2022

# Layers Of Maturation In Cortical Hierarchies

Adam Pines
*University of Pennsylvania*

# Layers Of Maturation In Cortical Hierarchies


## Abstract

Hierarchies form critical scaffolds for top-down processing but are often multiplex. In the brain, multiple layers of complex hierarchies intersect, dissociate, and re-converge over the lifespan. Although aspects of local hierarchical organizations are well-mapped for sensory systems, the fashion by which hierarchical organization extends globally is unknown. Human neuroimaging provides a means by which to observe both the developmental emergence and functions of global neurohierarchical organization. Here, we leveraged these advances to distill multiple layers of hierarchical formation across diverse brain-tissue quantifications. We demonstrate that these layers form common and dissociable biomarkers of the developmental emergence of complex cognition. Our results indicate that multiplex neurocognitive development both processes across a normative hierarchical pattern and contributes to engraining the pattern into cortical function. Further, our results suggest that neurocognitive development is largely contemporaneous with neurocognitive aging in an integrated, flexible lifespan sequence.



## Degree Type

Dissertation

## Degree Name

Doctor of Philosophy (PhD)

## Graduate Group

Neuroscience

## First Advisor

Theodore D. Satterthwaite

## Keywords

Development, Hierarchy, Maturation, Multivariate

## Subject Categories

Neuroscience and Neurobiology

# LAYERS OF MATURATION IN CORTICAL HIERARCHIES

Adam Pines

A DISSERTATION

in

Neuroscience

Presented to the Faculties of the University of Pennsylvania

in

Partial Fulfillment of the Requirements for the

Degree of Doctor of Philosophy

2022

Supervisor of Dissertation

Theodore Satterthwaite

Associate Professor of Psychiatry

Graduate Group Chairperson

Joshua Gold

Professor of Neuroscience

Dissertation Committee

| | |
|---|---|
| Allyson Mackey | Assistant Professor of Psychology |
| Russell Shinohara | Associate Professor of Biostatistics |
| Aaron Alexander-Bloch | Assistant Professor of Psychiatry |
| Raquel Gur | Karl and Linda Rickels Professor of Psychiatry |

ABSTRACT

LAYERS OF MATURATION IN CORTICAL HIERARCHIES

Adam Pines

Theodore Satterthwaite

Hierarchies form critical scaffolds for top-down processing but are often multiplex. In the brain, multiple layers of complex hierarchies intersect, dissociate, and re-converge over the lifespan. Although aspects of local hierarchical organizations are well-mapped for sensory systems, the fashion by which hierarchical organization extends globally is unknown. Human neuroimaging provides a means by which to observe both the developmental emergence and functions of global neurohierarchical organization. Here, we leveraged these advances to distill multiple layers of hierarchical formation across diverse brain-tissue quantifications. We demonstrate that these layers form common and dissociable biomarkers of the developmental emergence of complex cognition. Our results indicate that multiplex neurocognitive development both processes across a normative hierarchical pattern and contributes to engraining the pattern into cortical function. Further, our results suggest that neurocognitive development is largely contemporaneous with neurocognitive aging in an integrated, flexible lifespan sequence.

TABLE OF CONTENTS

LIST OF TABLES

LIST OF ILLUSTRATIONS

# CHAPTER 1: INTRODUCTION

The brain is complicated. There's a lot going on. For comparison, consider the universe. Pierre-Simon Laplace's deterministic postulation of the universe was that if someone knew the exact location and momentum of all molecules in the universe at a single point in time, the future of the universe would be predictable (Laplace, 1814). In the brain, some organizational regimes exist purely dynamically: organization that occurs explicitly *across* time rather than at any one point (Buzsáki & Draguhn, 2004; Palva & Palva, 2018). We find already that our contemporary conception of the brain is beyond the complexity of the Laplacian conception of the universe.

In the conquest of biology, complexity is a foe. Our typical approach of compartmentalizing, cornering, and interrogating small subunits of the human system has proven insufficient at surmounting this foe. Because of our reasonable preference for discrete, dissociable constructs of facts, the guerilla interconnectivity of the brain eludes our conceptual, semantic, and even causal frameworks. Consequently, only the most predictable pathways in the brain have surrendered their secrets.

Off of the scientific front, complexity is an evolutionarily won privilege (Hill et al., 2010), a natural optimization of adaptation to and forging of our environment (Buckner & Krienen, 2013). However, feedforward and feedback relationships are reciprocal between the mind and environment (Adler, 1927; Brinkmann et al., 2022). The environment has predominantly fed-forward down onto us. The sky became hostile; we moved underground (Macleod et al., 1997). The land became the sea; we built boats (Sumerians, 2,100-1,800 B.C.). The water left our fields; we made caravans (Drews, 1993). But our adaptations have extended so far as to confuse the traditional perspective of feed-forward communication propagating solely from the top-down. Adaptations have forged the environment receiver.

By externalizing our conscious and unconscious processing onto the environment, we bestow ourselves with greater capacity to consider and adapt to our shifting needs. Through projecting monetary value onto discrete, standardized, objects, we discovered our capacity to

consider the logical extreme extensions of these objects: 0 and infinity (Casselman, 2007). Towering edifices of mentation stand atop the semantic scaffolds we built by first projecting discrete, standardized concepts onto words and symbols (Berwick & Chomsky, 2016). By ascribing the impossible odds of our existence and terrifying uncertainty of the world around us to deities, we were able to forge and sign extensive social contracts under a unified banner of appreciation for the ineffable (Rousseau, 1762). By producing photographs, we've offloaded our own memory storage constraints. By delineating demonizations, we've mitigated the burdens of processing of our own deep-seeded discontents. But our innate tendency to aggregate worldviews piecemeal in small, independently true flashcard-constructs now presents a direct barrier to neuroscientific progress. The brain isn't a sum of individual units, it's a pattern.

And as the pattern refines over species, within-individual refinement of the pattern encounters more freedom to adapt at multiple smaller scales. Children accelerate their own development in response to the demands laid upon them,  or pump the breaks on their development if they are afforded the time (Bath et al., 2016; Bavelier et al., 2010; Callaghan & Tottenham, 2016; Casey et al., 2011; Larsen & Luna, 2018; Tooley et al., 2021). Here, we see evidence of another example beyond Laplace. Developmental acceleration serves the purpose of rapidly bringing the organism to maturity, arguably for the purpose of acquiring safety for progeny (Adler, 1927). Progeny who obtain such security are subsequently afforded the opportunity to decelerate their development, allowing for more total adaptivity but over a longer period of time (Vainik et al., 2020). Although the exact periodicity is unknown, existing data suggests that intergenerational epigenetic oscillations occurs contemporaneously with intergenerational safety oscillations (Adler, 1927). Such an intergenerational sociogenetic program, resonating across time, undoubtedly invokes bidirectional feedback loops at multiple scales.

Because neural and social systems are reciprocally integrated at multiple levels (Lamarck, 1802; Darwin, 1859) the interconnectivity of brain and social organization is the most honest realization of either. The joint form is the true form.

To “identify” multiplex patterns, the brain extracts multisensory information and integrates them into an abstract representation. Consequently, our hope of understanding the functions and dysfunctions of social interactions, health, and neuronal interactions, information lies within our ability to extract information from each sphere and integrate them holistically into a low-dimensional pattern. Our propensity for interpreting low-dimensional patterns is great enough to warrant such hope. A century ago, Adler noted that we might leverage “curves” to understand development of the mind:

*“Since movements may have many meanings [gaining knowledge] is not always so simple. We can however take many movements of an individual, compare them, and understand of a human being by connecting two points wherein a definite attitude of the psychic life was expressed, in which the difference in time is noted by a curve.”* (Adler, 1927).

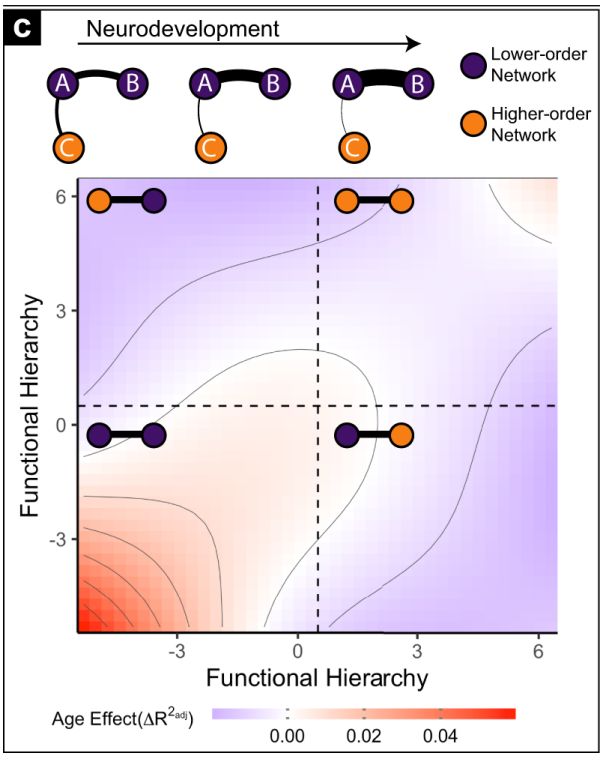


Figure 1.1 Four continuous variables (Age, functional connectivity, hierarchical positioning of network on x-axis, hierarchical positioning of network on y-axis) represented as a surface.

Let’s consider a three dimensional curve: a topographical surface such as that we might use to plan a hike. By leveraging recent advances in statistical and visualization software, we can extract and visualize non-linear interactions between four continuous variables as a single topographical surface (Age, functional connectivity, hierarchical positioning of network A, hierarchical positioning of network B; **Figure 1.1**). Next, we might integrate this topographical surface into a low-dimensional, semantic pattern. In this example, we might say that “over development, coupling between lower-order networks strengthens and coupling between lower-order and higher-order networks attenuates” (Pines et al., 2022a).

Now by virtue of integration, we've reduced 4 dimensions of variation (age, functional connectivity, network A hierarchical position, network B hierarchical position) to 3 salient dimensions of variation (age, coupling between lower-order networks, coupling between lower- and higher-order networks). Notably, continuous topographical surfaces are simplifications of even abstract space, which likely contains un-represented "holes" (Heidecker et al., 2010). Further, transforming four variables to three represents a modest dimensionality reduction; let us bear our limitations every step of the way. Following this limethod, there are at least two steps to further our understanding of neuronal functions. 1) Sampling multiple spheres of information and 2) integrating this information to fewer spheres.

Given that no spatiotemporal scale of brain function is independent (Betzel & Bassett, 2017; Buzsáki & Draguhn, 2004), the desire to advance our understanding of the brain begets an obligation to sample across scales. This obligation arises out of primarily a concern of generalizability: if we don't know that an observation is true for at least several of the trillions of levels of organization in the brain, how can we confidently integrate that observation into our worldview? Consider several well-established spheres of scale.

Spatially, the brain exhibits meaningful organization at the level of lobes, regions, sulci, columns, microcircuits, arbors, and boutons. Temporally, meaningful organization exists at the level of guided evolution (Melamed et al., 2022), intergenerational memory (Rudolph et al., 2018), generational memory (Leskovec et al., 2009), seasonal fluctuations (Melrose, 2015), circadian rhythms (Vitaterna et al., 2001), infraslow, alpha, beta, delta, gamma, and at least high gamma oscillations (Buzsáki & Draguhn, 2004). These temporal scales interact across spatial scales (Braun et al., 2018; Breakspear & Stam, 2005; Mitra et al., 2018), and layer themselves on top of layers of neurogenic systems. Astrocyte networks, vascularization, glymphatic, inhibitory, excitatory, hormonal, and epigenetic pathways all fleetingly intersect (Cadwell et al., 2019; Leinekugel et al., 2002), converge to yield irreversible changes (Antón-Bolaños et al., 2019; Cadwell et al., 2019), and again diverge (Blinder et al., 2013) once they are put to the microscope.

So if the parts might not be known independent of the whole, but *we* are unable to reconstruct the whole without parts, where is the beginning of the delineation? Only those tenants that generalize the most expansively across scales and systems might form a foundation with this formula. The brain uses Adenosine Triphosphate. The brain uses electricity. The brain can be broken.

So the foundation is sparse but present. But in which direction might we build? Incentive structures lead the way, particularly for aggregate advancements where normative responses dominate ("Budget of NASA," 2022). Our moral incentive structures are strikingly consistent across spatiotemporally diverse populations, typically reaching their apex at mitigating the suffering of children (Dostoyevsky, 1879). In the context of genetic programs exploiting and rationing their time allotted to development, we might consider this consistency over generations of gene-rations more ascribable to Gemeinschaftsgefühl than individual will. And so we find that although our foundations for *understanding* the brain are sparse, our foundational *drive* might be enough of a common denominator across time to serve as a foundation for numerators (Wegman, 2001). In other words, we can come together to negatively mediate the suffering with improved understandings of the brain (Brody et al., 2017).

What foundations might we have here? The distillation and purification of Freud, Jung, and Adler has provided the strongest lead on the social antecedents of psychopathologies, suggesting that psychopathologies are reflections of early childhood maladaptivity (Adler, 1927). Mapping the emergence of psychopathologies over the temporal domain has suggested that normative neurodevelopment might be a causal agent in psycopathology (Casey et al., 2011). Psychopathologies emerge most often in an adolescent wave, corresponding to a wave of genetic expression (Li et al., 2018).

Are there foundations of adolescent neurodevelopment? We know that the primordial waters of the brain are drained and relegated to the ventricles (Le Bihan, 2007; Chang et al., 2015; Pines et al., 2020), sensation matures earlier than cognition (Gogtay et al., 2004; Sotiras et

al., 2017; Sowell et al., 1999), and that development is expensive (Kleitman & Engelmann, 1953). This crystallization is a tenuous process, only safe relative to its absence.

Observing individually-variable aspects of neurocognitive development might serve to further elucidate both the biological and social substrates of psychopathologies. What relates to what under what conditions and considerations? What structure might the foundations suggest? What functions? Where is the leading wall that we might throw our brick onto, rather than aimlessly into the air? In another reciprocal feedforward loop, we first must consider what is being done before we consider what has been done.

Diffusion-weighted imaging (DWI) has informed our understanding of both local tissue (Basser and Pierpaoli, 1996; Koh and Padhani, 2006; Svolos et al., 2014) and distributed network properties of the brain *in vivo* (Sporns et al., 2005; Gollo et al., 2018). DWI has proven to be particularly useful for studying neurodevelopment, and has provided critical evidence of the protracted maturation of white matter from infancy into adulthood (Lebel et al., 2008; Schmithorst and Yuan, 2010; Asato et al., 2010; Larsen et al., 2018; Jalbrzikowski et al., 2017). Recent studies have leveraged tools from network neuroscience and established that structural networks reconfigure in development to promote efficient communication (Hagmann et al., 2010; Fan et al., 2011; Grayson et al., 2014; Baum et al., 2017; Uddin et al., 2011; Baker et al., 2015; Bassett et al., 2018; Huang et al., 2015).

Most DWI studies have used single *b*-value diffusion acquisitions (“single shell”) and applied a diffusion tensor imaging (DTI) model to characterize observed diffusion patterns as indices of neuronal microstructure (Lebel and Deoni, 2018; Lebel et al., 2017). While valuable, these studies may have been limited by certain characteristics of the diffusion tensor model and single-shell imaging sequences. In practice, metrics derived from the diffusion tensor model underestimate diffusion restriction in voxels within crossing fibers (Jeurissen et al., 2013; Jones and Cercignani, 2010; Volz et al., 2018; De Santis et al., 2014) and are systematically impacted by in-scanner motion, which is often prominent in children (Yendiki et al., 2014; Ling et al., 2012; Baum et al., 2018; Roalf et al., 2016). More recently, a new generation of models have

been developed to leverage multiple *b*-values ("multi-shell"). Although it is unknown if these new models ameliorate the potential impact of motion or other artifacts, they do offer promising advances in characterizing white matter. When systematically varied over a DWI acquisition, the differential tissue responses elicited by different *b*-values can be used to model more detailed features of the cellular environment (Stanisz et al., 1997; Clark et al., 2002; Assaf and Basser, 2005). These models can be broadly separated into "tissue" and "signal" models (Alexander et al., 2017; Ferizi et al., 2017): tissue models attempt to classify signal attributable to different components of biological tissues, while signal models model the diffusion process directly and do not attempt to delineate tissue composition.

Although several tissue models were foundational for tissue modeling of diffusion images (Assaf and Basser, 2005; Alexander et al., 2010), Neurite Orientation Dispersion and Density Imaging has become the most widely used (NODDI; Zhang et al., 2012). NODDI provides estimates of the directional distribution of neurites (axons and dendrites) as well as compartmental volume fractions. Volume fractions convey the proportion of volume posited to be intracellular, extracellular and isotropic in each voxel based on the estimated contributions of these compartments to the diffusion signal. In contrast to DTI metrics, NODDI estimates separate parameters for the directional spread of water diffusion and the degree of microstructural restriction of water diffusion. This distinction allows more specific tissue properties to be discerned, like fiber direction coherence and intracellular volume fraction. As such, NODDI provides an advance in disambiguating properties of putative cellular microstructure over DTI (Chang et al., 2015; Eaton-Rosen et al., 2015; Mah et al., 2017; Zhang et al., 2012; Kodiweera et al., 2016; Timmers et al., 2016). These differences may have particular importance for developmental studies as recent work suggests that NODDI may be more sensitive to brain development than DTI (Chang et al., 2015; Genc et al., 2017; Nazeri et al., 2015; Mah et al., 2017; Ota et al., 2017). However, it remains unclear as to how useful NODDI-based measures are for studies of brain networks, or how they are impacted by in-scanner motion.

In contrast to tissue-based models like NODDI, “signal” based methods remain agnostic to tissue composition when characterizing the intra-voxel diffusion process. Two recently-introduced techniques which model the intra-voxel diffusion process are Mean Apparent Propagator MRI (MAP-MRI; Özarslan et al., 2013) and Laplacian-regularized MAP-MRI (MAPL; Fick et al., 2016a). Laplacian regularization makes MAPL more resilient to noisy data, which is a particularly important issue in studies of brain development. Notably, signal-based models estimate water molecule displacement patterns without *a priori* assumptions about the underlying tissue environment (Özarslan et al., 2013; Karmacharya et al., 2018). In contrast to the accumulating number of studies using NODDI to investigate brain development, MAPL has not previously been used in studies of brain maturation. Furthermore, like NODDI, it remains unknown how in-scanner motion may impact MAPL-based measures.

Here, we see that the development of dehydration, but technologies have advanced to allow us to assay hydration from *many angles*.

Graded transitions from bottom-up, feedforward projections to top-down, feedback projections create an anatomic hierarchy of both regional[1,2] and global[3,4] cortical organization. In turn, anatomical hierarchy supports a hierarchy of cortical function. Whereas regional hierarchical organization facilitates higher-order stimulus encoding in sensory networks[1], global hierarchical organization is thought to facilitate the development of executive functioning (EF)[5,6,7]. Critically, initial evidence suggests that global hierarchical organization is not established in youth, but instead is a product of protracted development[8,9,10]. Understanding the normative process by which hierarchical cortical organization emerges and supports EF is crucial, as deficits in the emergence of EF are associated with lower academic achievement[11,12], risk-taking behaviors[13], and most major psychiatric illnesses[14,15,16].

Large-scale patterns of functional organization can be identified in humans using functional MRI (fMRI), which allows for studies of development and cognition. Prior developmental neuroimaging studies have found that a sensorimotor to association hierarchy represents a principal mode of functional coupling in adults[17], but not in infants[8] or children[9,10].

These results implicate development as central in the establishment of a normative cortical hierarchy, but the process by which this hierarchy emerges is unclear. In parallel, recent studies of cognition in neurodevelopment have found that functional segregation of cortical networks near the top of the hierarchy from lower-order networks supports the emergence of EF[18,19,20]. Although these results further suggest a role of functional hierarchy in cognitive development, other studies have produced discrepant results[21,22,23,24], leaving the role of cortical hierarchy in cognitive development unclear. This lack of consensus across existing work may arise due to two limitations that are shared across prior studies.

First, nearly all studies of functional network development only examine a single network resolution or scale. Typically, investigators use standard network atlases that specify a single number of functional networks (e.g., 7, 14, or 17). However, it is increasingly recognized that the brain is a multi-scale system, and that studies of a specific resolution of subnetworks may be limited[25,26,27,28]. Rather, evidence suggests that brain network organization emerges from neural coordination across overlapping spatial scales[25,29,30,31]. Importantly, distinct brain-behavior relationships may be present at different scales[32], with each scale potentially offering complementary information regarding multifaceted processes such as development. As a result, current accounts of brain development that rely on a single network scale are almost certainly incomplete and may hamper our ability to synthesize findings across studies where different scales were examined[33,34].

A second key limitation of prior studies of functional network development is that they have not accounted for individual differences in the spatial layout of brain networks on the cortical mantle. Multiple independent studies in adults using different datasets and distinct methods have provided convergent evidence that there is prominent between-individual variability in the spatial distribution (i.e., the functional topography) of large-scale networks on the anatomic cortex[35,36,37,38,39]. In studies of adults, transmodal association networks tend to have the greatest variability in functional topography[36,37,38,39]; recent work has shown that this is also true in children and adolescents[40]. Accounting for such individual variation in functional

topography may be critical for understanding the development of coupling between networks, as prior work has shown that differences in spatial topography can be aliased into estimates of connectivity[35,41]. Further, individual differences in spatial topography and individual differences in connectivity can have distinct associations with psychopathology[42]. Finally, individual-specific–or "personalized"–networks may be particularly relevant when evaluating development at multiple scales, as individual variation in topography might depend in part on network resolution[43,44].

Here, we see that the development of network differentiation, but technologies have advanced to allow us to assay differentiation from *many scales*.

The hierarchical organization of the cortex underlies bottom-up sensory integration and top-down control[1,2,3]. Existing evidence suggests that cortex-wide hierarchical organization is a product of protracted development[4,5,6]. Understanding the development of hierarchical processing is critical, as developmental deficits in top-down control are associated with transdiagnostic psychopathology[7], reduced quality of life[8], and youth mortality[9]. In the brain, hierarchical processing necessarily involves activity propagating through space between higher and lower-order areas. However, fMRI studies concerning hierarchical processing have chiefly quantified activity fluctuations in fixed regions over time, rather than examining activity propagations over space.

More recently, several studies used a combination of fMRI and intracranial recordings to demonstrate that infraslow but large-scale activity systematically propagates along a principal gradient (PG)[10] of cortical organization from lower to higher-order areas[11,12,13]. Two studies also noted top-down propagations, where activity instead moved from higher-order to lower-order areas. Intriguingly, such top-down propagations were associated with alertness[12] and the ascending arousal system[14], suggesting that top-down propagations might be linked to top-down cognitive processing. However, to infer hierarchical directionality, these approaches associated a single, group-level cortical pattern with the time series of a single variable: either respiratory variability[12], the global signal[13], or the difference in signal from two subcortical regions over time[14]. While these approaches revealed stereotyped hierarchical propagations, they are not

sensitive to propagations associated with other physiological events, concurrent propagations, or propagations that are spatially or temporally variable between individuals. As a result, little is known about how propagations vary across individuals and mature with development.

Here, we see that the development of top-down propagations might be assayed by *many overlapping timecourses* (Pines et al., 2022b). Let's check it out.

# CHAPTER 2: LEVERAGING MULTI-SHELL DIFFUSION FOR STUDIES OF BRAIN DEVELOPMENT IN YOUTH AND YOUNG ADULTHOOD

## 1. Premise

Here, we sought to describe the relationships between three diffusion models, brain development, and in-scanner motion. We evaluated how diffusion metrics from DTI, NODDI, and MAPL are associated with both age and in-scanner motion in a sample of 120 youth and young adults who completed multi-shell diffusion imaging. Importantly, we included DTI metrics derived from solely the *b* = 800 shell (to more closely match a traditional DTI scan), as well as the full multi-shell scheme. Statistical associations were examined across multiple scales of analysis, including global white matter values, tract values, edges in structural brain networks, and individual voxels. As described below, we present new evidence that multi-shell diffusion data can be leveraged to provide important advantages for studies of the developing brain.

## 2. Methods

### 2.1. Participant characteristics

After quality assurance (section 2.3), we studied 120 participants between the ages of 12 and 30 years old (*M* = 21.27, *SD* = 3.36, 68 females). Potential participants were excluded due to metallic implants, claustrophobia, pregnancy, acute intoxication, as well as significant medical and/or developmental conditions that could impact brain function. Parental consent and assent was obtained for minors participating in the study (*n* = 21; 18 after quality assurance). All protocols were approved by the University of Pennsylvania's Institutional Review Board.

### 2.2. Image acquisition

All participants were imaged on a 3-Tesla Siemens MAGNETOM Prisma with a T1-weighted structural and diffusion-weighted scan. Our structural scan was a 3 min 28 s MPRAGE sequence with 0.9 × 0.9 × 1.0 $mm^3$ resolution (TR =1810 ms, TE =3.45 ms, inversion time =1100 ms, flip

angle = 9 degrees, acceleration factor = 2). Our DWI sequence was a single-shot, multiband, multi-shell acquisition protocol (TR =3027 ms, TE =82.80 ms, flip angle = 78 degrees, voxel size = 1.5 $mm^3$ isotropic, FOV = 210 mm, acquisition time =6 min 12 s, multi-band GRAPPA acceleration factor = 4, phase-encoding direction = anterior to posterior) with 3 diffusion-weighted shells at b = 300 $s/mm^2$ (15 volumes), b = 800 $s/mm^2$ (30 volumes), and b = 2000$s/mm^2$ (64 volumes). The sequence included 9 b = 0 $s/mm^2$ scans interspersed throughout. We also acquired a b = 0 $s/mm^2$ reference scan with the opposite phase-encoding direction (posterior to anterior) to correct for phase-encoding direction-induced distortions.

### 2.3. Pre-processing and quality assurance

Distortions induced by phase encoding were corrected using *topup* from the FMRIB Software Library (*FSL*; Jenkinson et al., 2012). Eddy-current distortions and in-scanner movement were corrected using *eddy* from FSL version 5.0.11 with both single slice and multiband outlier replacement (Jenkinson et al., 2012; Andersson et al., 2016, 2017); this processing step also rotated the initial *b*-vectors from our sequence to align with estimated subject head motions. Motion-, distortion-, and eddy-corrected images served as the common input to all diffusion modeling methods.

Following prior work, we quantified in-scanner motion using the root mean squared displacement over the course of the scan (mean relative RMS; Baum et al., 2018; Roalf et al., 2016). To ensure robustness of our findings across different measurements of diffusion image quality, we also quantified and assessed temporal signal-to-noise ratio (tSNR). Mean relative RMS displacement was calculated between the interspersed *b* = 0 images, while tSNR was calculated from exclusively the *b* = 800 shell as in prior work (Roalf et al., 2016). Both metrics were calculated with publicly available tools (https://www.med.upenn.edu/cmroi/qascripts.html). Subsequently, three participants were removed for high in-scanner motion (mean relative RMS ≥ 2.95 *SD* above the mean) and one participant was removed for low signal-to-noise ratio (tSNR = 3.47 *SD* below

the mean). Manual inspection of all T1 images led to one additional participant being removed for poor T1 image quality.

### 2.4. Overview of diffusion metrics

We evaluated 14 diffusion metrics from three DWI modeling techniques. From DTI, we calculated fractional anisotropy (FA), mean diffusivity (MD), axial diffusivity (AD), and radial diffusivity (RD; Basser et al., 1994). In accordance with previous applications of DTI to multi-shell data, we fit the DTI model using only the shell where gaussian diffusion patterns were expected ($b$ = 800; Jones and Basser, 2004). We also fit a DTI model to the entire multi-shell dataset using an iteratively reweighted linear least squares estimator tensor fit (Veerart et al., 2013), yielding a multi-shell version of each of the same 4 diffusion metrics. From NODDI, we calculated orientation dispersion indices (ODI), the intracellular volume fraction (ICVF), and the isotropic volume fraction (ISOVF; Zhang et al., 2012). From MAPL, we evaluated the return-to-origin (RTOP), return-to-axis (RTAP), and return-to-plane (RTPP) probabilities (Özarslan et al., 2013; Fick et al., 2016a).

#### 2.4.1. DTI metrics

DTI assesses the directionality and magnitude of water diffusion by assuming a Gaussian diffusion process in each voxel. DTI utilizes a 6 degrees of freedom symmetric tensor model that is fit to the observed signal. Subsequently, the primary direction of diffusion in a voxel is calculated by finding the largest eigenvalue of the tensor. After tensors are fit to a voxel, FA, MD, AD, and RD can be calculated from the corresponding eigenvalues. While MD is the averaged sum of these eigenvalues (representing the average magnitude of water diffusion), AD is derived from only the largest eigenvalue (representing the primary direction of diffusion). RD is the average of the remaining two eigenvalues, both representing eigenvectors orthogonal to the primary one. Finally, FA evaluates the magnitude of the eigenvalue associated with the primary direction of diffusion *relative* to the remaining eigenvalues. Thus, FA represents the fraction of

anisotropy in a voxel aligned with a primary direction of diffusion. As diffusion shows increasing directional preference, FA increases (Soares et al., 2013; Basser et al., 1994).

All DTI metrics were calculated in MRtrix3 using an iteratively reweighted linear tensor fitting procedure (Tournier et al., 2012; Veerart et al., 2013). As mentioned, we included FA, MD, AD, and RD derived from a DTI fit to all of the shells, as well as the same DTI metrics derived from the *b* = 800 shell only. This processing choice was made to account for the possibility that the utility of including more diffusion directions was outweighed by the non-Gaussian contribution of high *b*-value acquisitions.

### 2.4.2. NODDI metrics

NODDI estimates the directional distribution of neurites (axons and dendrites) in a voxel, and then matches diffusion patterns to that distribution. Like DTI, this model is informed by restriction of diffusion unaligned with neuronal fibers, and unhindered diffusion along their prominent axes. Unlike DTI, the introduction of a 3D neurite distribution allows for modeling diffusion restriction in fiber populations with dispersed orientations.

NODDI attempts to parse the diffusion signal into discrete contributions of cellular compartments. The total signal is set to equal the sum of the contributions from each compartment, such that A=(1-Viso)(VicAic+(1-Vic)Aec)+VisoAiso, where *A* is the full diffusion signal, Aic, Aec, and Aiso are the signal attributable to the intracellular, extracellular, and isotropic compartments, and Viso, Vic, and Vec represent the fraction of tissue volume attributable to the corresponding compartments. In order to assign diffusion signal to one of these compartments, the method assumes neurites can be modeled as zero-radius cylinders, or sticks. NODDI then fits an estimated distribution of these sticks to a spherical distribution, which captures the estimated spread of neurite orientations. ODI measures this spread, which ranges from 0 (non-dispersed) to 1 (highly dispersed). $A_{ic}$ is calculated with respect to this posited orientation dispersion in any given voxel. Intracellular signal is estimated by comparing the spherical distribution of neurite

orientations with the distribution of unimpeded diffusion, yielding Vic, or the ICVF metric. Isotropic diffusion signal is attributed to a cerebrospinal fluid compartment, which yields the ISOVF metric (Zhang et al., 2012). Recent advances have markedly accelerated fitting the NODDI model; here we calculated NODDI using AMICO, which has been shown to accelerate fitting the NODDI model by several orders of magnitude without substantially impacting accuracy (Daducci et al., 2015).

2.4.3. MAPL metrics

Unlike tissue-based models such as NODDI, signal-based techniques seek to model the diffusion process directly and do not assume the separability of specific tissue compartments. In contrast to DTI, MAPL is not limited to representing diffusion as ellipsoids, and can therefore in theory capture arbitrary fiber configurations. MAP-MRI characterizes observed DWI signal as a linear combination of angular and radial basis functions. Once fit to the DWI signal, analytic transforms can be directly applied to estimate both the 3D diffusion propagator and the angular diffusion orientation distribution function (Özarslan et al., 2013; Walter, 1977). Building on MAP-MRI, Fick et al. (2016a) recently introduced Laplacian-regularized MAP-MRI (MAPL). MAPL imposes additional smoothness on MAP-MRI's coefficient estimation using the norm of the Laplacian of the reconstructed signal. This approach effectively penalizes model fits with physiologically improbable high local variances, which are more likely to be artifactual than reflective of signals of interest (Descoteaux et al., 2007). The authors also demonstrated that this method reduces error over MAP-MRI in voxels with crossing fibers (Fick et al., 2016a).

MAP-MRI and MAPL allow for quantification of the likelihood that diffusing molecules undergo zero net displacement in one, two, or three dimensions. More specifically, RTOP estimates the probability of water molecules undergoing no net displacement in any direction. RTAP estimates the probability that molecules undergo no net displacement from their primary axis of diffusion; this axis typically represents the average neuronal tract direction within any given voxel (Assaf and Ofer, 2008; Basser et al., 2000). Finally, RTPP estimates the probability that molecules are

not displaced from their original plane perpendicular to the primary direction of diffusion, but is not sensitive towards movement of molecules within that plane (Özarslan et al., 2013). It is important to note that these values reflect probabilities but are not scaled to reflect formal probabilities in the range of 0–1 (Fick et al., 2016a). We fit the MAPL model with a radial order of 8, without anisotropic scaling, using generalized cross-validation for determining optimal regularization weighting. We conducted model fitting and generated RTOP, RTAP, and RTPP with dipy, an open-source diffusion imaging toolbox in Python (Fick et al., 2016a; Garyfallidis et al., 2014).

### 2.5. Structural image processing

T1 images were processed using the ANTs Cortical Thickness Pipeline (Tustison et al., 2014). Images were bias field corrected using N4ITK (Tustison et al., 2010), and brains were extracted from T1 images using study-specific tissue priors (Avants, Tustison, Wu, et al., 2011). We utilized a custom young-adult template constructed via the *buildtemplateparallel* procedure in ANTs (Avants et al., 2011a, 2011b). A custom template was used due to evidence demonstrating the utility of custom templates in reducing registration biases (Tustison et al., 2014). The T1 to template affine and diffeomorphic transformations were calculated with the top-performing symmetric diffeomorphic normalization (SyN) tool in ANTs (Klein et al., 2009). The transforms between T1 and the initial $b$ = 0 DWI images were calculated using boundary-based registration with 6 degrees of freedom (Greve and Fischl, 2009). All transforms were concatenated so that only one interpolation was performed.

### 2.6. Network construction

Accumulating evidence suggests that structural brain networks undergo substantial maturation during youth (Hagmann et al., 2010; Fan et al., 2011; Grayson et al., 2014; Baum et al., 2017; Uddin et al., 2011; Baker et al., 2015). Accordingly, in addition to analysis of summary measures and scalar maps, we evaluated each measure in the context of structural networks. Networks were constructed using the Schaefer 200 cortical parcellation (Schaefer et al., 2014).

The parcellation was warped to the custom template, and then projected back to each subject's T1 and native diffusion space using the inverse of each transform. Whole-brain connectomes were constructed by representing each of the 200 regions as a network node, while deterministic tractography was used to create network edges. Tractography was conducted in Camino (Cook et al., 2006) using the Euler tracking algorithm in native diffusion space (Basser et al., 2000). The intersections between gray and 1mm-dilated white matter were used as both seed regions and termination points for tractography. We used voxels defined as CSF by the segmented T1 image as termination boundaries for streamlines. Voxels defined as white matter by the segmented T1 image were used as an inclusion mask for streamlines, ensuring that streamlines had to pass through white matter. Additionally, we imposed a curvature restriction on all streamlines. Fibers determined to curve more than 60 degrees over a 5 mm interval were discarded in order to mitigate the impact of noise on tractography (Bastiani et al., 2012). Lastly, the mean value of each diffusion metric was calculated along each edge in this network; these values were used as edge weights between nodes connected via tractography. As higher values of ODI and ISOVF both indicate reduced anisotropic diffusivity, ODI and ISOVF values were transformed as 1 – ODI and 1 – ISOVF for weighted structural networks. Similarly, as higher MD and RD also indicate reduced anisotropy, their inverse values (1/RD and 1/MD) were utilized for weighting structural networks.

### 2.7. Statistical analyses

In order to determine how the spatial distribution of the different diffusion metrics covary, we first evaluated their spatial covariance within subjects across white matter. Specifically, within subjects, we calculated the Spearman's ρ between each diffusion metric across all white matter voxels. To do so, we masked native-space diffusion images, vectorized diffusion metric values across voxels, and correlated the 14 vectors for each participant. Metric by metric correlations were averaged across all participants.

Next, we sought to evaluate the sensitivity of each diffusion metric for investigating neurodevelopment across four levels of features (see schematic in Fig. 2.1). First, we evaluated age associations with mean diffusion metric values within a global white matter mask. Second, we analyzed regional effects using a common white matter atlas (Mori et al., 2008). Third, we conducted mass-univariate voxelwise analyses within white matter. Finally, we evaluated associations between age and edges within tractography-based structural networks.

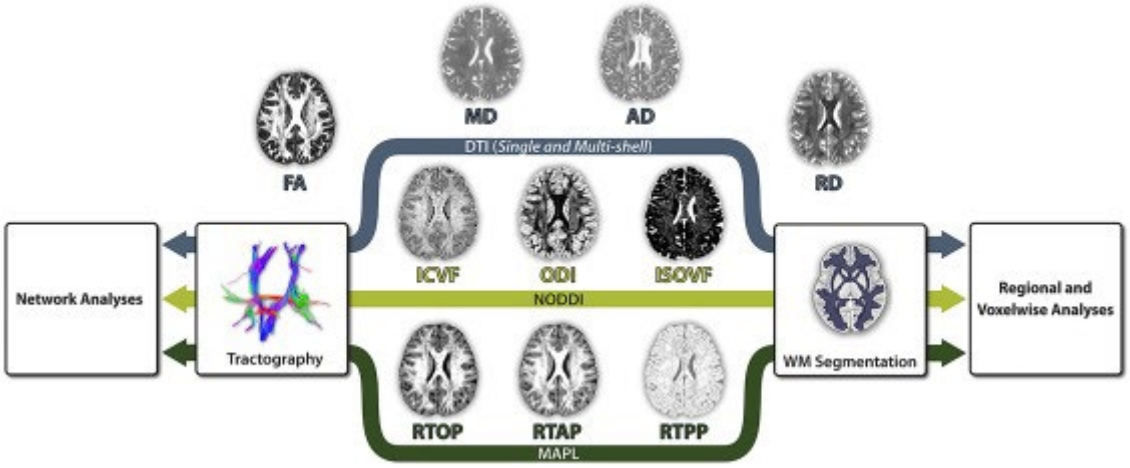


Figure 2.1 Analytic workflow. The DTI, NODDI, and MAPL models were fit to the same motion-, distortion-, and eddy-current corrected images, with the exception of the single-shell DTI fit, which only utilized the corrected $b$ = 800 data. The resulting scalar maps were evaluated for associations with both age and data quality at multiple levels of analysis, including mean white matter values, mean values within tracts, white matter voxels, and network edges reconstructed by deterministic tractography that were weighted by each metric.

For all analyses, age effects were estimated with penalized splines and generalized additive models (GAMs; Wood, 2001, 2004) in R (Version 3.5.1) using the *mgcv* package (R Core Team, 2013; Wood, 2011). To avoid over-fitting, nonlinearity was penalized using restricted maximum likelihood (REML). Sex and in-scanner motion were included as linear covariates. For voxel and edge-level analyses, statistical significance maps were thresholded at $p < 0.001$ (uncorrected). In order to identify periods of significant neurodevelopment, we quantified the slope of the spline fit for age in each GAM from its derivative. We operationalized the window of significant age-related

change as the period at which the 95 % confidence interval of the spline's estimated slope did not include 0. These calculations were conducted with the *gratia* package in R (Simpson, 2018). Additionally, to compare the strength of the age effects across metrics, we calculated an estimate of effect size. As conventional effect size estimates are not available for smoothed terms in GAMs, we calculated effect sizes with polynomial models. We calculated the difference in variance explained (change in $R^2$) between a model that included motion and sex terms *only* and a model that also included polynomial age terms (linear, quadratic and cubic). As such, the reduced models took the form of $y = \beta_{\text{Head Motion}} + \beta_{\text{Sex}}$. The full polynomial models were: $y = \beta_{\text{Head Motion}} + \beta_{\text{Sex}} + \beta_{\text{Age}} + \beta_{\text{Age}^2} + \beta_{\text{Age}}3$. In both models, $y$ was the diffusion metric of interest. We calculated the change in $R^2$ ($\Delta R^2$) between the full and reduced model to provide an estimate of the combined effect size of both linear and non-linear age terms; this was applied to all diffusion metrics evaluated.

In order to estimate the vulnerability of each metric to in-scanner motion, we calculated the correlation of each diffusion metric with our measurement of head motion. In order to remove age and sex effects from all head motion correlations, we first regressed out the effects of age and sex as estimated from GAMs to obtain model residuals. These residuals were then correlated with head motion. We used this correlation coefficient to quantify the relationships between each diffusion metric and head motion while controlling for common sources of variance.

### 2.8. Code availability

All analysis code is available at: https://github.com/PennBBL/multishell_diffusion.

## 3. Results

### 3.1. Measures of diffusion show differential patterns of covariance

As an initial step, we investigated the relationships between all diffusion metrics of interest with Spearman's correlations within white matter, and averaged these correlations across participants.

This included correlations obtained when using a multi-shell DTI fit (Fig. 2.2A, top triangle), and single-shell DTI fits (Fig. 2.2A, bottom triangle). As expected, metrics of diffusion restriction were highly correlated with each other (i.e., FA, ICVF, and RTOP), and negatively correlated with metrics of diffusion dispersion (i.e., MD, ODI). In contrast, measures like RTPP demonstrated less systemic covariation with other metrics. Multi- and single-shell DTI metrics were generally quite similar (Fig. 2.2B), with MD being the least similar across shell schemes ($r$ = 0.73). Next, we sought to understand the differential utility of these measures of diffusion for studies of brain development.

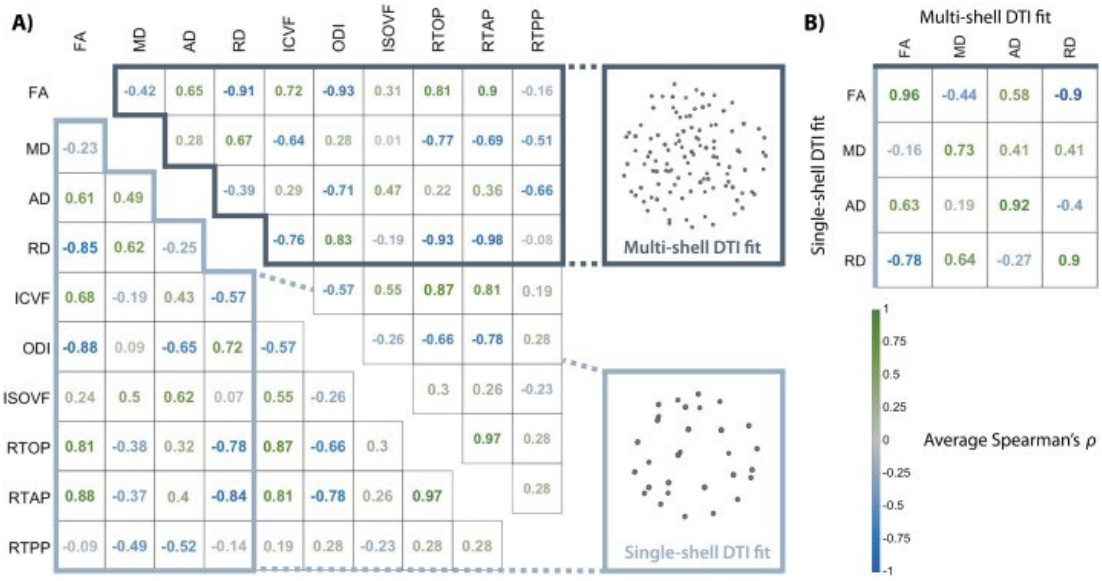


Figure 2.2 Measures of diffusion are differentially related. **A**. Average Spearman's correlations between diffusion metrics in white matter. The top triangle depicts correlations derived from multi-shell DTI fitting, and the bottom triangle reflects correlations derived from single-shell fits. In the corresponding sampling schemes, the distance of each dot from the center of the sphere represents the *b*-value of a single volume, and the angle represents its *b*-vector. **B**. Average correlations between single and multi-shell DTI metrics. FA = fractional anisotropy, MD = mean diffusivity, AD = axial diffusivity, RD = radial diffusivity, ICVF = intracellular volume fraction, ODI = orientation dispersion index, ISOVF = iso

### 3.2. Associations with age vary by diffusion measure

We evaluated the association of each diffusion metric with age at multiple scales. Specifically, we examined mean white matter values, mean values within white matter tracts, and high-resolution voxelwise mass-univariate analyses. While mean white matter values were significantly

associated with age across all 14 diffusion metrics, metrics that incorporated data from multiple shells tended to yield the largest age effect sizes (Fig. 2.3A, Table 2.1). When we examined the fitted age trajectories, as expected, we observed that associations with age were strongest at the younger end of the age range sampled and diminished during the transition to adulthood (Fig. 2.3B). For most diffusion metrics, the slopes of the age effects were no longer significant by the early 20's. ODI, ISOVF, and ssAD were notable exceptions in that their respective values significantly increased across the entire age range of our sample (Table 2.1).

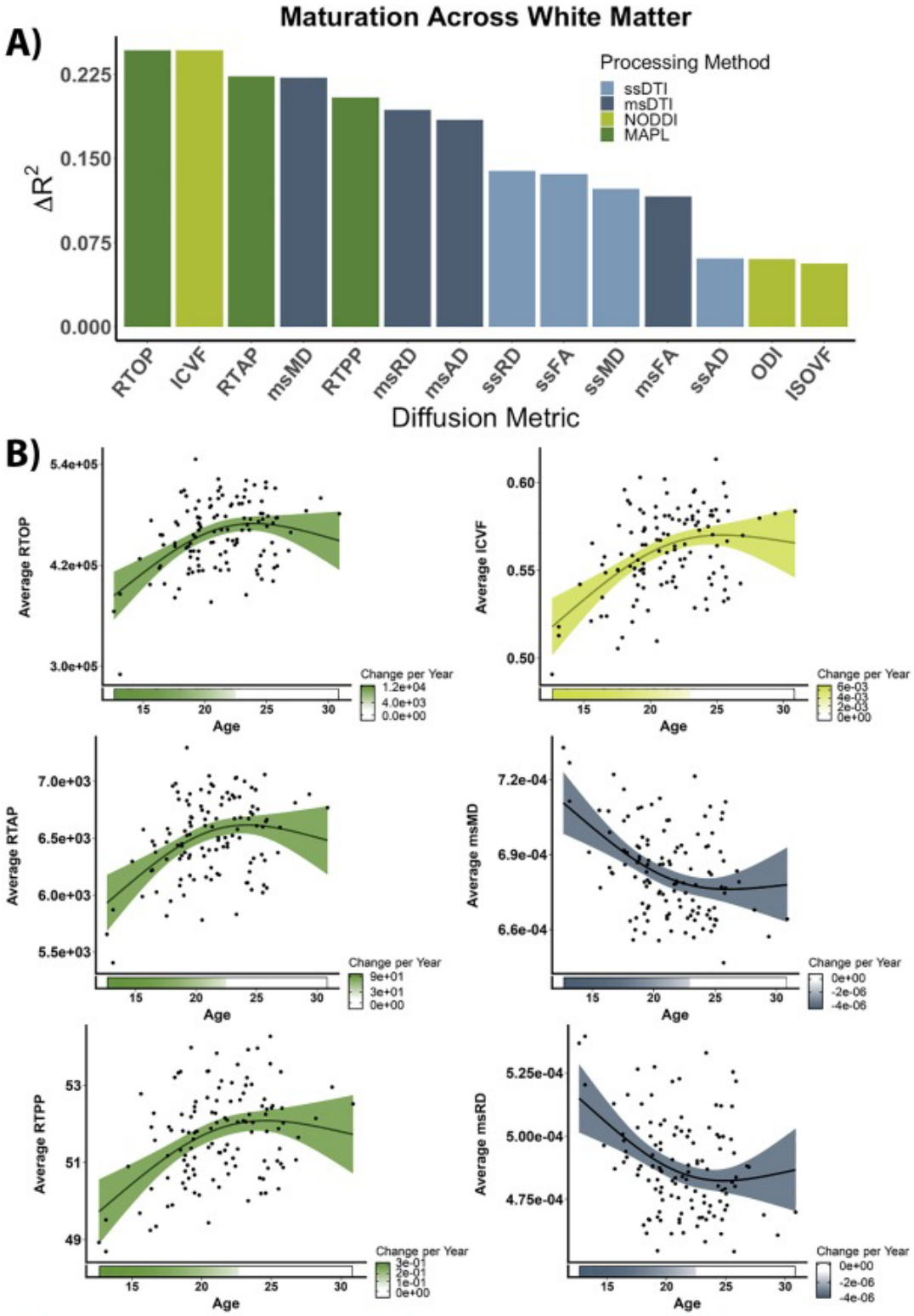


**ssFA**: Single-shell fractional anisotropy, **ssMD**: Single-shell mean diffusivity, **ssRD**: Single-shell radial diffusivity, **ssAD**: Single-shell axial diffusivity, **msFA**: Multi-shell fractional anisotropy, **msMD**: Multi-shell mean diffusivity, **msAD**: Multi-shell axial diffusivity, **msRD**: Multi-shell radial diffusivity, **ICVF**: Intracellular volume fraction, **ISOVF**: Isotropic volume fraction, **ODI**: Orientation dispersion index, **RTOP**: Return-to-origin probability, **RTAP**: Return-to-axis probability, **RTPP**: Return-to-plane probablity.

Figure 2.3 Diffusion models leveraging multi-shell data show variable associations with age in white matter. **A**. Change in $R^2$ after the addition of linear, quadratic, and cubic age terms for each diffusion metric. Models included head motion and sex as linear covariates. **B**. Relationships between mean white matter values and age, after controlling for sex and data quality. GAMs were leveraged to more precisely estimate linear and non-linear effects as one spline. The derivative of these splines, representing the estimated rate of change, are depicted below the x-axis. Shaded area indicates where the confidence interval of the slope does not include 0.

Table 2.1 Statistical relationships between mean white matter values and age for each metric. The second and third columns contains the *F*-statistic and *p*-value derived from the penalized spline for age in each GAM. The fourth column contains change in $R^2$ between polynomial models only accounting for sex and head motion effects and those that include age terms as well. The last column represents the age range at which the 95 % confidence interval for the estimated age effect does not include 0 in each GAM.

| **Metric** | $F_{Age}$ | $p_{Age}$ | $\Delta R^2$ | **Age Spline Slope CI ≠ 0** |
|---|---|---|---|---|
| **msFA** | 4.24 | 0.034 | 0.116 | 12.7−21.3 |
| **msMD** | 14.04 | $1.20 \times 10^{-5}$ | 0.222 | 12.7−22.9 |
| **msAD** | 14.37 | $2.07 \times 10^{-5}$ | 0.184 | 12.7−23.8 |
| **msRD** | 10.33 | $2.16 \times 10^{-4}$ | 0.193 | 12.7−22.4 |
| **ssFA** | 4.91 | 0.018 | 0.136 | 12.7−21.4 |
| **ssMD** | 6.12 | 0.001 | 0.123 | 12.7−22.2 |
| **ssAD** | 6.57 | 0.012 | 0.061 | NA |
| **ssRD** | 5.83 | 0.010 | 0.139 | 12.7−21.9 |
| **ICVF** | 18.23 | $3.41 \times 10^{-7}$ | 0.246 | 12.7−23.0 |
| **ODI** | 5.66 | 0.019 | 0.060 | NA |
| **ISOVF** | 5.55 | 0.020 | 0.057 | NA |
| **RTOP** | 15.20 | $2.77 \times 10^{-6}$ | 0.247 | 12.7−22.4 |
| **RTAP** | 13.17 | $1.64 \times 10^{-5}$ | 0.223 | 12.7−22.4 |
| **RTPP** | 13.87 | $1.01 \times 10^{-5}$ | 0.204 | 12.7−22.6 |

Tractwise analyses revealed a similar pattern of effects to whole brain analyses, further suggesting enhanced developmental sensitivity of multi-shell derived metrics. Voxelwise analyses within white matter yielded more heterogenous results. While some metrics demonstrated only sparse associations with age, RTOP, ICVF, and MD derived from all of the shells displayed widespread effects encompassing thousands of voxels (Fig. 2.4).

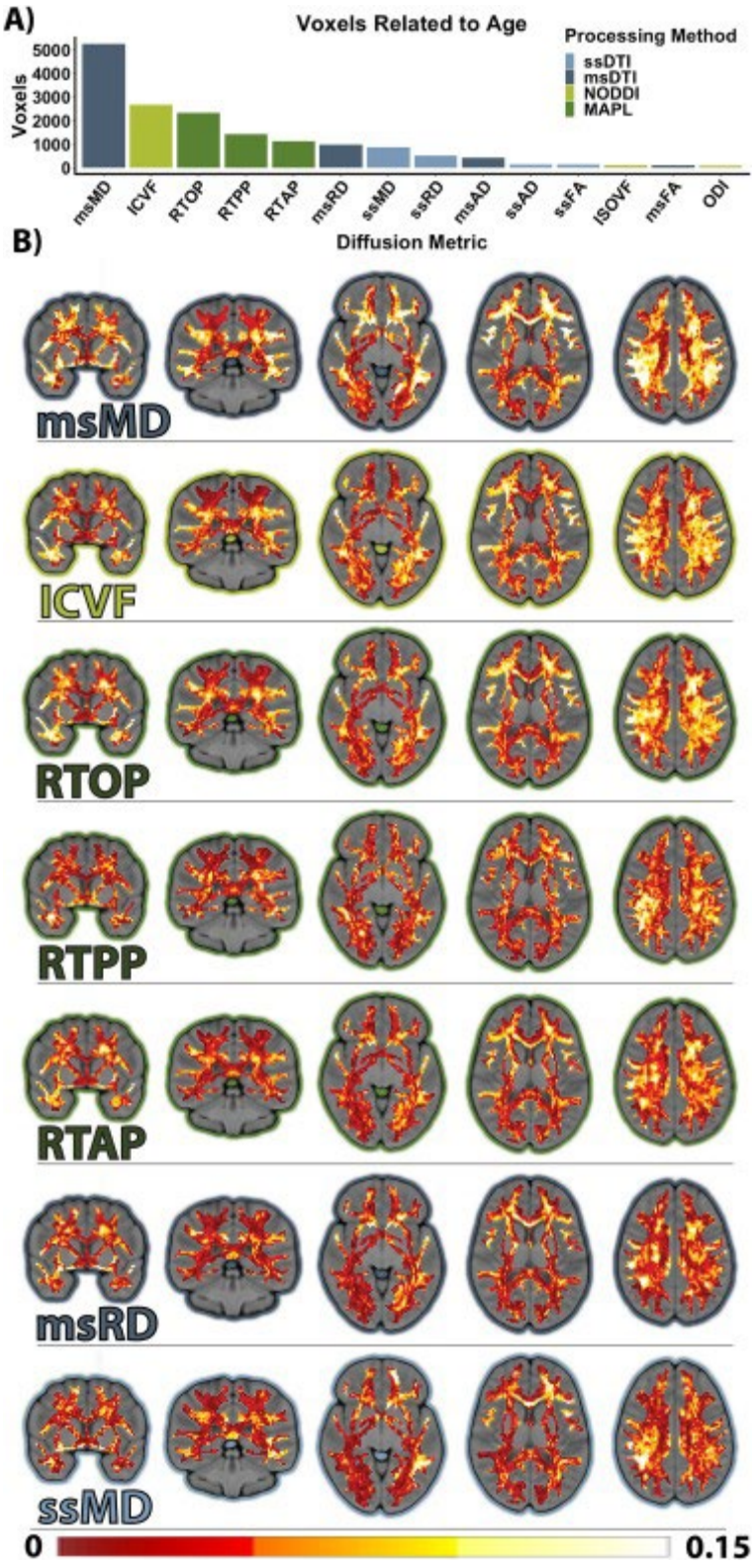
A)
Voxels Related to Age
Processing Method
ssDTI
msDTI
NODDI
MAPL
Voxels
5000
4000
3000
2000
1000
0
msMD
ICVF
RTOP
RTPP
RTAP
msRD
ssMD
ssRD
msAD
ssAD
ssFA
ISOVF
msFA
ODI
B)
Diffusion Metric
msMD
ICVF
RTOP
RTPP
RTAP
msRD
ssMD
0
0.15

Figure 2.4 Regional patterns of neurodevelopment are differentially associated with diffusion metrics. **A**. Number of voxels related to age (threshold of $p < 0.001$, uncorrected). **B.** The 7 diffusion metrics yielding the most voxels associated with age. Voxel color depicts age effect sizes ($\Delta R^2$) at each voxel. Note that the color bar only extends to 0.15 for equitable contrast across metrics, but many voxels demonstrated higher changes in $R^2$ ($msMD_{max} = 0.44$, $ICVF_{max} = 0.30$, $RTOP_{max} = 0.59$).

### 3.3. Estimates of network development vary according to diffusion metric

Given that tools from network science are increasingly used to study the developing brain, we next evaluated associations with age within networks where edges were weighted by diffusion metrics. These analyses yielded similar results to the voxelwise analyses described above, with network edges weighted by ICVF, RTPP, msMD, and RTOP displaying the most associations with age (Fig. 2.5).

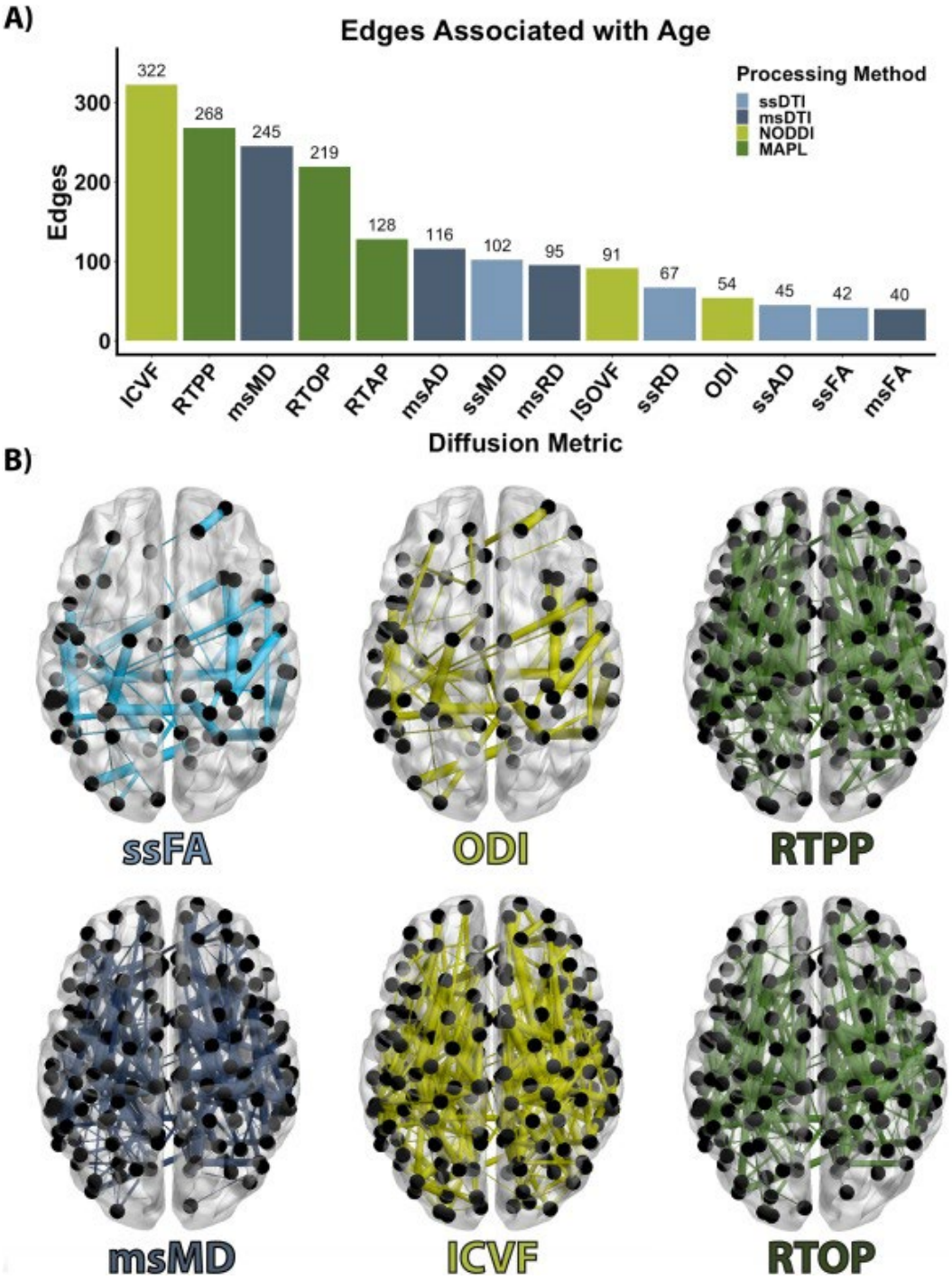


Figure 2.5. Scalar-weighted structural networks show differential associations with age. **A**. Number of edges that displayed significant associations with age while controlling for sex and head motion. **B**. Associations between age and selected structural networks; thickness of edges is scaled to their transformed *p*-values, with lower *p*-values depicted by thicker edges.

### 3.4. Diffusion measures are differentially impacted by data quality

As a final step, we sought to characterize the impact of motion on all diffusion metrics. Evaluation of mean white matter values revealed that several diffusion measures were related to head motion after controlling for age and sex, including FA, RD, ssMD, ODI, and ISOVF (Table 2.2, Fig. 2.6). We observed similar patterns at the voxel level, with MAPL metrics and AD being least impacted by motion. Analyses of networks weighted by each of these values revealed relatively similar associations with head motion across metrics, except for ISOVF, which had 118 edges significantly associated with head motion.

Table 2.2 Head motion and diffusion metric relations. All correlations were obtained after controlling for age and sex effects, and were derived from mean white matter values. Motion-metric relations were evaluated for statistical significance at the $p < 0.001$ level across all voxels and edges.

| Metric | Global White Matter $r_{relRMS}$ | Global White Matter $p_{relRMS}$ | # Voxels Related to motion ($p<0.001$) | # Edges Related to motion ($p<0.001$) |
|---|---|---|---|---|
| **msFA** | −0.30 | $7.8 \times 10^{-4}$ | 143 | 48 |
| **msMD** | 0.17 | 0.070 | 116 | 52 |
| **msAD** | −0.07 | 0.452 | 57 | 49 |
| **msRD** | 0.26 | $4.9 \times 10^{-3}$ | 220 | 51 |
| **ssFA** | −0.22 | 0.017 | 113 | 45 |
| **ssMD** | 0.23 | 0.013 | 278 | 54 |
| **ssAD** | 0.11 | 0.219 | 102 | 53 |
| **ssRD** | 0.25 | 0.006 | 210 | 49 |
| **ICVF** | 0.05 | 0.571 | 138 | 48 |
| **ODI** | 0.40 | $7.7 \times 10^{-6}$ | 162 | 59 |

| Metric | Global White Matter $r_{relRMS}$ | Global White Matter $p_{relRMS}$ | # Voxels Related to motion ($p$<0.001) | # Edges Related to motion ($p$<0.001) |
|---|---|---|---|---|
| **ISOVF** | 0.39 | $1.33 \times 10^{-5}$ | 480 | 118 |
| **RTOP** | −0.03 | 0.726 | 54 | 42 |
| **RTAP** | −0.15 | 0.114 | 114 | 44 |
| **RTPP** | 0.03 | 0.767 | 71 | 50 |

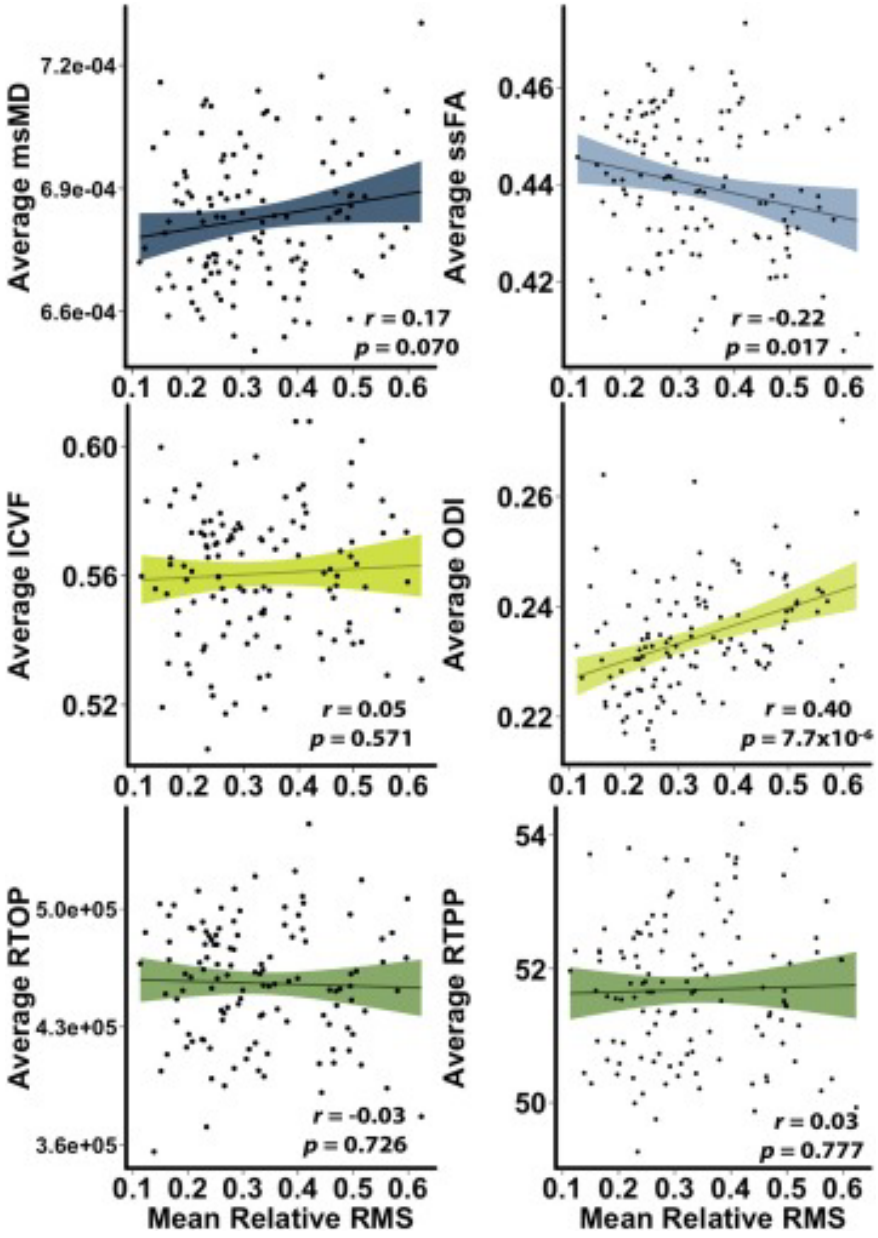


Figure 2.6 Mean measures of diffusion are differentially impacted by in-scanner motion. Selected measures displayed; see Table 2 for full results. All analyses control for age and sex.

## 4. Discussion

Our findings suggest that diffusion models leveraging multi-shell data have important advantages for studying the developing brain. These advantages include increased sensitivity to developmental effects and reduced impact of in-scanner motion. Benefits of multi-shell data were

present at multiple scales, including mean white matter values, white matter tracts, voxelwise analyses, and network edges. The context, implications, and limitations of these results are discussed below.

### 4.1. Metrics derived from multi-shell data demonstrate superior sensitivity to brain development

In our dataset, diffusion models that leveraged the full multi-shell acquisition had strong associations with age. For some metrics, stronger age associations were present despite relatively high correlations with equivalent single-shell metrics (Fig. 2.2B). This discrepancy implies that the unique diffusion patterns captured by multi-shell measures may drive associations with age. Specifically, the "slow" diffusion elicited by higher *b*-values (Stanisz et al., 1997) may change more with age than water diffusion patterns observed at *b*-values typically used in single-shell sequences. Indeed, additional recent evidence also suggests that high *b*-value diffusion images may be more sensitive to age effects in many white matter tracts (Genc et al., 2020). Some metrics, like RTPP, were robustly related to age but not highly correlated with other metrics. Because RTPP may capture specific white matter properties, it could be particularly useful as a complementary measure in studies using multiple diffusion metrics to characterize microstructure (Chamberland et al., 2019).

The similar neurodevelopmental patterns observed across the majority of diffusion metrics implicate a common pattern of microstructural changes that plateau in the early 20's. Prior work has strongly suggested continued myelination throughout adolescence and into adulthood (Lebel et al., 2008; Asato et al., 2010), and persistent myelination may, at least in part, explain developmental effects observed here. However, other important neurobiological factors can affect diffusion properties independent of myelination. Among other factors, increased axonal packing may also contribute to restricted diffusion over neurodevelopment (Neil et al., 2002; Beaulieu, 2002).

In contrast to NODDI, MAPL, and DTI metrics derived from all shells, single-shell DTI metrics tended to demonstrate fewer age associations across all analyses. Although these metrics were

calculated from less diffusion directions than their multi-shell counterparts, DTI-based neurodevelopmental inquiries have effectively characterized microstructure with far fewer sampling directions (Lebel et al., 2008). It is important to consider that the diffusion tensor model does not explicitly account for the non-gaussianity of water diffusion that is common at higher *b*-values. While our estimates of single-shell DTI, NODDI, and MAPL values aligned with previous literature (Lebel et al., 2008; Zhang et al., 2012; Fick et al., 2016a), the combination of high *b*-value data and the DTI model likely produced the relatively low values of multi-shell DTI metrics. Despite limitations of using the DTI model with multi-shell data, most DTI-derived metrics fit using all shells demonstrated substantial associations with age, particularly MD. This indicates that complete fulfillment of the assumptions of gaussian diffusion underlying the diffusion tensor model may not be necessary for probing broad, albeit potentially non-specific, developmental effects.

These results move beyond previous findings in several respects. To our knowledge, this is the first study to demonstrate that MAPL-derived metrics are highly sensitive to brain development in youth. RTOP, RTAP, and RTPP likely reflect multifaceted aspects of water diffusion becoming more restricted as the brain develops. Age-related changes in RTOP likely reflect aggregate water restriction from developmental factors like myelination and axonal packing (Aung et al., 2013; Beaulieu, 2002; Feldman et al., 2010; Neil et al., 2002), as RTOP is equally sensitive to water movement in all directions in all voxels. However, the neurodevelopmental effects that RTAP and RTPP track may reflect more specific fiber geometry in addition to generalized diffusion restriction. RTAP tracks water displacement from the principal axis of diffusion in a voxel. In white matter voxels with unidirectional fiber populations, RTAP is thought to correspond to cross-sectional area of cylindrically-shaped cellular compartments. Conversely, RTPP tracks water displacement from the plane that is perpendicular to that principal axis of diffusion and may correspond to the length of cellular compartments along that axis (Özarslan et al., 2013). However, like DTI (Volz et al., 2018; Jeurissen et al., 2013; Wheeler-Kingshott and Cercignani, 2009) and NODDI (Farooq et al., 2016), the neurobiological interpretation of MAPL metrics

changes in voxels with crossing fibers. Efforts to explicitly model crossing fibers will undoubtedly play a role in disambiguating the relationship between diffusion metrics and fiber properties (Volz et al., 2018; Farooq et al., 2016; Raffelt et al., 2015).

Second, our results demonstrate that multi-shell measures of structural brain network connectivity, such as ICVF and RTPP, are more strongly associated with age than traditional FA-weighted networks. This result builds upon prior studies, which have shown that ICVF derived from NODDI is more strongly associated with age than traditional measures such as FA (Chang et al., 2015; Genc et al., 2017; Ota et al., 2017), and that weighting streamlines with DTI and NODDI metrics may offer complementary information (Deligianni et al., 2016). As previous developmental studies have indicated, these advantages may be driven by greater biological specificity from multi-shell models (Chang et al., 2015; Eaton-Rosen et al., 2015; Mah et al., 2017; Timmers et al., 2016). Overall, the age associations we have presented across analyses emphasize the utility of multi-shell data for studying brain development. These advantages of multi-shell data likely stem from the ability to successfully capture differential tissue responses across *b*-values and the evolution of complex white matter architecture during development (Jeurissen et al., 2013; Volz et al., 2018).

### 4.2. MAPL metrics are less impacted by head motion than NODDI and DTI

As children are more likely to move during scanning than adults, motion artifact remains a major concern for studies of brain development (Theys et al., 2014; Satterthwaite et al., 2012; Satterthwaite et al., 2013; Fair et al., 2012). For diffusion imaging and other sequences, the primary determinant of scan quality for diffusion imaging is in-scanner head motion (Yendiki et al., 2014; Ling et al., 2012). Importantly, higher in-scanner motion was associated with reduced mean white matter FA, and increased MD, RD, ODI, and ISOVF while accounting for age. This finding aligns with prior reports of in-scanner motion systematically impacting DTI metrics (Yendiki et al., 2014; Ling et al., 2012; Roalf et al., 2016; Baum et al., 2018).

However, to our knowledge there has been no prior work documenting the impact of in-scanner head motion on ODI and ISOVF, or any measure derived from MAPL. ODI and ISOVF were both significantly positively correlated with in-scanner head motion. Investigators should consider and account for this confound when utilizing the NODDI model. Notably, measures derived from MAPL were minimally impacted by motion. This may be due to the Laplacian signal regularization in MAPL, which was designed to mitigate the impact of noise in DWI acquisitions. Especially when considered alongside the robust associations between MAPL-derived measures and age, noise-resistance may strengthen the rationale for using MAPL in studies of brain development.

### 4.3. Limitations and future directions

Several limitations should be noted. First, our results were only derived from one study. Replication of these results using multiple datasets, scanners, and acquisition schemes would strengthen evidence for the relative advantages of multi-shell models. Specifically, MAPL has typically been fit on data with *b*-value shells higher than 2000, raising the possibility that it may perform better in acquisitions with $b$ = 3000 shells (including those used for the HCP and ABCD efforts) (Özarslan et al., 2013; Fick et al., 2016a; Casey et al., 2018). A second limitation of our study is the lack of cellular specificity, which is a limitation of all non-invasive imaging techniques. However, several *ex vivo* studies of NODDI have suggested a degree of histological correspondence (Schiling et al., 2018; Sato et al., 2017; Grussu et al., 2017). Notably, although MAPL is also sensitive to cellular-level properties, it does not use an explicit model of tissue compartments like NODDI. However, preliminary animal work has tied MAPL diffusion metrics to neurodegenerative tissue abnormalities (Fick et al., 2016b). Third, we used deterministic DTI-based tractography to define streamlines, which results in a sparse structural network biased towards major white matter tracts. While these network analyses demonstrated enhanced associations with several diffusion metrics, networks constructed using multi-fiber tractography techniques might provide additional advantages (Maier-Hein et al., 2017; Reddy and Rathi, 2016; Farooq et al., 2016; Christiaens et al., 2015; Bonilha et al., 2015). Finally, our study mainly

included young adults and older adolescents. Studies of younger children would provide complementary data, as prior literature in younger ages has demonstrated dramatic changes in FA during childhood and early adolescence (Lebel et al., 2008; Simmonds et al., 2014). Consequently, we anticipate that inclusion of younger participants could yield stronger FA-measured effects than those observed in our sample. Despite the relatively older age range of our sample, our results demonstrate that diffusion metrics incorporating tissue responses across multiple *b*-values are sensitive to protracted neurodevelopmental processes that single-shelled metrics may not be able to discern.

### 4.4. Conclusion

In summary, we provide novel evidence that diffusion metrics are differentially associated with age and motion in youth. Measures that are more tightly linked to brain maturation and less related to data quality are likely to be particularly useful for developmental studies or clinical samples. Through free open-access software, these advanced diffusion methods are relatively easy for investigators to implement (Alimi et al., 2018; Daducci et al., 2015; Fick et al., 2018; Garyfallidis et al., 2014). In the context of these results, we anticipate that multi-shell diffusion models will be increasingly adopted by the developmental and clinical neuroscience community.

**Acknowledgements**

This work was supported by grants from the National Institute of Mental Health: R01MH107703, R01MH113550, R01MH112847, R21MH106799, RF1MH116920, and F31 MH115709. Additional support was provided by the AE Foundation, the Center for Biomedical Computing and Image Analysis (CBICA) at Penn, and the Penn/CHOP Lifespan Brain Institute.

**5. Bibliography**

Alexander, D.C., Hubbard, P.L., Hall, M.G., Moore, E.A., Ptito, M., Parker, G.J.M., Dyrby, T.B., 2010. Orientationally invariant indices of axon diameter and density from diffusion mri. NeuroImage 52 (4), 1374–1389.

Alexander, D.C., Dyrby, T.B., Nilsson, M., Zhang, H., 2017. Imaging brain microstructure with diffusion mri: practicality and applications. NMR Biomed.

Alimi, A., Fick, R., Wassermann, D., Deriche, R., 2018. Dmipy, A Diffusion Microstructure Imaging Toolbox in Python to Improve Research Reproducibility. htt ps://hal.inria.fr/hal-01873353/document.

Andersson, J.L.R., Graham, M.S., Zsoldos, E., Sotiropoulos, S.N., 2016. Incorporating outlier detection and replacement into a non-parametric framework for movement and distortion correction of diffusion MR images. NeuroImage 141, 556–572.

Andersson, J.L.R., Graham, M.S., Drobnjak, I., Zhang, H., Filippini, N., Bastiani, M., 2017. Towards a comprehensive framework for movement and distortion correction of diffusion MR images: within volume movement. Neuroimage 152, 450–466.

Asato, M.R., Terwilliger, R., Woo, J., Luna, B., 2010. White matter development in adolescence: a DTI study. Cereb. Cortex 20 (9), 2122–2131.

Assaf, Y., Basser, P.J., 2005. Composite hindered and restricted model of diffusion (Charmed) MR imaging of the human brain. NeuroImage 27 (1), 48–58.

Assaf, Y., Ofer, P., 2008. Diffusion tensor imaging (DTI)-based white matter mapping in brain research: a review. J. Mol. Neurosci. 34 (1), 51–61.

Aung, W.Y., Mar, S., Benzinger, T.L., 2013. Diffusion tensor MRI as a biomarker in axonal and myelin damage. Imaging Med. 5 (5), 427–440.

Avants, B.B., Tustison, N.J., Song, G., Cook, P.A., Klein, A., Gee, J.C., 2011a. A reproducible evaluation of ants similarity metric performance in brain image registration. NeuroImage 54 (3), 2033–2044.

Avants, B.B., Tustison, N.J., Wu, J., Cook, P.A., Gee, J.C., 2011b. An open source multivariate framework for n-tissue segmentation with evaluation on public data. Neuroinformatics 9 (4), 381–400.

Baker, S.T.E., Lubman, D.I., Yücel, M., Allen, N.B., Whittle, S., Fulcher, B.D., Zalesky, A., Fornito, A., 2015. Developmental changes in brain network hub connectivity in late adolescence. J. Neurosci. 35 (24), 9078–9087.

Basser, P.J., Pierpaoli, C., 1996. Microstructural and physiological features of tissues elucidated by quantitative-diffusion-tensor MRI. J. Magn. Reson. B 111 (3), 209–219.

Basser, P.J., Mattiello, J., Le Bihan, D., 1994. MR diffusion tensor spectroscopy and imaging. Biophys. J. 66 (1), 259–267.

Basser, P.J., Pajevic, S., Pierpaoli, C., Duda, J., Aldroubi, A., 2000. In vivo fiber

tractography using DT-MRI data. Magn. Reson. Med. 44 (4), 625–632.

Bassett, D.S., Zurn, P., Gold, J.I., 2018. On the nature and use of models in network neuroscience. Nat. Rev. Neurosci. 19 (9), 566.

Bastiani, M., Shah, N.J., Goebel, R., Roebroeck, A., 2012. Human cortical connectome reconstruction from diffusion weighted MRI: the effect of tractography algorithm. NeuroImage 62 (3), 1732–1749.

Baum, G.L., Ciric, R., Roalf, D.R., Betzel, R.F., Moore, T.M., Shinohara, R.T., Kahn, A.E., Vandekar, S.N., Rupert, P.E., Quarmley, M., Cook, P.A., Elliott, M.A., Ruparel, K., Gur, R.E., Gur, R.C., Bassett, D.S., Satterthwaite, T.D., 2017. Modular segregation of structural brain networks supports the development of executive function in youth. Curr. Biol. 27 (11), 1561–1572.

Baum, G.L., Roalf, D.R., Cook, P.A., Ciric, R., Rosen, A.F.G., Xia, C., Elliott, M.A., Ruparel, K., Verma, R., Tunç, B., Gur, R.C., Gur, R.E., Bassett, D.S., Satterthwaite, T. D., 2018. The impact of in-scanner head motion on structural connectivity derived from diffusion MRI. NeuroImage 173, 275–286.

Beaulieu, C., 2002. The basis of anisotropic water diffusion in the nervous system—a technical review. NMR Biomed. 15 (7–8), 435–455.

Bonilha, L., Gleichgerrcht, E., Fridriksson, J., Rorden, C., Breedlove, J.L., Nesland, T., Paulus, W., Helms, G., Focke, N.K., 2015. Reproducibility of the structural brain

connectome derived from diffusion tensor imaging. PLoS One 10 (9), e0135247.

Casey, B.J., Cannonier, T., Conley, M.I., Cohen, A.O., Barch, D.M., Heitzeg, M.M., Soules, M.E., Teslovich, T., Dellarco, D.V., Garavan, H., Orr, C.A., Wager, T.D., Banich, M.T., Speer, N.K., Sutherland, M.T., Riedel, M.C., Dick, A.S., Bjork, J.M., Thomas, K.M., Chaarani, B., Mejia, M.H., Hagler, D.J., Cornejo, M.D., Sicat, C.S., Harms, M.P., Dosenbach, N.U.F., Rosenberg, M., Earl, E., Bartsch, H., Watts, R., Polimeni, J.R., Kuperman, J.M., Fair, D.A., Dale, A.M., the ABCD Imaging Acquisition Workgroup, 2018. The adolescent brain cognitive development (ABCD) study: imaging acquisition across 21 sites. Dev. Cogn. Neurosci.

Chamberland, M., Raven, E.P., Genc, S., Duffy, K., Descoteaux, M., Parker, G.D., Tax, C. M.W., Jones, D.K., 2019. Dimensionality reduction of diffusion MRI measures for improved tractometry of the human brain. NeuroImage 200, 89–100.

Chang, Y.S., Owen, J.P., Pojman, N.J., Thieu, T., Bukshpun, P., Wakahiro, M.L.J., Berman, J.I., 2015. White matter changes of neurite density and fiber orientation dispersion during human brain maturation. PLoS One 10 (6), e0123656.

Christiaens, D., Reisert, M., Dhollander, T., Sunaert, S., Suetens, P., Maes, F., 2015. Global tractography of multi-shell diffusion-weighted imaging data using a multi-tissue model. Neuroimage 123, 89–101.

Clark, C.A., Hedehus, M., Moseley, M.E., 2002. In vivo mapping of the fast and slow

diffusion tensors in human brain. Magn. Reson. Med. 47 (4), 623–628.

Cook, P.A., Bai, Y., Nedjati-Gilani, S., Seunarine, K.K., Hall, M.G., Parker, G.J., Alexander, D.C., 2006. Camino: Open-source diffusion-mri reconstruction and processing. In: 14th Scientific Meeting of the International Society for Magnetic Resonance in Medicine. Seattle, WA, USA, p. 2759.

Daducci, A., Canales-Rodríguez, E.J., Zhang, H., Dyrby, T.B., Alexander, D.C., Thiran, J. P., 2015. Accelerated microstructure imaging via convex optimization (Amico) from diffusion mri data. NeuroImage 105, 32–44.

De Santis, S., Drakesmith, M., Bells, S., Assaf, Y., Jones, D.K., 2014. Why diffusion tensor MRI does well only some of the time: Variance and covariance of white matter tissue microstructure attributes in the living human brain. NeuroImage 89, 35–44.

Deligianni, F., Carmichael, D.W., Zhang, H., Clark, C.A., Clayden, J.D., 2016. NODDI and tensor-based microstructural indices as predictors of functional connectivity. PLoS One 11 (4), e0153404.

Descoteaux, M., Angelino, E., Fitzgibbons, S., Deriche, R., 2007. Regularized, fast, and robust analytical q-ball imaging. Magn. Reson. Med. 58 (3), 497–510.

Eaton-Rosen, Z., Melbourne, A., Orasanu, E., Cardoso, M.J., Modat, M., Bainbridge, A., Kendall, G.S., Robertson, N.J., Marlow, N., Ourselin, S., 2015. Longitudinal measurement of the developing grey matter in preterm subjects using multi-modal

MRI. NeuroImage 111, 580–589.

Fair, D.A., Nigg, J.T., Iyer, S., Bathula, D.R., Mills, K.L., Dosenbach, N.U.F., Schlaggar, B. L., Mennes, M., Gutman, D., Bangaru, S., Buitelaar, J.K., Dickstein, D.P., Di Martino, A., Kennedy, D.N., Kelly, C., Luna, B., Schweitzer, J.B., Velanova, K., Wang, Y.-F., Mostofsky, S., Castellanos, X.F., Milham, M.P., 2012. Distinct neural signatures detected for ADHD subtypes after controlling for micro-movements in resting state functional connectivity MRI data. Front. Syst. Neurosci. 6, 80.

Fan, Y., Shi, F., Smith, J.K., Lin, W., Gilmore, J.H., Shen, D., 2011. Brain anatomical networks in early human brain development. NeuroImage 54 (3), 1862–1871.

Farooq, H., Xu, J., Nam, J.W., Keefe, D.F., Yacoub, E., Georgiou, T., Lenglet, C., 2016. Microstructure imaging of crossing (MIX) white matter fibers from diffusion MRI. Sci. Rep. 6, 38927.

Feldman, H.M., Yeatman, J.D., Lee, E.S., Barde, L.H.F., Gaman-Bean, S., 2010. Diffusion Tensor Imaging: A Review for Pediatric Researchers and Clinicians. J. Dev. Behav. Pediatr. 31 (4), 346–356.

Ferizi, U., Scherrer, B., Schneider, T., Alipoor, M., Eufracio, O., Fick, R.H.J., Deriche, R., Nilsson, M., Loya-Olivas, A.K., Rivera, M., Poot, D.H.J., Ramirez-Manzanares, A., Marroquin, J.L., Rokem, A., P€otter, C., Dougherty, R.F., Sakaie, K., Wheeler-Kingshott, C., Warfield, S.K., Witzel, T., Wald, L.L., Raya, J.G., Alexander, D.C.,

2017. Diffusion mri microstructure models with in vivo human brain connectome data: results from a multi-group comparison. NMR Biomed. 30 (9).

Fick, R.H.J., Wassermann, D., Caruyer, E., Deriche, R., 2016a. MAPL: tissue microstructure estimation using laplacian-regularized MAP-MRI and its application to HCP data. NeuroImage 134, 365–385.

Fick, R., Daianu, M., Pizzolato, M., Wassermann, D., Jacobs, R.E., Thompson, P.M., Town, T.C., Deriche, R., 2016b. Comparison of Biomarkers in Transgenic Alzheimer Rats Using Multi-shell Diffusion MRI. MICCAI 2016.

Fick, R.H.J., Deriche, R., Wassermann, D., 2018. Dmipy: An Open-source Framework for Reproducible dMRI-Based Microstructure Research (Version 0.1). Zenodo.

Garyfallidis, E., Brett, M., Amirbekian, B., Rokem, A., Van Der Walt, S., Descoteaux, M., Nimmo-Smith, I., 2014. Dipy, a library for the analysis of diffusion MRI data. Front. Neuroinform. 8.

Genc, S., Malpas, C.B., Holland, S.K., Beare, R., Silk, T.J., 2017. Neurite density index is sensitive to age related differences in the developing brain. NeuroImage 148, 373–380.

Genc, S., Tax, M.W.C., Raven, E.P., Chamberland, M., Parker, G.D., Jones, D.K., 2020. Impact of b-value on estimates of apparent fibre density. Hum. Brain Mapp. 1–13.

Gollo, L.L., Roberts, J.A., Cropley, V.L., Di Biase, M.A., Pantelis, C., Zalesky, A.,

Breakspear, M., 2018. Fragility and volatility of structural hubs in the human connectome. Nat. Neurosci. 21 (8), 1107.

Grayson, D.S., Ray, S., Carpenter, S., Swathi Iyer Dias, T.C.G., Stevens, C., Nigg, J.T., Fair, D.A., 2014. Structural and functional rich club organization of the brain in children and adults. PLoS One 9 (2), e88297.

Greve, D.N., Fischl, B., 2009. Accurate and robust brain image alignment using boundary-based registration. NeuroImage 48 (1), 63–72.

Grussu, F., Schneider, T., Tur, C., Yates, R.L., Tachrount, M., Ianuş, A., Yiannakas, M.C., Newcombe, J., Zhang, G., Alexander, D.C., DeLuca, G.C., Gandini Wheeler-Kingshott, C.A.M., 2017. Neurite dispersion: a new marker of multiple sclerosis spinal cord pathology? Ann. Clin. Transl. Neurol. 4 (9), 663–679.

Hagmann, P., Sporns, O., Madan, N., Cammoun, L., Pienaar, R., Wedeen, V.J., Meuli, R., Thiran, J.P., Grant, P.E., 2010. White matter maturation reshapes structural connectivity in the late developing human brain. Proc. Natl. Acad. Sci. U. S. A. 107 (44), 19067–19072.

Huang, H., Shu, N., Mishra, V., Jeon, T., Chalak, L., Wang, Z.J., Rollins, N., Gong, G., Cheng, H., Peng, Y., Dong, Q., He, Y., 2015. Development of human brain structural networks through infancy and childhood. Cereb. Cortex 25 (5), 1389–1404.

Developmental Cognitive Neuroscience 43 (2020) 100788

11Jalbrzikowski, M., Larsen, B., Hallquist, M.N., Foran, W., Calabro, F., Luna, B., 2017. Development of white matter microstructure and intrinsic functional connectivity between the Amygdala and ventromedial prefrontal cortex: associations with anxiety and depression. Biol. Psychiatry 82 (7), 511–521.

Jenkinson, M., Beckmann, C.F., Behrens, T.E.J., Woolrich, M.W., Smith, S.M., 2012. FSL. NeuroImage 62 (2), 782–790.

Jeurissen, B., Leemans, A., Tournier, J., Jones, D.K., Sijbers, J., 2013. Investigating the prevalence of complex fiber configurations in white matter tissue with diffusion magnetic resonance imaging. Hum. Brain Mapp. 34 (11), 2747–2766.

Jones, D.K., Basser, P.J., 2004. Squashing peanuts and smashing pumpkins': how noise distorts diffusion-weighted MR data. Magn. Reson. Med. 52 (5), 979–993.

Jones, D.K., Cercignani, M., 2010. Twenty-five pitfalls in the analysis of diffusion MRI data. NMR Biomed. 23, 803–820.

Karmacharya, S., Gagoski, B., Ning, L., Vyas, R., Cheng, H.H., Soul, J., Newberger, J.W., Shenton, M.E., Rathi, Y., Grant, P.E., 2018. Advanced diffusion imaging for assessing normal white matter development in neonates and characterizing aberrant development in congenital heart disease. Neuroimage Clin. 19, 360–373.

Klein, A., Andersson, J., Ardekani, B.A., Ashburner, J., Avants, B., Chiang, M.,

Christensen, G.E., Collins, D.L., Gee, J., Hellier, P., Song, J.H., Jenkinson, M., Lepage, C., Rueckert, D., Thompson, P., Vercauteren, T., Woods, R.P., Mann, J.J., Parsey, R.V., 2009. Evaluation of 14 nonlinear deformation algorithms applied to human brain MRI registration. NeuroImage 46 (3), 786–802.

Kodiweera, C., Alexander, A.L., Harezlak, J., McAllister, T.W., Wu, Y.C., 2016. Age effects and sex differences in human brain white matter of young to middle-aged adults: a DTI, NODDI, and Q-space study. NeuroImage 128, 180–192.

Koh, D.M., Padhani, A.R., 2006. Diffusion-weighted MRI: a new functional clinical technique for tumour imaging. Br. J. Radiol. 79 (944), 633–635.

Larsen, B., Verstynen, T.D., Yeh, F.-C., Luna, B., 2018. Developmental changes in the integration of affective and cognitive corticostriatal pathways are associated with reward-driven behavior. Cereb. Cortex 28 (8), 2834–2845.

Lebel, C., Deoni, S., 2018. The development of brain white matter microstructure. NeuroImage 182, 207–218.

Lebel, C., Walker, L., Leemans, A., Phillips, L., Beaulieu, C., 2008. Microstructural maturation of the human brain from childhood to adulthood. NeuroImage 40 (3), 1044–1055.

Lebel, C., Treit, S., Beaulieu, C., 2017. A review of diffusion MRI of typical white matter development from early childhood to young adulthood. NMR Biomed. e3778.

Ling, J., Merideth, F., Caprihan, A., Pena, A., Teshiba, T., Mayer, A.R., 2012. Head injury or head motion? Assessment and quantification of motion artifacts in diffusion tensor imaging studies. Hum. Brain Mapp. 33 (1), 50–62.

Mah, A., Geeraert, B., Lebel, C., 2017. Detailing neuroanatomical development in late childhood and early adolescence using NODDI. PLoS One 12 (8), e0182340.

Maier-Hein, K.H., Neher, P.F., Houde, J.C., C^ot�e, M.A., Garyfallidis, E., Zhong, J., Chamberland, M., Yeh, F.C., Lin, Y.C., Ji, Q., Reddick, W.E., Glass, J.O., Chen, D.Q., Feng, Y., Gao, C., Wu, Y., Ma, J., Renjie, H., Li, Q., Westin, C.F., Deslauriers-Gauthier, S., Gonz�alez, J.O.O., Paquette, M., St-Jean, S., Girard, G., Rheault, F., Sidhu, J., Tax, C.M.W., Guo, F., Mesri, H.Y., D�avid, S., Froeling, M., Heemskerk, A. M., Leemans, A., Bor�e, A., Pinsard, B., Bedetti, C., Desrosiers, M., Brambati, S., Doyon, J., Sarica, A., Vasta, R., Cerasa, A., Quattrone, A., Yeatman, J., Khan, A.R., Hodges, W., Alexander, S., Romascano, D., Barakovic, M., Auría, A., Esteban, O., Lemkaddem, A., Thiran, J.P., Cetingul, H.E., Odry, B.L., Mailhe, B., Nadar, M.S., Pizzagalli, F., Prasad, G., Villalon-Reina, J.E., Galvis, J., Thompson, P.M., Requejo, F. D.S., Laguna, P.L., Lacerda, L.M., Barrett, R., Dell'Acqua, F., Catani, M., Petit, L., Caruyer, E., Daducci, A., Dyrby, T.B., Holland-Letz, T., Hilgetag, C.C., Stieltjes, B., Descoteaux, M., 2017. The challenge of mapping the human connectome based on diffusion tractography. Nat. Commun. 8, 1349.

Mori, S., Oishi, K., Jiang, H., Jiang, L., Li, X., Akhter, K., Hua, K., Faria, A.V., Mahmood, A., Woods, R., Toga, A.W., Pike, G.B., Neto, P.R., Evans, A., Zhang, J., Huang, H., Miller, M.I., Zijl, P., Mazziotta, J., 2008. Stereotaxic white matter atlas based on diffusion tensor imaging in an ICBM template. NeuroImage 40 (2), 570–582.

Nazeri, A., Chakravarty, M.M., Rotenberg, D.J., Rajji, T.K., Rathi, Y., Michailovich, O.V., Voineskos, A.N., 2015. Functional consequences of neurite orientation dispersion and density in humans across the adult lifespan. J. Neurosci. 35 (4), 1753–1762.

Neil, J., Miller, J., Mukherjee, P., Hüppi, P.S., 2002. Diffusion tensor imaging of normal and injured developing human brain—a technical review. NMR Biomed. 15 (7–8), 543–552.

Ota, M., Sato, N., Maikusa, N., Sone, D., Matsuda, H., Kunugi, H., 2017. Whole brain analyses of age-related microstructural changes quantified using different diffusional magnetic resonance imaging methods. J. Radiol. 1–6.

€Ozarslan, E., Koay, C.G., Shepherd, T.M., Komlosh, M.E., _Irfano�glu, M.O., Pierpaoli, C., Basser, P.J., 2013. Mean apparent propagator (MAP) MRI: a novel diffusion imaging method for mapping tissue microstructure. NeuroImage 78, 16–32.

R Core Team, 2013. R: A Language and Environment for Statistical Computing. R Foundation for Statistical Computing, Vienna, Austria. http://www.R-project.org/.

Raffelt, D.A., Smith, R.E., Ridgway, G.R., Tournier, J.-D., Vaughan, D.N., Rose, S., Henderson, R., Connelly, A., 2015. Connectivity-based fixel enhancement: whole-brain statistical analysis of diffusion MRI measures in the presence of crossing fibres. NeuroImage 117, 40–55.

Reddy, C.P., Rathi, Y., 2016. Joint multi-fiber NODDI parameter estimation and tractography using the unscented information filter. Front. Neurosci. 10.

Roalf, D.R., Quarmley, M., Elliott, M.A., Satterthwaite, T.D., Vandekar, S.N., Ruparel, K., Gennatas, E.D., Calkins, M.E., Moore, T.M., Hopson, R., Prabhakaran, K., Jackson, C. T., Verma, R., Hakonarson, H., Gur, R.C., Gur, R.E., 2016. The impact of quality assurance assessment on diffusion tensor imaging outcomes in a large-scale population-based cohort. NeuroImage 125, 903–919.

Sato, K., Kerever, A., Kamagata, K., Tsuruta, K., Irie, R., Tagawa, K., Okazawa, H., Arikawa-Hirasawa, E., Nitta, N., Aoki, I., Aoki, S., 2017. Understanding microstructure of the brain by comparison of neurite orientation dispersion and density imaging (NODDI) with transparent mouse brain. Acta Radiol. Open 6 (4).

Satterthwaite, T.D., Wolf, D.H., Loughead, J., Ruparel, K., Elliott, M.A., Hakonarson, H., Gur, R.C., Gur, R.E., 2012. Impact of in-scanner head motion on multiple measures of functional connectivity: relevance for studies of neurodevelopment in youth. NeuroImage 60 (1), 623–632.

Satterthwaite, T.D., Wolf, D.H., Ruparel, K., Erus, G., Elliott, M.A., Eickhoff, S.B., Gennatas, E.D., Jackson, C., Prabhakaran, K., Smith, A., Hakonarson, H., Verma, R., Davatzikos, C., Gur, R.E., Gur, R.C., 2013. Heterogeneous impact of motion on fundamental patterns of developmental changes in functional connectivity during youth. NeuroImage 83, 45–57.

Schaefer, A., Margulies, D.S., Lohmann, G., Gorgolewski, K.J., Smallwood, J., Kiebel, S. J., Villringer, A., 2014. Dynamic network participation of functional connectivity hubs assessed by resting-state fMRI. Front. Hum. Neurosci. 8.

Schiling, K.G., Janve, V., Gao, Y., Stepniewska, I., Landmann, B.A., Anderson, A.W., 2018. Histological validation of diffusion MRI fiber orientation distributions and dispersion. Neuroimage 165, 200–221.

Schmithorst, V.J., Yuan, W., 2010. White matter development during adolescence as shown by diffusion MRI. Brain Cognit. Adoles. Brain Dev. Curr. Themes Future Direct. 72 (1), 16–25.

Simmonds, D.J., Hallquist, M.N., Asato, M., Luna, B., 2014. Developmental stages and sex differences of white matter and behavioral development through adolescence: a longitudinal diffusion tensor imaging (DTI) study. NeuroImage 92, 356–368.

Soares, J.M., Marques, P., Alves, V., Sousa, N., 2013. A hitchhiker's guide to diffusion tensor imaging. Front. Neurosci. 7.

Sporns, O., Tononi, G., K€otter, R., 2005. The human connectome: a structural description of the human brain. PLoS Comput. Biol. 1 (4), e42.

Stanisz, G.J., Wright, G.A., Henkelman, R.M., Szafer, A., 1997. An analytical model of restricted diffusion in bovine optic nerve. Magn. Reson. Med. 37 (1), 103–111.

Svolos, P., Kousi, E., Kapsalaki, E., Theodorou, K., Fezoulidis, I., Kappas, C., Tsougos, I., 2014. The role of diffusion and perfusion weighted imaging in the differential diagnosis of cerebral tumors: a review and future perspectives. Cancer Imaging 14 (1), 20.

Theys, C., Wouters, J., Ghesquière, P., 2014. Diffusion tensor imaging and resting-state functional MRI-scanning in 5- and 6-year-old children: training protocol and motion assessment. PLoS One 9 (4), e94019.

Timmers, I., Roebroeck, A., Bastiani, M., Jansma, B., Rubio-Gozalbo, E., Zhang, H., 2016. Assessing microstructural substrates of white matter abnormalities: a comparative study using DTI and NODDI. PLoS One 11 (12).

Tournier, J.-D., Calamante, F., Connelly, A., 2012. MRtrix: Diffusion tractography in crossing fiber regions. Int. J. Imaging Syst. Technol. 22 (1), 53–66.

Tustison, N.J., Avants, B.B., Cook, P.A., Zheng, Y., Egan, A., Yushkevich, P.A., Gee, J.C., 2010. N4ITK: improved N3 bias correction. IEEE Trans. Med. Imaging 29 (6), 1310–1320.

Tustison, N.J., Cook, P.A., Klein, A., Song, G., Das, S.R., Duda, J.T., Kandel, B.M., van Strien, N., Stone, J.R., Gee, J.C., Avants, B.B., 2014. Large-scale evaluation of ants and freesurfer cortical thickness measurements. NeuroImage 99, 166–179.

Uddin, L.Q., Supekar, K.S., Ryali, S., Menon, V., 2011. Dynamic reconfiguration of structural and functional connectivity across core neurocognitive brain networks with development. J. Neurosci. 31 (50), 18578–18589.

Veerart, J., Sijbers, J., Sunaert, S., Leemans, A., Jeurissen, B., 2013. Weighted linear least squares estimations of diffusion MRI parameters: stengths, limitations, and pitfalls. NeuroImage 81, 335–346.

Volz, L.J., Cieslak, M., Grafton, S.T., 2018. A probabilistic atlas of fiber crossings for variability reduction of anisotropy measures. Brain Struct. Funct. 223 (2), 635–651.

Walter, G.G., 1977. Properties of hermite series estimation of probability density. Ann. Stat. 5 (6), 1258–1264.

Wheeler-Kingshott, C.A.M., Cercignani, M., 2009. About “axial” and “radial” diffusivities. Magn. Reson. Med. 61 (5), 1255–1260.

Wood, S.N., 2001. Mgcv: GAMs and generalized ridge regression for R. R News 1, 20–25.

Wood, S.N., 2004. Stable and efficient multiple smoothing parameter estimation for generalized additive models. J. Am. Stat. Assoc. 99, 673–686.

Wood, S.N., 2011. Fast stable restricted maximum likelihood and marginal likelihood

estimation of semiparametric generalized linear models. J. R. Stat. Soc. Ser. B 73 (1), 3–36.

Yendiki, A., Koldewyn, K., Kakunoori, S., Kanwisher, N., Fischl, B., 2014. Spurious group differences due to head motion in a diffusion MRI study. NeuroImage 88, 79–90.

Zhang, H., Schneider, T., Wheeler-Kingshott, C.A., Alexander, D.C., 2012. NODDI: practical in vivo neurite orientation dispersion and density imaging of the human brain. NeuroImage 61 (4), 1000–1016.

# CHAPTER 3: DISSOCIABLE MULTI-SCALE PATTERNS OF DEVELOPMENT IN PERSONALIZED BRAIN NETWORKS

## 1. Premise

In this study, we sought to understand how multi-scale cortical networks, occupying diverse positions across the sensorimotor-association hierarchy, mature with age to support EF. We evaluated the development of multi-scale personalized networks in a large sample of youth, with the goal of testing three interrelated hypotheses. First, we hypothesized that across scales, patterns of network development would vary across the sensorimotor-association hierarchy, with association networks exhibiting functional segregation relative to sensorimotor networks. Second, we predicted that association network segregation would relate to the maturation of EF in adolescence. Finally, we expected to find evidence of multi-scale network development. Specifically, given the diverse functions supported by brain organization at different scales, we anticipated that different network scales would have distinct associations with both age and EF.

## 2. Results

We studied 693 youths ages 8–23 years from the Philadelphia Neurodevelopmental Cohort, who completed fMRI at 3 T and had 27 min of high-quality data[41,45]. To derive multi-scale personalized functional networks, we used a specialized adaptation of non-negative matrix factorization (NMF) that incorporates spatial regularization[46,47] (see Methods). To ensure correspondence of personalized networks across participants, this process was initialized by creating a group atlas, which was then adapted to each individual's data (see Methods). To evaluate multiple resolutions, group atlases that included between 2 and 30 networks were created (Fig. 3.1). Across this range of scales, reconstruction error declined smoothly. To evaluate the degree to which finer-grained functional networks were nested within the network partitions obtained at the coarsest scale, we evaluated each network for its spatial overlap with

the group atlas derived at K = 2 networks. Across scales, ~57% of all networks fell within the unimodal partition, and 43% fell within the transmodal partition.

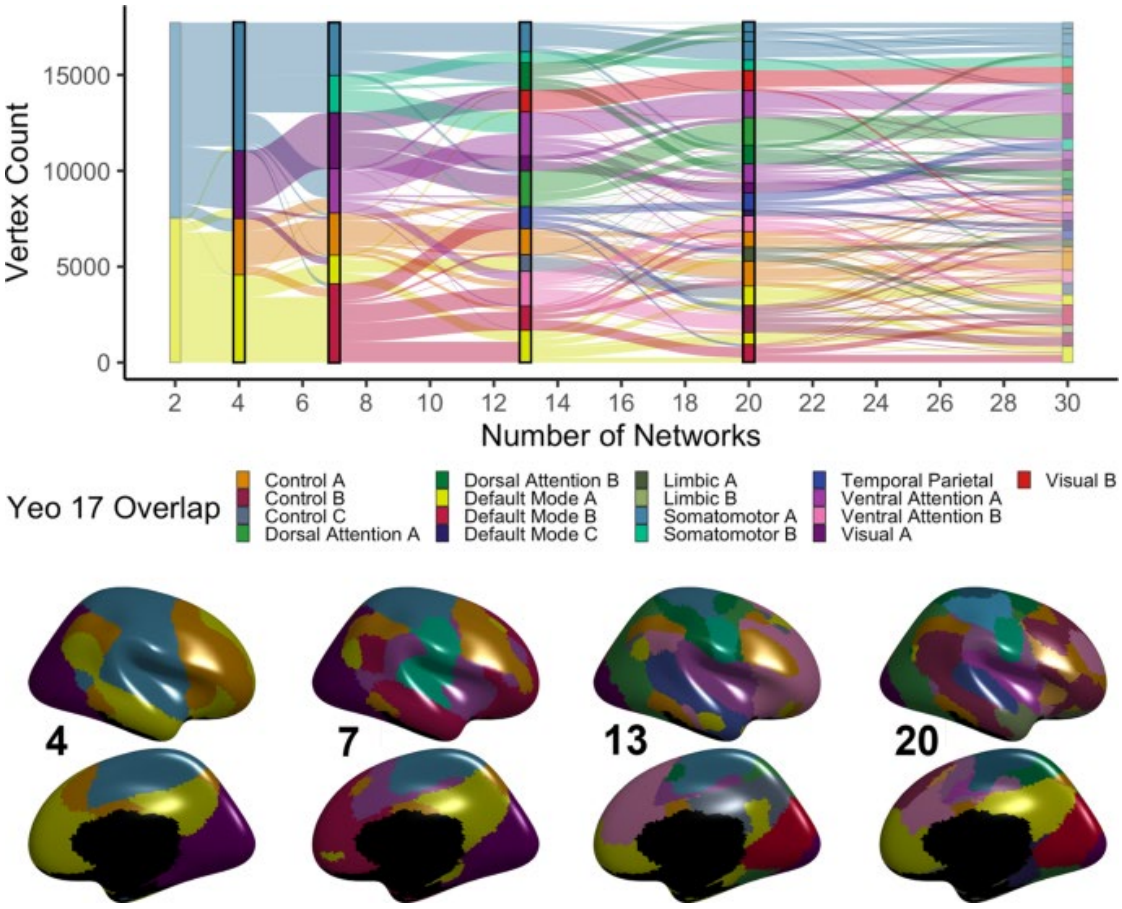


**Figure 3.1. Group-consensus functional networks at multiple scales.**

We used regularized non-negative matrix factorization to derive personalized functional networks at 29 scales (2–30 networks). Tracking network membership of each vertex across scales reveals a nested structure where finer-grained networks gradually emerge from coarse networks (top). Scales 4, 7, 13, and 20 are chosen for visualization; see bottom panel for cortical projections. Colors reflect each network's predominant overlap with a canonical atlas of 17 functional networks[84].

Examination of multi-scale personalized brain networks revealed prominent differences in person-specific functional neuroanatomy at all scales (Fig. 3.2a); networks were robust to NMF parameters chosen. Prior work at a single scale found that variability in functional neuroanatomy disproportionately localizes to association cortices[35,36,37,38,39]. Here, to quantify individual variability in-network topography, we calculated the median absolute deviation (MAD) of network loadings at each cortical vertex across participants. To verify that variability was consistently greater within association cortices at multiple scales, we compared network MAD at each scale to a widely used map summarizing a functional hierarchy, derived from the principal gradient of functional connectivity[17] (see Methods). Using a conservative spin-based spatial randomization procedure that accounts for spatial auto-correlation[48], we found that MAD was positively correlated with functional hierarchy in 27 of the 29 scales evaluated (Fig. 3.2b; green). Furthermore, we found that topographic variability became increasingly correlated with the hierarchy at finer scales (Fig. 3.2c; $r = 0.56$, $p_{boot} < 0.001$). These results demonstrate that variability in functional neuroanatomy is increasingly prominent within association cortices at finer-grained network resolutions.

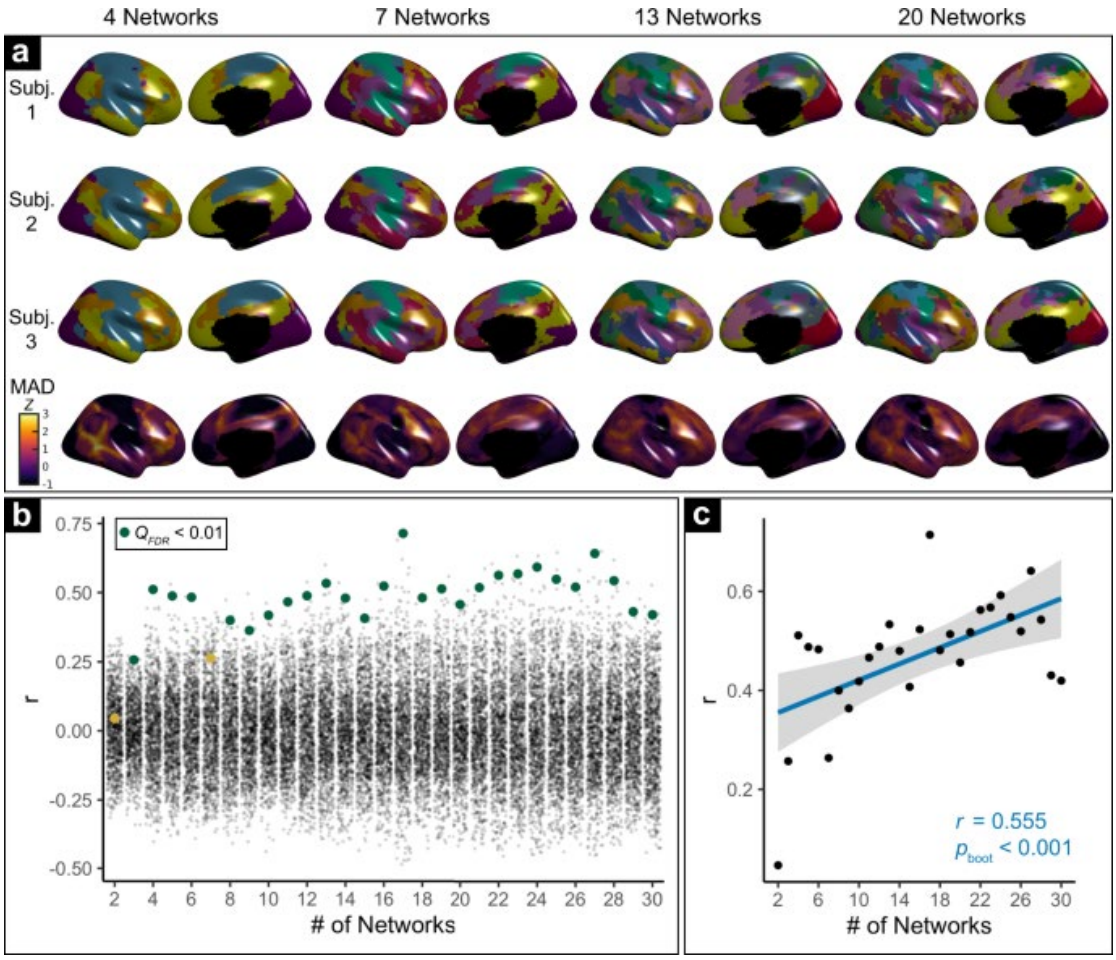


**Figure 3.2 Variability in personalized networks across scales.**

**a** Variability in personalized networks is greatest in association cortex across scales. Exemplar personalized networks at scales 4, 7, 13, and 20 are shown for three participants. Prominent individual differences in functional topography are present at all scales, as quantified by median absolute deviation (MAD) of functional network loadings across participants (bottom row, z-scored within each scale). **b** Variability of functional topography aligns with functional hierarchy. Spin-tests of the correlation between topographic variability and the principal functional connectivity gradient[17] at each scale reveal that variability is significantly correlated with a sensorimotor-to-association hierarchy at most scales (green dots = significant correlations; yellow dots = non-significant correlations; black dots = spin-test null correlations, FDR false discovery rate). **c** Greater alignment between a sensorimotor-to-association hierarchy and topographic

variability is present at finer scales. Scatterplot depicts second-order correlation of variability (MAD) and the principal gradient (from **b**) across scales. The statistical test is two-sided. Error bands depict the 95% confidence interval.

### 2.1 Brain network coupling develops according to a hierarchical sensorimotor-association axis

Having defined multi-scale personalized networks in a large sample of youth, we next sought to examine how network coupling evolves with age. To summarize the functional coupling of each network to other networks, we averaged between-network connectivity values across all personalized networks at each scale. We hypothesized that age-related changes in between-network coupling would vary according to a network's position on the sensorimotor-association functional hierarchy. To test this hypothesis, we first summarized each networks' position along the functional hierarchy, where higher values correspond to regions located in association cortices and lower values are assigned to regions in sensorimotor cortices (Fig. 3.3a). Specifically, the position of each network in the functional hierarchy was operationalized by extracting the average value of the principal gradient of functional connectivity[17] within each network's boundaries. We related all network-level age effects to this measure of functional hierarchy.

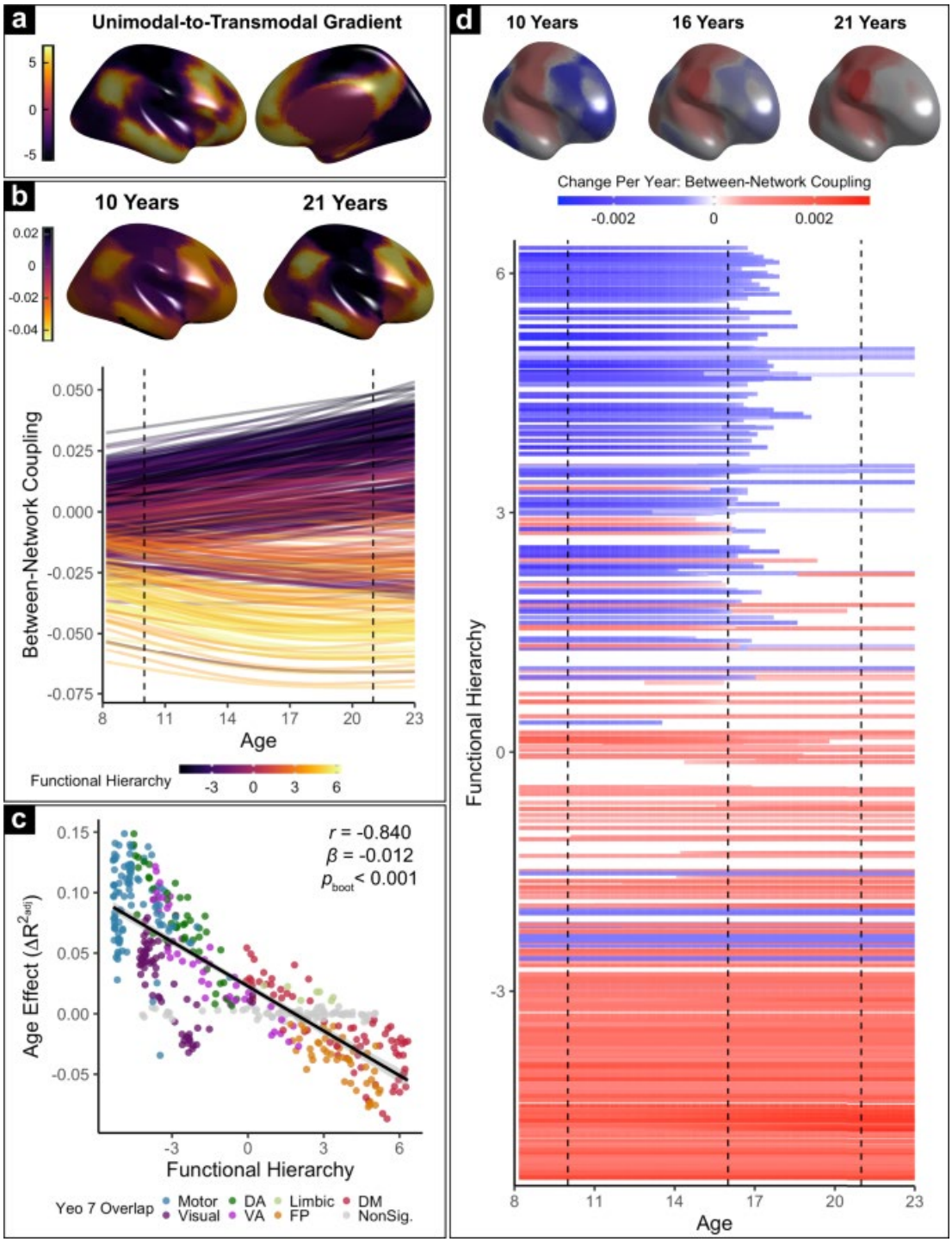


**Figure 3.3. Network development in youth unfolds along a functional hierarchy.**

**a** We define functional hierarchy according to the widely used principal gradient of functional connectivity from Margulies et al. (2016), which describes each location on the cortex on a

unimodal-to-transmodal continuum. **b** Between-network coupling is modeled for every network at each scale using Generalized Additive Models (GAMs) with penalized splines to account for linear and nonlinear effects of age. Each solid line represents the developmental pattern of one network at one scale; colors indicate the position of that network on the functional hierarchy. Dashed lines and corresponding brain maps represent estimated between-network coupling at each age, averaged across scales. Between-network coupling of sensorimotor networks (purple lines) increases with age, indicating increased integration. In contrast, the coupling of association networks (yellow lines) declines with age, reflecting increased segregation. **c** Age effects of each network (from **b**) are plotted versus their position on the functional hierarchy (from **a**). Networks that do not display significant change over development are shaded in gray ($Q_{FDR} > 0.05$). The position of each network on the functional hierarchy explains the majority of variance in age effects ($r = -0.840$, $\beta = -0.012$, $p_{boot} < 0.001$, two-sided). **d** We quantified the duration, magnitude, and direction of maturational changes in coupling for each network using the derivatives of the fitted splines (from **b**). Top: annualized change in between-network coupling at 10, 16, and 21 years old, averaged across scales. Bottom: change per year in average between-network coupling of each network across the age range studied; as in **b**, each line represents the developmental pattern of a given network at a single scale. While integration of sensorimotor networks increases over the entire age range sampled, segregation of association networks generally plateaus near the end of adolescence.

Across all participants and independent of age, we found greater average between-network coupling was present lower in the functional hierarchy, whereas attenuated coupling was present higher in the hierarchy (Fig. 3.3b). To rigorously model linear and nonlinear changes in coupling over development, we used generalized additive models (GAMs) with penalized splines to examine how between-network coupling of each network was associated with age. In these models, sex and in-scanner motion were also included as covariates. We found that age-related changes in between-network coupling were largely explained by a network's position in the

functional hierarchy. Between-network coupling of lower-order networks became more positive at older ages, indicative of greater network integration. In contrast, between-network coupling in higher-order networks became more negative, reflecting increasing segregation. A network's position on the functional hierarchy explained most of the variance in observed developmental effects (Fig. 3.3c; $r = -0.84$, $p_{boot} < 0.001$). Sensitivity analyses yielded similar results using data from resting-state scans alone ($r = -0.77$, $p_{boot} < 0.001$) or from task scans alone ($r = -0.83$, $p_{boot} < 0.001$). Together, these results suggest that the development of between-network coupling in youth is largely described by dissociable processes of segregation and integration across the functional hierarchy.

Next, we sought to identify intervals of significant age-related change in-network coupling. To accomplish this, we calculated the confidence interval of the derivative of the developmental curve for each model. We found that age-related changes in sensorimotor and association networks occurred over different developmental periods: between-network coupling increased in lower-order areas over the entire age range studied, whereas decreases in between-network coupling in higher-order areas did not extend beyond late adolescence (Fig. 3.3d). Consequently, in addition to differences in the sign of developmental changes described above, the temporal span of maturation in-network coupling also systematically varied across the cortico-functional hierarchy.

To provide a more nuanced understanding of the maturational changes in between-network coupling described above, we next evaluated the development of specific connections between networks. As between-network connections can link networks that have a similar hierarchical position (i.e., two association networks) or may alternatively link a sensorimotor and association network, we calculated the difference in hierarchical position of the two networks connected by each edge. As the principal axis captures variance in the cortical coupling, we expected networks similarly positioned along this axis to share a degree of this variance. As expected, we found that

networks with similar hierarchical positions had greater mean coupling, and networks that were further apart in the functional hierarchy tended to have weaker coupling across participants ($r = -0.57$, $p_{boot} < 0.001$; Fig. 3.4a). Critically, we additionally found that age-related changes in-network edges were also explained by differences in their relative position in the functional hierarchy ($r = -0.49$, $p_{boot} < 0.001$; Fig. 4b). Specifically, sensorimotor-to-sensorimotor edges tended to strengthen with age, whereas edges that linked sensorimotor and association networks weakened (Fig. 4c; $p_{boot} < 0.001$); developmental strengthening of association-to-association edges was present but less prominent. Sensitivity analyses provided convergent results using data from resting-state scans only (Fig. S7c; $r = -0.39$, $p_{boot} = 0.005$) and from task scans only (Fig. S8c; $r = -0.45$, $p_{boot} < 0.001$). These results demonstrate that functional network development is characterized by increases in coupling between hierarchically similar networks and decreases in coupling between dissimilar networks—yielding increased differentiation along the functional hierarchy with development.

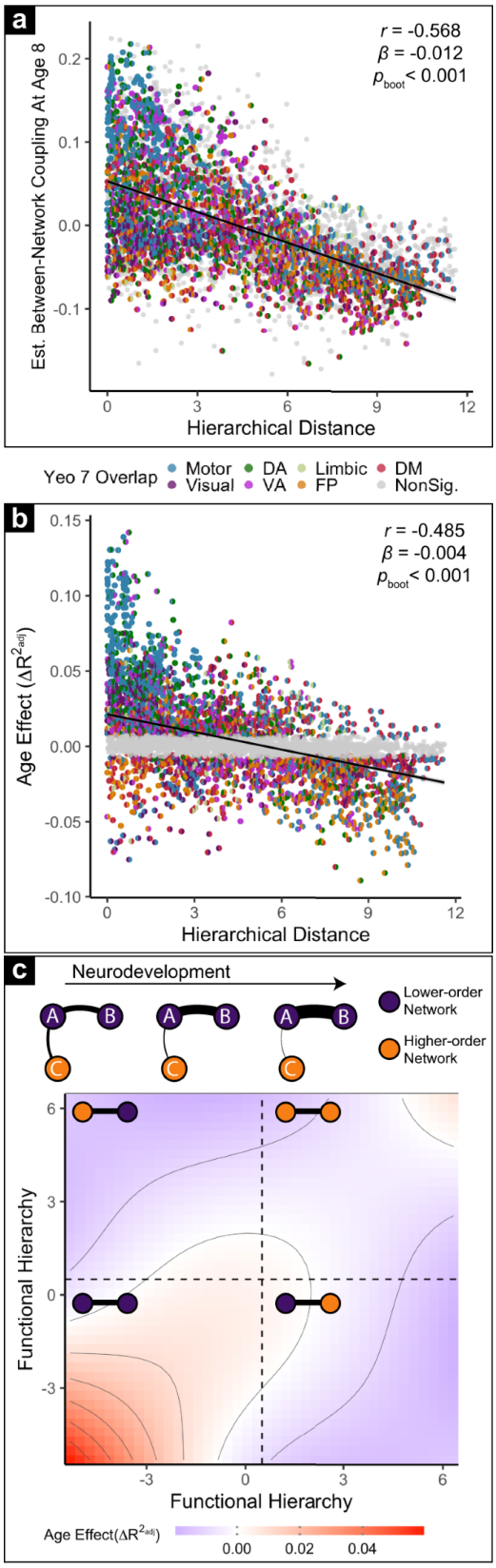


**Fig. 3.4:**

**Figure 3.4 Maturation of between-network coupling aligns with the position of each network in the functional hierarchy.**

**a** Mean between-network coupling is largely captured by relative position along the sensorimotor to association axis. The inter-network coupling of each pair of networks at each scale is modeled using a GAM to estimate their values at age 8. Here, those values are plotted versus the difference in the hierarchical position of the two networks being evaluated. Each data point represents the coupling of a network pair at a given scale. Each half of the circle is colored according to constituent networks' maximum overlap with the 7-network solution defined by Yeo et al. (2011); network pairs that do not significantly change with age after FDR correction ($Q < 0.05$) are shaded in gray. As expected, networks at a similar position along the functional hierarchy tend to have higher coupling ($r = -0.568$, $\beta = -0.012$, $p_{boot} < 0.001$, two-sided). **b** Age effects quantifying the development of between-network coupling is similarly aligned with the relative position of networks along the functional hierarchy. Age effects of every network pair at each scale are plotted versus their hierarchical distance and colored as in **a**. Network pairs without significant age effects are plotted in gray. Developmental effects on pairwise coupling between networks are associated with the hierarchical distance between networks ($r = -0.49$, $p_{boot} < 0.001$, two-sided). **c** Top: schematic summarizing developmental effects. Development is associated with strengthening of network coupling between lower-order networks and weakening of coupling between lower and higher-order networks; thicker lines represent greater functional coupling. Bottom: topographical plot of the observed age effect as a function of absolute (rather than relative) network hierarchy values across all network pairs. Increased coupling with age between functionally similar networks is prominent for sensorimotor networks (bottom left), and less prominent for association networks (top right). Age-related decreases in coupling occur in sensorimotor-association network pairs (top left and bottom right).

It should be noted that previous studies have documented that the physical distance between two brain regions explains the patterning of functional maturation across network edges[49,50,51]. As

functional hierarchy is related to the intrinsic geometry of the cortex[52,53], we sought to verify that the effects of hierarchical distance described above were not better explained by physical distance. To do so, we compared the correlation between age effects and Euclidean distance with the relationship between age effects and hierarchical distance. While the correlation between Euclidean distance and age effects was significant ($r = -0.11$, $p_{boot} < 0.001$), it was substantially weaker than that observed for hierarchical distance ($r = -0.49$, $p_{boot} < 0.001$) and the effect of hierarchical distance remained significant while co-varying for Euclidean distance (partial $r = -0.45$, $p < 0.001$). This result suggests that although the physical distance spanned by a functional connection is weakly related to its developmental pattern, developmental effects are better explained by the functional distance that a connection spans across the sensorimotor-to-association hierarchy.

### 2.2 Development has dissociable signatures at different networks and scales

The above results demonstrate that functional network development is largely captured by a network's position on a hierarchical axis of sensorimotor-to-associative function. However, these analyses are agnostic to the multi-scale nature of the personalized brain networks that we constructed. As a next step, we evaluated whether developmental effects were dependent on network scale. Initial inspection revealed that the relationship between age and between-network coupling varied systematically as a function of scale, with greater age effects in the sensorimotor cortex at finer network scales (Fig. 3.5a). To quantify scale effects while controlling for within-subject correlations over scales, we used generalized estimating equations (GEEs) with exchangeable correlation structures at each cortical vertex. We found that the effect of scale on between-network coupling was strongest in the sensorimotor cortex (Fig. 3.5b). Furthermore, we found evidence that scale-moderated age effects, with maximal scale-by-age interactions being observed in the sensorimotor cortex (Fig. 3.5c).

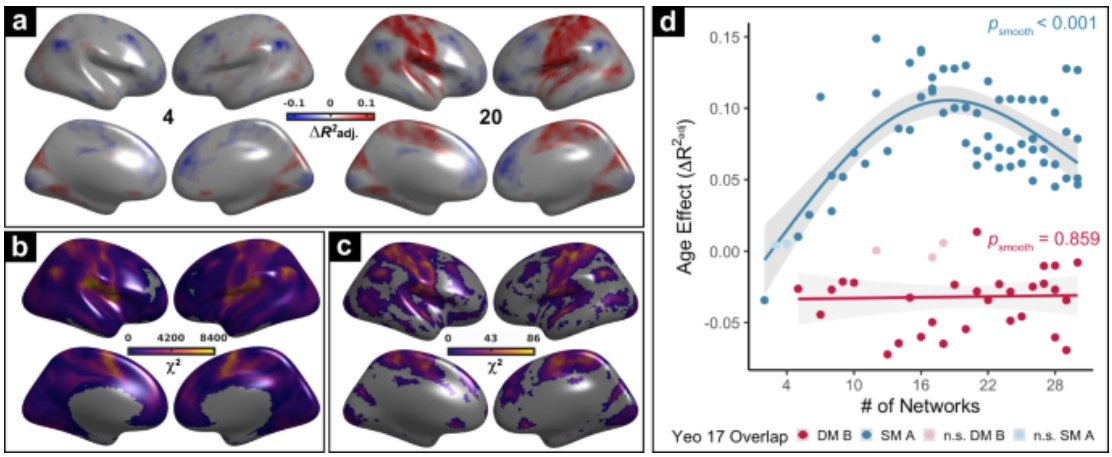


**Figure 3.5 The interactions between-network scale and developmental coupling is maximal in sensorimotor cortex.**

**a** The effect of age on average vertex-wise between-network coupling at two scales (4 and 20). Age effects are modeled using GAMs with penalized splines; thresholded at $Q_{FDR} < 0.05$. Scale-dependent age effects can be observed in sensorimotor cortex: while no developmental increase in between-network coupling was seen in somatomotor cortex at scale 4, such an increase is evident at scale 20. **b** Across ages, between-network coupling of the sensorimotor cortex is strongly influenced by scale. Generalized estimating equations (GEEs) reveal that the effect of scale ($\chi^2$) differentially influences the strength of between-network coupling across the cortex. Locations within unimodal sensorimotor cortex exhibit the strongest scale-dependence in their mean between-network coupling ($Q_{FDR} < 0.05$). **c** Scale differentially interacts with age-dependent developmental associations with coupling across the cortex. GEEs are used to examine the degree of scale-moderated developmental effects (age-by-scale interaction; thresholded at $Q < 0.05$); maximal effects are present in the sensorimotor cortex. **d** Scale differentially interacts with age-dependent developmental effects in sensorimotor and association networks. Specifically, age effects in lower-order networks tend to be more scale-dependent than those in higher-order networks. The effect of age across scales is plotted for networks predominantly overlapping with the lowest-order (blue; Somatomotor-A) and highest-order (red; Default Mode-B)

networks, as quantified from the functional hierarchy. Statistical tests are two-sided. Error bands depict the 95% confidence interval.

To further understand these scale-dependent age effects, we compared the age effect across scales for networks that fall at opposite ends of the sensorimotor-to-association hierarchy. Specifically, at each scale we identified networks that aligned most closely with the somatomotor-A network and the default mode-B network from the commonly used atlas defined by Yeo et al. (Fig. 3.5d). This comparison revealed that age effects within the somatomotor network were highly scale-dependent, with greater increases in between-network coupling with age at finer scales. In contrast, default-mode networks demonstrated consistent developmental segregation across scales. These results suggest that age-related changes in-network coupling are differentially linked to scale across the cortical hierarchy.

### 2.3 Multi-scale network coupling is associated with executive function

Having delineated developmental changes in between-network coupling, we next sought to understand the implications for individual differences in executive function (EF). First, we modeled the association between-network coupling and EF, controlling for developmental effects by including age as a penalized spline; other model covariates included sex and motion as in prior analyses. We found that the relationship between EF and between-network coupling was quadratically related to the functional hierarchy (Fig. 3.6a; $p_{boot} = 0.003$); this quadratic pattern was markedly different than the linear relationship between hierarchy and age effects (see Fig. 3.3c for comparison). Specifically, decreased between-network coupling at both extremes of the hierarchy was associated with greater EF, with maximal effects being seen in sensorimotor and default-mode networks. In contrast, greater coupling of several visual, ventral attention, and fronto-parietal networks were associated with greater EF.

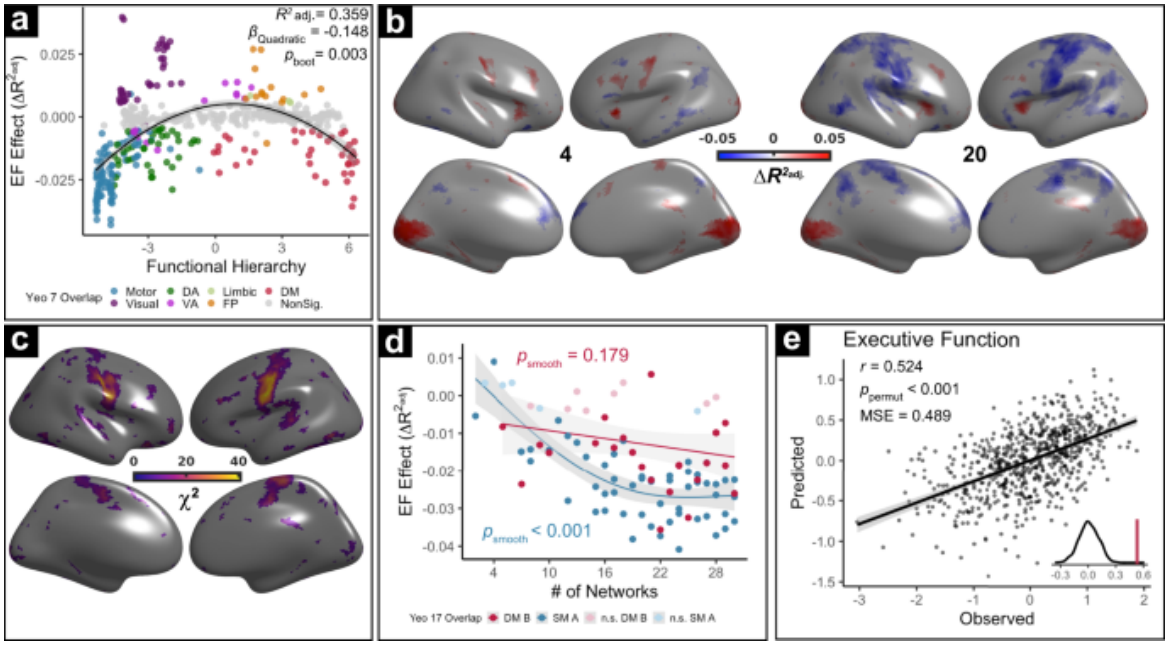


**Figure 3.6** . **Multi-scale network coupling is associated with executive function.**

**a** Network-level relationships between coupling and EF are quadratically related to transmodality. Specifically, segregation of both sensorimotor and default-mode networks is associated with better EF. These associations with EF are dissociable from normative developmental effects (Fig. 3.3c) where default-mode segregation and sensorimotor integration are observed. The statistical test was two-sided. **b** Analyses at scales 4 and 20 reveal differing associations with EF. While between-network coupling of visual, insular, and dorsolateral prefrontal cortical areas is consistently associated with greater EF ($Q_{FDR} < 0.05$), opposite associations with EF were present in motor cortex at coarse and fine scales. **c** Tests of age-by-scale interactions using GEEs reveal that scale effects are strongest in the sensorimotor cortex. **d** Scale is differentially linked to EF associations with coupling in higher-order and lower-order networks. As for age, effects in somatomotor networks tend to be more scale-dependent than those in association networks. The

effect of age across scales is plotted for networks predominantly overlapping with the lowest-order (blue; Somatomotor-A) and highest-order (red; Default Mode-B) of the Yeo 17 networks. **e** Complex patterns of multi-scale coupling between personalized networks accurately predicts EF in unseen data. Cross-validated ridge regression with nested parameter tuning was used to predict EF of unseen data using each participant's multivariate pattern of coupling across scales. Error bands depict the 95% confidence interval, statistical tests are two-sided for **d** and one-sided for **e**. MSE = mean squared error.

To further understand these effects, we next performed high-resolution analyses at each cortical vertex to detail associations between EF and between-network coupling across scales. Consistent with network-level results, reduced between-network coupling in default-mode regions like the medial prefrontal cortex and precuneus was associated with greater EF across scales (Fig. 3.6b). In contrast, greater between-network coupling in the dorsolateral prefrontal cortex, anterior insula, and calcarine fissure was associated with greater EF across scales. Sensorimotor cortices again exhibited scale-dependent associations: higher between-network coupling in the sensorimotor cortex was associated with reduced EF, but only at finer scales. To further assess the role of network scale, we used GEEs to examine whether there was an interaction between EF and scale on between-network coupling at each cortical location. This analysis revealed prominent scale effects, primarily in sensorimotor cortices (Fig. 3.6c). To further illustrate the differential effects of network scale, we again contrasted networks that lie at opposite ends of the functional hierarchy (Fig. 3.6d). We found that network scale did not moderate the association between default-mode network coupling and EF; greater default-mode segregation was associated with better EF across scales. However, somatomotor network associations with EF were highly dependent on network scale.

Having found evidence of both scale-dependent and scale-independent associations between EF and network coupling, we next examined the degree to which these complex patterns of coupling could jointly predict individual differences in EF. To do so, we fit a multivariate ridge regression model to predict EF using data from all scales, while controlling for age and in-scanner motion. We found that this multivariate model accurately predicted the EF of unseen participants (see Methods; Fig. 3.6e; $r = 0.52$, $p_{permut} < 0.001$). Similar results were obtained in sensitivity analyses that considered data only from resting-state or task fMRI runs ($r_{rest} = 0.34$, $p_{permut} < 0.001$; $r_{task} = 0.54$, $p_{permut} < 0.001$). These results emphasize that EF is supported by multi-scale patterns of functional coupling.

Finally, to assess the specificity of the relationship between functional network coupling and EF, we also evaluated associations with other major domains of cognition, including episodic memory and social cognition. For episodic memory, segregation of the most unimodal networks was similarly associated with episodic memory. However, transmodal segregation was not associated with episodic memory performance, and no quadratic relationship with functional hierarchy was observed ($p_{boot} = 0.269$). A similar assessment of the social cognition factor revealed no significant associations with network-level coupling after correction for multiple comparisons. Edge-level ridge regression analyses revealed reduced model performance for both episodic memory ($r = 0.33$, $p_{permut} < 0.001$) and social cognition ($r = 0.14$, $p_{permut} = 0.024$). Taken together, these results suggest some degree of specificity for links between multi-scale network connectivity and EF.

## 3. Discussion

In this study, we demonstrated that variation in the development of person-specific functional networks is intrinsically related to fundamental properties of brain organization. Specifically, we found that developmental patterns differentially unfold along the hierarchical sensorimotor to association axis of organization: unimodal sensorimotor networks became more integrated with

age, while transmodal association networks became more segregated. This dissociable pattern of maturation had unique relevance for the development of cognition: while greater segregation of association networks was associated with better EF, developmental integration of sensorimotor networks was associated with worse EF. By examining functional network development and associations with EF across a range of macroscale networks, we additionally identified scale-dependent effects, which were predominantly present in somatomotor networks. Taken together, these results provide a new framework that incorporates multi-scale cortical organization for understanding how functional network maturation allows for the development of cognition in youth.

### 3.1 Functional network development differs by position in a unimodal to transmodal hierarchy

Previous work in adults[36,37,38,39] has established that between-individual variability of functional topography is greatest in the association cortex. In our prior report[40] we demonstrated that this is also true in youth. Such marked variability of functional topography in association cortices may be a result of protracted and environmentally sensitive development in these higher-order cortices, facilitating continuous adaptation to individual-specific needs[5,54]. Here, we extended prior findings by demonstrating that topographic variability aligns with a functional hierarchy across multiple network scales. Furthermore, we found that variability of functional topography increasingly localizes to association cortices as the number of functional networks increases. As this scale-dependency might be just one of many shifts in between-participant variability over scales[32,43], our results highlight the importance of scale and precision functional mapping techniques for investigations of individual differences in functional network coupling.

We found strong evidence that developmental changes in between-network coupling align with a sensorimotor-to-association hierarchy. Even prior to adolescence, sensorimotor networks tended to have greater between-network coupling, which was primarily driven by their coupling with other lower-order networks. In contrast, association networks were more functionally segregated even among the youngest of our participants. From ages 8–23 years, this pattern became more prominent: between-network coupling further strengthened in lower-order networks and weakened with age in higher-order networks. Together, these developmental effects served to further distinguish the functional hierarchy that is now well described in adults and broadly aligns with recent reports using independent methods and datasets[9,10]. This functional differentiation of cortical hierarchy over development is consistent with evidence that cortical myeloarchitecture further differentiates between sensorimotor and association regions during adolescence[55], and that higher-order structural networks become increasingly dissimilar from lower-order networks with age[56]. Coupling between hierarchically similar networks may be partially attributable to the propagation of infra-slow cortical waves along functional hierarchies[25,57,58,59]; however, additional research is needed to examine how such waves evolve in development. Taken together, our results suggest that functional network development in youth both aligns with and strengthens the sensorimotor-to-association hierarchy seen in adulthood.

### 3.2 Functional network differentiation supports executive function

EF is supported by coordinated recruitment of distributed networks of brain regions[60,61,62]. We found that the segregation of networks located at the two opposing ends of the sensorimotor to association hierarchy (i.e., somatomotor and default-mode networks) was associated with cognitive performance. Conversely, we demonstrated that increased integration of networks more centrally positioned within the axis supported EF. As such, two dissociable patterns of normative network development observed across the cortical functional hierarchy differentially relate to the development of EF. Specifically, whereas normative developmental segregation of transmodal association networks was positively associated with EF, unimodal integration was positively

associated with age but negatively associated with EF. These results in part explain the existing heterogeneous literature, which has reported that refinement of both functional network segregation and integration is important for neurocognitive development[19,63,64,65]. However, our results also specify that the degree to which developmental integration versus segregation is advantageous for EF may largely depend on a network's role within the functional hierarchy.

That both sensorimotor and DMN segregation were associated with greater EF accords with recent work demonstrating that the overall balance of network activity shifts across the functional hierarchy when individuals are engaged in externally oriented versus internally guided cognition. Prior work has shown that localized activity within networks at the bottom of the hierarchy supports cognition when it is reliant on immediate perceptual input[66]. In contrast, greater segregation of unimodal networks from transmodal networks supports cognition that is dependent on internally-oriented processing, including memory or theory of mind[18,66,67]. Furthermore, the association between EF and integration of control networks situated more centrally in the hierarchy is supported by prior literature emphasizing the role of these networks in top-down control[68,69,70]. Speculatively, these results suggest that functional segregation at the extremes of the functional hierarchy, in tandem with the integration of control networks situated in the middle of the hierarchy, may serve to reduce cross-modal interference[71,72] while facilitating coordination of brain networks specialized for top-down cognitive control[67,68,69].

We found that transmodal cortical segregation increased with age in youth and is associated with enhanced EF. In contrast, unimodal cortical integration increased with age but was associated with poorer EF. This discrepancy could stem from differences in the pace of maturation between parts of the cortex. In late life, cortical networks reintegrate, losing the segregation that is achieved earlier in maturation[73,74,75,76,77,78,79]. Notably, this integration at the end of the lifespan has been shown to mediate cognitive decline in both normal aging and neurodegenerative disease[76,77,78,79]. Our data suggest that the inflection point between

maturational segregation and integration may be temporally staggered across a normative hierarchy, with lower-order networks beginning reintegration prior to transmodal networks, which are still segregating in youth. Consequently, we hypothesize that processes seen in aging may have begun in lower-order sensorimotor networks in adolescence.

### 3.3 Multi-scale patterns of network development are associated with executive function

Prior work has primarily investigated organizational regimes of 2[80], 3[17], 4[81], 5[82], 6[83], 7[84], 13[50], and 17[84] functional subdivisions of the brain. In line with an emergent body of literature regarding multi-scale brain organization[26,32,85,86], the scale-dependencies that we observed suggest that previous, single-scale descriptions of neurodevelopment only partially describe cortical network reorganization in youth. Notably, we present new evidence that scale and hierarchical positioning interact. We observed differential effects of scale on both development and EF across the functional hierarchy, with scale effects being disproportionately present in unimodal cortices. Coarse segregation of unimodal networks from transmodal networks with age was concurrent with fine-grained integration within unimodal networks. In contrast, no such scale dependence was seen in transmodal networks. A similar scale-dependence was present in associations with EF: coarse segregation and fine-grained integration of motor areas were both associated with worse EF. These effects of network scale might be driven in part by a greater propensity for unimodal functional networks to host nested multi-scale organizations than their transmodal counterparts[87,88].

Finer scales systematically capture shorter “neural bridges”[6] across the functional hierarchy. In other words, as higher network resolutions distinguish increasingly similar subnetworks, finer scales ultimately capture functional interactions between networks that are more proximate in the functional hierarchy. In our data, at the coarsest scale of two functional subdivisions, between-network coupling reflects interactions between only a single sensorimotor and association network. At this resolution, network segregation between these two broad classes of cortex

increased with age. In contrast, finer scales revealed that, along with overall developmental segregation of sensorimotor and association networks, there is prominent integration of functionally similar, finer-grained networks. Consequently, our findings illustrate that different network scales reveal different developmental effects across the functional hierarchy. Several limitations to the current study should be noted. Adolescent development represents a complex, layered process not easily delineated by cross-sectional studies. This is a particularly salient limitation for approaches seeking to establish the role of brain maturation in cognitive development, rather than their co-occurrence. Further, there are undoubtedly individual differences in the pace of brain development, which cannot be indexed with cross-sectional data[89]. Future longitudinal studies will be critical for understanding temporal precedence in network maturation and how deviations from normative neurodevelopment are associated with the emergence of psychopathology[90]. Second, as children tend to move more during MRI scans, in-scanner head motion continues to be a concern for all neuroimaging studies of development[91]. Here, we rigorously followed the best practices for mitigating the influence of head motion on our results, including the use of a top-performing preprocessing pipeline and co-varying for motion in all hypothesis testing[92]. The use of these conservative procedures limits the possibility that reported findings are attributable to in-scanner motion. Third, we used data combined across three fMRI runs, including two where an fMRI task was regressed from the data[93]. This choice was motivated by studies that have shown that functional networks are primarily defined by individual-specific rather than task-specific factors and that intrinsic networks during task performance are similarly organized to those at rest[94]. Importantly, by including task-regressed data, we were able to generate individualized networks with 27 min of high-quality data. Prior work suggests that parcellations created using a timeseries of this length show high concordance with those generated using 380 min of data[95]. Fourth, we studied multi-scale organization in the spatial domain; the brain also exhibits multi-scale organization in the temporal domain[96,97,98,99]. Future investigations using tools with greater temporal resolution may be critical for simultaneously describing the spatial and temporal multi-scale organization. Finally, the

maturation of subcortical structures is a critical component of neurodevelopment[100,101]. Recent advances in precision[102,103] and multi-scale[104] functional mapping of subcortical regions and hierarchies[105] present an excellent opportunity for future work to delineate the role of subcortical functional coupling in neurocognitive development.

In conclusion, we leveraged advances in delineating personalized functional networks to elucidate divergent patterns of functional network development and to establish their relevance for cognition. These results are important for understanding the developmental refinement of cortical hierarchy that is prominent in healthy adults. Moving forward, the process of this refinement may be critically important for understanding executive dysfunction in those affected by mental illness. Examining abnormalities of functional network reorganization in longitudinal clinical samples will provide an important opportunity to test the hypothesis that insufficient maturational segregation of association networks confers risk to diverse psychiatric disorders. Indeed, existing research suggests that abnormalities associated with cross-disorder psychopathology are predominantly present at the association end of the functional hierarchy[15,106,107], and that diverse psychopathology is associated with attenuated segregation of higher-order networks[108]. Eventually, understanding the normative development of individualized networks may be a critical prerequisite for guiding personalized neuromodulatory interventions targeting both individual-specific functional neuroanatomy and developmental phases with amenable plasticity.

## 4.0 Methods

### 4.1 Participants

A total of 1601 participants were studied and compensated as part of the Philadelphia Neurodevelopmental Cohort[45]. We excluded 340 participants due to treatment with psychoactive medications, prior inpatient psychiatric treatment, or incidentally encountered structural brain abnormalities. Among the 1261 participants eligible for inclusion, 54 more were excluded from

analyses due to low-quality T1-weighted images or low-quality FreeSurfer reconstructions. Of the 1207 subjects with useable T1 images and adequate FreeSurfer reconstructions, 514 more participants were excluded for missing functional data or poor functional image quality. For inclusion in analyses, all participants were required to have three functional runs that passed quality assurance. As prior[91,92], a functional run was excluded if the mean relative root-mean square (RMS) framewise displacement was higher than 0.2 mm, or it had more than 20 frames with motion exceeding 0.25 mm. This set of exclusion criteria resulted in a final sample of 693 participants with a mean age of 15.93 years (*SD* = 2.33); the sample included 301 males and 392 females. All subjects or their parents/guardian provided informed consent, and minors provided assent. All study procedures were approved by the Institutional Review Boards of both the University of Pennsylvania and the Children's Hospital of Philadelphia.

### 4.2 Image acquisition

As previously described[45], all MRI scans were acquired using the same 3 T Siemens Trim Trio whole-body scanner and 32-channel head coil and VB17 revision software at the Hospital of the University of Pennsylvania.

#### 4.2.1 Structural MRI

Prior to functional MRI acquisitions, a 5 min magnetization-prepared, rapid acquisition gradient-echo T1-weighted (MPRAGE) image (TR = 1810 ms; TE = 3.51 ms; TI = 1100 ms, FOV = 180 × 240 $mm^2$, matrix = 192 × 256, effective voxel resolution = 0.9 × 0.9 × 1 $mm^3$) was acquired.

#### 4.2.2 Functional MRI

We used one resting-state and two task-based (*n*-back and emotion identification) fMRI scans for the current study. All fMRI scans were acquired with the same single-shot, interleaved multi-slice,

gradient-echo, echo-planar imaging (GE-EPI) sequence sensitive to BOLD contrast with the following parameters: TR = 3000 ms; TE = 32 ms; flip angle = 90°; FOV = 192 × 192 $mm^2$, matrix = 64 × 64; 46 slices; slice thickness/gap = 3/0 mm, effective voxel resolution = 3.0 × 3.0 × 3.0 $mm^3$. Resting-state scans consisted of 124 volumes, while the *n*-back and emotion recognition scans consisted of 231 and 210 volumes, respectively. Further details regarding the *n*-back[60] and emotion recognition[109] tasks have been described in prior publications.

#### 4.2.3 Field map

A B0 field map was derived for application of distortion correction procedures, using a double-echo, gradient-recalled echo (GRE) sequence: TR = 1000 ms; TE1 = 2.69 ms; TE2 = 5.27 ms; 44 slices; slice thickness/gap = 4/0 mm; FOV = 240 mm; effective voxel resolution = 3.8 × 3.8 × 4 mm.

#### 4.2.4 Scanning procedure

Before scanning, to acclimate subjects to the MRI environment, a mock scanning session where subjects practiced the task was conducted using a decommissioned MRI scanner and head coil. Mock scanning was accompanied by acoustic recordings of the noise produced by gradients coils for each scanning pulse sequence. During these sessions, feedback regarding head movement was provided using the MoTrack motion tracking system (Psychology Software Tools). Motion feedback was given only during the mock scanning session. To further minimize motion, before data acquisition, participants' heads were stabilized in the head coil using a single foam pad over each ear and a third over the top of the head.

## 4.3 Image processing

### 4.3.1 Preprocessing

Structural images were processed with FreeSurfer (version 5.3) to allow for the projection of functional timeseries to the cortical surface[110]. Functional images were processed using a top-performing preprocessing pipeline implemented using the eXtensible Connectivity Pipeline (XCP) Engine[111], which includes tools from FSL[112,113] and AFNI[114]. This pipeline included (1) correction for distortions induced by magnetic field inhomogeneity using FSL's FUGUE utility, (2) removal of the initial volumes of each acquisition, (3) realignment of all volumes to a selected reference volume using FSL's MCFLIRT, (4) interpolation of intensity outliers in each voxel's timeseries using AFNI's 3dDespike utility, (5) demeaning and removal of any linear or quadratic trends, and (6) co-registration of functional data to the high-resolution structural image using boundary-based registration[115]. Images were de-noised using a 36-parameter confound regression model that has been shown to minimize associations with motion artifacts while retaining signals of interest in distinct subnetworks[92]. This model included the six framewise estimates of motion, the mean signal extracted from eroded white matter and cerebrospinal fluid compartments, the mean signal extracted from the entire brain, the derivatives of each of these nine parameters, and quadratic terms of each of the nine parameters and their derivatives. Both the BOLD-weighted timeseries and the artifactual model timeseries were temporally filtered using a first-order Butterworth filter with a passband between 0.01 and 0.08 Hz to avoid mismatch in the temporal domain[116]. Furthermore, to derive timeseries that were more comparable across runs, the task activation model was regressed from *n*-back and emotion identification fMRI data[93]. The task activation model and nuisance matrix were regressed out using AFNI's 3dTproject.

For each modality, the fMRI timeseries of each participant was projected to their own FreeSurfer surface reconstruction and smoothed on the surface of this reconstruction with a 6 mm full-width half-maximum kernel. The smoothed data were projected to the *fsaverage5* template, which has 10,242 vertices on each hemisphere (18,715 total vertices after removing the medial wall).

Finally, we concatenated the three fMRI acquisitions, yielding a timeseries of 27 min and 45 s in total (555 volumes). As prior, we removed vertices with a low signal-to-noise ratio[117,118,119]. We used the same SNR mask as in our prior work, which used the same dataset[40]. After masking, 17,734 vertices remained for subsequent analyses.

#### 4.3.2 Regularized non-negative matrix factorization

As previously described in detail[40,47], we used non-negative matrix factorization[46,47] (NMF) to derive personalized functional networks. The NMF method decomposes the timeseries by positively weighting cortical vertices that covary, leading to a highly specific and reproducible parts-based representation[46,120]. Our approach was enhanced by a group-consensus regularization term that preserves inter-individual correspondence, as well as a data locality regularization term to mitigate imaging noise, improve spatial smoothness, and enhance functional coherence of personalized functional networks (see Li et al., 2017 for details of the method; see also: https://github.com/hmlicas/Collaborative_Brain_Decomposition). As NMF requires non-negative input, we shifted the timeseries of each vertex linearly to ensure all values were positive. Finally, all vertex timeseries were normalized to their maximum values such that all values ranged between 0 and 1.

Given a group of $n$ subjects, each having fMRI data $X^i \in R^{S \times T}$, $i = 1, \ldots, n$, consisting of $S$ vertices and $T$ timepoints, we aimed to find $K$ non-negative functional networks $V^i = (V^i_{s,k}) \in R^{S \times K}$ and their corresponding time courses $U^i = (U^i_{t,k}) \in R^{T \times K}$ for each subject, such that

$$Xi \approx Ui(Vi)' + Ei, s.t. Ui, Vi \geq 0, \forall 1 \leq i \leq n, Xi \approx Ui(Vi)' + Ei, s.t. Ui, Vi \geq 0, \forall 1 \leq i \leq n, \quad (1)$$

Where $(V^i)'$ is the transpose of $(V^i)$ and $E^i$ is independently and identically distributed residual noise following a gaussian distribution. Both $U^i$ and $V^i$ were constrained to be non-negative so

that each functional network did not contain anticorrelated functional units. A group-consensus regularization term was applied to ensure inter-individual correspondence, which was implemented as a group-sparsity term on each column of $V^i$ and formulated as

$$Rc=\sum k=1KV1,...,n\cdot,k2,1=\sum k=1K\sum Ss=1(\sum ni=1(Vis,k)2)1/2(\sum Ss=1\sum ni=1(Vis,k)2)1/2Rc=\sum k=1K\text{⍰}V\cdot,k1,...,n2,1=\sum k=1K\text{⍰}\sum s=1S(\sum i=1n(Vs,ki)2)1/2(\sum s=1S\sum i=1n(Vs,ki)2)1/2 \quad (2)$$

The data locality regularization term was applied to encourage spatial smoothness and coherence of the functional networks using graph regularization techniques[121]. The data locality regularization term was formulated as

$$RiM=Tr((Vi)'LiMVi),RMi=Tr((Vi)'LMiVi), \quad (3)$$

where $LiM=DiM-WiMLMi=DMi-WMi$ is a Laplacian matrix for subject *i*, WiMWMi is a pairwise affinity matrix to measure spatial closeness or functional similarity between different vertices, and DiMDMi is its corresponding degree matrix. The affinity between each pair of spatially connected vertices (here, vertices *a* and *b*) was calculated as $(1+corr(Xia,Xib))/2(1+corr(Xai,Xbi))/2$, where *corr*(Xia,Xib)(Xai,Xbi) is the Pearson correlation coefficient between timeseries XiaXai and XibXbi; the pairwise affinity between non-connected vertices was set to zero so that WiMWMi would be sparse. We identified personalized functional networks by optimizing a joint model with integrated data fitting and regularization terms formulated as

$$\min(Ui,Vi)\sum i=1n(Xi-Ui(Vi))2F+\lambda M\sum i=1nRim+\lambda cRc,s.t.Ui,Vi\geq 0,Vi.,k\infty=1,\forall 1\leq k\leq K,\forall 1\leq i\leq n\min(Ui,Vi)\sum i=1n\text{⍰}(Xi-Ui(Vi))F2+\lambda M\sum i=1n\text{⍰}Rmi+\lambda cRc,s.t.Ui,Vi\geq 0,V.,k\infty i=1,\forall 1\leq k\leq K,\forall 1\leq i\leq n \quad (4)$$

Where λM=β×(T/K×nm)λM=β×(T/K×nm) and λc=α·(n·T/K)λc=α·(n·T/K) are used to balance the data fitting, data locality, and group-consensus regularization terms, $n_m$ is the number of neighboring vertices, and $\alpha$ and $\beta$ are free parameters leveraged to scale sparsity and locality in derived network solutions, respectively. For this study, we used previously validated parameters[40,47] (Sparsity, locality = 1,10) across 29 values of $K$ ($K$ = 2 to $K$ = 30) corresponding to 29 scales of cortical organization. To evaluate the spatial nesting of finer-grained functional networks within coarser networks, we evaluated the degree to which each network from K = 3 to K = 30 overlapped with the coarse network partitions derived at K = 2. Specifically, each vertex from the *fsaverage5* template was assigned to one of the two networks derived at K = 2, corresponding to a single unimodal and transmodal network. At subsequent (finer) scales, we evaluated A) which of the K = 2 networks that it predominantly overlapped within space (e.g., unimodal or transmodal) and B) the percentage of vertices that fell within that K = 2 network.

#### 4.3.3 Defining personalized networks

Our approach to defining personalized networks included three steps. In the first two steps, a group-consensus atlas was created. In the third step, this group atlas was used to initialize network personalization for each participant at each scale. Although individuals exhibit distinct network topography, broad consistencies exist among individual-to-individual[39,94]. By first generating a group atlas for personalization initialization, we ensured spatial correspondence across all subjects and scales. This strategy has also been applied in other studies of personalized networks[121,122]. For computational efficiency and to avoid outlier-driven group atlases, a bootstrap strategy was utilized to perform the group-level decomposition multiple times on a subset of randomly selected participants. Subsequently, the resulting decompositions were fused to obtain one robust initialization. As prior[40,47], we randomly selected 100 subjects and temporally concatenated their timeseries, resulting in a timeseries matrix with 55,500 rows

(timepoints) and 17,734 columns (vertices). We applied the above-mentioned regularized non-negative matrix factorization method with a random initialization to decompose this group-level matrix[46]. A group-level network loading matrix *V* was acquired, which had *K* rows and 17,734 columns. Each row of this matrix represents a functional network, while each column represents the loadings of a given cortical vertex. As prior[40,46], this procedure was repeated 50 times, each time with a different subset of subjects. Accordingly, this process yielded 50 different group atlas estimations for each value of *K*.

Next, we combined the 50 group network atlases to obtain one robust group network atlas with spectral clustering at each value of *K*. Specifically, we concatenated the 50 group parcellations together across networks to obtain a matrix with 50 × *K* rows (functional networks) and 17,734 columns (vertices). Next, we calculated inter-network similarity as

$$Sij=\exp(-d2ij\sigma 2), Sij=\exp(-dij2\sigma 2), \quad (5)$$

where $dij=1-\mathrm{corr}(\mathrm{Networki},\mathrm{Networkj}), dij=1-\mathrm{corr}(\mathrm{Networki},\mathrm{Networkj})$, $\mathrm{corr}(\mathrm{Networki},\mathrm{Networkj})\mathrm{corr}(\mathrm{Networki},\mathrm{Networkj})$ is a Pearson correlation coefficient between $\mathrm{Network}_i$ and $\mathrm{Network}_j$, and $\sigma$ is the median of $d_{ij}$ across all possible pairs of functional networks. Then, we applied normalized-cut-based spectral clustering[123] to group the 50 × *K* functional networks into *K* clusters. For each cluster, the functional network with the highest overall similarity with all other networks in the same cluster was selected as the most representative. The final group network atlas was composed of these maximally representative network estimations at each of the 29 resolutions studied.

In the final step, we derived each individual's specific network atlas using NMF, initializing each participant-specific solution on the group-consensus atlas for any given scale and optimizing NMF in accordance with each individual's specific fMRI timeseries (a 555 × 17,734 matrix). See Li et

al., (2017) for further optimization detail. This procedure yielded loading matrix $V_i$ ($K \times 17{,}734$ matrix) for each participant, where each row is a functional network, each column is a vertex, and the value in each cell quantifies the extent to which each vertex belongs to each network. This probabilistic (soft) definition was converted into discrete (hard) network definitions for the display and calculation of network statistics by labeling each vertex in accordance with its highest loading. This procedure was repeated for all 29 network resolutions.

## 4.4 Quantification and statistical analysis

### 4.4.1 Calculation of variability and spatial alignments of personalized networks

To quantify the degree to which NMF captured individualized functional neuroanatomy regardless of the NMF parameters chosen, we created individualized networks across a range of NMF parameters at both a coarse (K = 4) and fine (K = 20) scale (locality = 5, 10, 20, sparsity = 0.5, 1, and 2). After recalculating individualized networks for the 8 new parameter pairings at both scales, we calculated Adjusted Rand Indices (ARI) to evaluate the correspondence between networks derived from distinct parameterizations and our original individualized functional networks (set at spatial regularization = 10, sparsity = 1). This step yielded a distribution of within-subject ARI, or the similarity in individualized network decompositions across parameterizations. To evaluate the degree to which individual variability in functional network decompositions was driven by individual variability in the functional imaging data rather than the NMF parameters chosen, we compared the distributions of within-subject ARI to between-subject ARI across parameters. Within and between-subject ARI were calculated between our original individualized functional networks and the 16 new conditions for K = 4 and K = 20, locality/sparsity = 5 and 0.5, 5 and 1, 5 and 2, 10 and 0.5, 10 and 2, 20 and 0.5, 20 and 1, 20 and 2.

In order to quantify cross-subject spatial variability in personalized networks, we calculated the median absolute deviation (MAD) of personal network loadings at each vertex across participants. MAD is a non-parametric measure of variance that does not assume a normal

distribution. First, we calculated MAD for each network at each scale. Next, MAD was averaged across *K* networks to obtain a single value of MAD at each vertex for any given scale *K*.

### 4.5 Functional hierarchy

In order to quantify networks in terms of their position within a functional hierarchy, we used a widely adopted principal gradient of functional connectivity[17] (https://github.com/NeuroanatomyAndConnectivity/gradient_analysis). The principal gradient is derived from the primary component of variance in patterns of whole-brain functional connectivity, aligns with hierarchical estimations derived from tract-tracing[7], and reflects a unimodal-to-transmodal continuum of cortical function[17]. As such, at each cortical vertex, the value of this gradient reflects the loading of that vertex onto a cortical hierarchy, with higher principal gradient values corresponding to higher positioning within the hierarchy.

To maximize equivalence with prior studies, we used the original map of the principal gradient provided by Margulies et al. (2016). This map was transformed to *fsaverage5* space using metric-resample from Connectome Workbench. Functional hierarchy values for each network were quantified as the average principal gradient value of each vertex within each network in group-consensus space. These network-wise hierarchy values were used to analyze the spatial distribution of the effects of age and executive function, as described below.

### 4.6 Reference networks

To allow for comparison with previously estimated cortical systems, we quantified the overlap of each group-consensus network with a commonly used 7 and 17-functional network parcellation[84]. To illustrate this overlap, we assigned colors to the group and individualized networks in accordance with their maximum overlap with networks from the 7 and 17-network parcellations.

### 4.7 Spatial permutation testing (spin test)

In order to evaluate the significance of the localization of between-participant variability (MAD) to transmodal cortical areas, we used a spatial permutation procedure called the spin test[48,117,120,124] (https://github.com/spin-test/spin-test). The spin test is a spatial permutation method based on angular permutations of spherical projections at the cortical surface. Critically, the spin test preserves the spatial covariance structure of the data, providing a more conservative and realistic null distribution than randomly shuffling locations. Due to varying spatial covariance structures across scales, we conducted separate spin tests at each scale.

### 4.8 Modeling the association of scale with MAD-principal gradient colocalization

To account for potential non-independence of MAD-principal gradient correlations across scales, significance testing was performed using non-parametric bootstrap resampling. Specifically, we recalculated MAD and the subsequent spatial correlation with the principal gradient at each scale across 1000 bootstrap resamples to generate a bootstrapped confidence interval of the second-order relationship between the network scale and the MAD-principal gradient correlations.

#### 4.8.1 Quantification of between-network coupling

We used functional connectivity (FC) to quantify inter-regional coupling in the processed BOLD signals. Specifically, we calculated between-network FC at three levels of analysis: network, edge, and vertex. At all levels, FC was quantified as the Pearson correlation between BOLD timeseries. At the network level, between-network connectivity was quantified as a network's mean correlation with all other networks. At the edge level, between-network connectivity was quantified as the mean vertex-by-vertex correlation between vertices in both networks. At the vertex level, we evaluated each vertex's average correlation to vertices from all other networks. Between-network coupling at each level was quantified separately at each scale for each participant.

### 4.9 Developmental analyses

#### 4.9.1 Developmental modeling

Developmental effects were estimated using generalized additive models[125,126] (GAMs) with penalized splines in R (Version 3.6.3) using the *mgcv* package[127,128]. To avoid over-fitting, nonlinearity was penalized using restricted maximum likelihood (REML). Participant sex and in-scanner head motion were included as covariates within each GAM. Head motion was quantified as the mean framewise root-mean-square displacement across the three functional runs for each subject. Age was modeled using a penalized thin-plate regression spline; covariates were modeled as parametric regressors. This model can summarized using the formula in Eq. 6:

$$FC \sim s(age) + \beta sex + \beta headmotion FC \sim s(age) + \beta sex + \beta headmotion \quad (6)$$

To quantify the effect sizes of each age spline, we calculated the change in adjusted $R^2$ ($\Delta R^2_{adj.}$) between the full model and a nested model that did not include an effect of age. Statistical significance was assessed using analysis of variance (ANOVA) to compare the full and nested models. Because $\Delta R^2_{adj.}$ describes effect size but not direction (i.e., increasing or decreasing FC with age), we extracted and applied the sign of the age coefficient from an equivalent linear model as in prior work[40]. To estimate windows of significant age-related change for each network-level model, we calculated the age range for which the 95% confidence interval of estimated age splines did not include 0[129,130]. To calculate the intervals, we used the *gratia* package in R[131]. Multiple comparisons were controlled for with the false discovery rate (FDR) correction ($q < .05$).

#### 4.9.2 Modeling the distribution of developmental effects across the functional hierarchy

After analyzing the effect of age on between-network FC, we sought to evaluate the spatial distribution of age effects along the principal gradient. At the network level, we extracted the

mean hierarchy value for each network at each scale and regressed these values on the corresponding pattern of age effects (Eq. 7).

$$Age effect(\triangle R2adj.) \sim \beta hierarchy Age effect(\triangle Radj.2) \sim \beta hierarchy \quad (7)$$

To account for potential non-independence of age effects across scales, significance testing was performed using non-parametric bootstrap resampling. Specifically, we recalculated the age effects for each network and the resulting transmodality relationship across 1000 bootstrap resamples to generate a bootstrapped confidence interval. The effect size of the second-order model was also described as a Spearman's correlation coefficient.

We next evaluated how the magnitude of the age effects corresponded to the span of each edge (between-network connection) across the functional hierarchy. We modeled this effect in two ways. First, we calculated the difference in the hierarchy values for each pair of networks at each scale ("hierarchical distance") and regressed this difference on the age effects from the edge-wise developmental models (Eq. 8).

$$Age effect(\triangle R2adj.) \sim \beta hierarchical distance Age effect(\triangle Radj.2) \sim \beta hierarchical distance \quad (8)$$

As above, significance was evaluated using non-parametric bootstrap resampling. As a sensitivity analysis, we repeated this procedure using the average Euclidean distance between vertices in the two networks comprising each edge. Second, we sought to visualize the interaction between hierarchical distance and age-related changes in coupling across network edges spanning different portions of the functional hierarchy. In order to continuously model the relationship between age-related changes in coupling and hierarchical distance across the functional

hierarchy, we fit a bivariate smooth interaction. Specifically, we modeled the effect of transmodality on the edge-level age effects using a tensor product smooth[132] as in Eq. 9.

$$Ageeffect(\Delta R2adj.) \sim te(HierarchyNetworkA, HierarchyNetworkB) Ageeffect(\Delta R2adj.) \sim te(Hierarchy NetworkA, HierarchyNetworkB) \quad (9)$$

To verify the statistical significance of this model, we performed the same non-parametric bootstrap procedure as above using a simplified linear interaction model.

#### 4.9.3 Modeling scale-dependent developmental effects

In order to quantify and localize the scale-dependence of developmental changes in between-network coupling, we modeled the role of scale on coupling at each vertex. Model formulas and initial model fits were estimated using GAMs (Eq. 10).

$$Networkcoupling \sim s(Scale) + \beta sex + \beta headmotion Networkcoupling \sim s(Scale) + \beta sex + \beta headmotion \quad (10)$$

GAM-derived coefficient estimates for scale, sex, and head motion were used to initialize generalized estimating equations (GEEs). GEEs enabled us to account for the covariance between same-subject measurements across scales without assuming the independence of these observations. At each vertex, the effect of the scale was assessed for statistical significance via a joint Wald test that compared the full model to a nested model that did not include an effect of scale.

Age-by-scale interactions were modeled using the same procedure. First, GAMs were used to generate initial model fits. Age-by-scale interactions were modeled as a bivariate tensor product interaction (*ti* in mgcv) as in Eq. 11.

$$\text{Networkcoupling} \sim s(\text{Scale}) + s(\text{Age}) + ti(\text{Scale},\text{Age}) + \beta_{sex} + \beta_{headmotion} \text{Networkcoupling} \sim s(\text{Scale}) + s(\text{Age}) + ti(\text{Scale},\text{Age}) + \beta_{sex} + \beta_{headmotion} \quad (11)$$

Again, GEEs were used to account for the covariance between same-subject measurements across scales without assuming independence. Statistical significance was evaluated with a joint Wald test that compared the full model to a nested model that did not include a bivariate interaction term.

Finally, to further understand scale-dependent age effects within areas exhibiting age-by-scale interactions, we compared network-level developmental effects across scales for networks that fall at opposite ends of the principal axis. We grouped networks by their maximum overlap with the higher-resolution reference atlas (the 17 network solution provided by Yeo et al.) and calculated average transmodality values for each group of reference networks. The lowest (Somatomotor-A) and highest (Default mode-B) transmodality networks were chosen to depict differential scale dependence across the principal gradient. To illustrate the effect of scale, we fit a penalized spline to the relationship between scale and observed age effects for each network within each group.

### 4.10 Analyses of executive function

#### 4.10.1 Cognitive assessment

The Penn computerized neurocognitive battery (Penn CNB) was administered to all participants as part of a session separate from neuroimaging. The CNB consists of 14 tests adapted from

tasks applied in functional neuroimaging to evaluate a broad range of cognitive domains[133]. These domains include executive function (abstraction and mental flexibility, attention, working memory), episodic memory (verbal, facial, spatial), complex cognition (verbal reasoning, nonverbal reasoning, spatial processing), social cognition (emotion identification, emotion differentiation, age differentiation), and sensorimotor and motor speed. Accuracy for each test was z transformed. As previously described in detail, factor analysis was used to summarize these accuracy scores into three factors[134], including executive and complex cognition, episodic memory, and social cognition. Here, we focused on the executive and complex cognition factor score; episodic memory and social cognition factor scores were evaluated in specificity analyses.

### 4.11 Cognitive modeling

Analyses of associations with cognition were executed using GAMs, as described above for developmental analyses. Specifically, EF was modeled using a penalized regression spline, while co-varying for age using a penalized regression spline; participant sex and mean head motion were included as linear covariates (Eq. 12).

$$FC \sim s(EF)+s(age)+\beta sex+\beta headmotion FC \sim s(EF)+s(age)+\beta sex+\beta headmotion \quad (12)$$

As for developmental analyses, we calculated the effect size as the change in adjusted $R^2$ between the full model and a nested model that did not include the effect of EF ($\Delta R^2_{adj.}$).

### 4.12 Linking associations with EF to the principal gradient of brain organization

After analyzing the effect of cognition on between-network FC, we sought to evaluate the distribution of EF effects across the sensorimotor to association hierarchy. At the network level, we extracted the mean hierarchy value for each network at each scale and compared these

values to the corresponding pattern of associations between between-network coupling and EF. As for previous developmental analyses, in order to assess the statistical significance of EF effect-hierarchy correspondence, we also evaluated a second-order model over 1000 bootstrap resamples. However, here we also included quadratic terms (Eq. 13).

$$EFEffect(\Delta R2adj.) \sim \beta Hierarchy + \beta Hierarchy2 EFEffect(\Delta R2adj.) \sim \beta Hierarchy + \beta Hierarchy2 \quad (13)$$

The resulting bootstrapped confidence intervals for $\beta_{Hierarchy}$ and βHierarchy2βHierarchy2 were then used for significance testing of these second-order effects.

### Modeling scale-dependent cognitive effects

In order to quantify and localize the scale dependence of associations between EF and between-network coupling, we modeled the role of scale at each vertex. EF-by-scale interactions were modeled using the same procedure as for developmental models. First, GAMs were used to generate initial model fits. EF-by-scale interactions were modeled as a bivariate tensor product interaction (*ti* in mgcv) as in Eq. 14.

$$FC \sim s(EF) + s(Scale) + s(Age) + ti(Scale,EF) + ti(Scale,Age) + \beta sex + \beta headmotion FC \sim s(EF) + s(Scale) + s(Age) + ti(Scale,EF) + ti(Scale,Age) + \beta sex + \beta headmotion \quad (14)$$

Again, GEEs were used to account for the covariance between same-subject measurements across scales without assuming independence. Statistical significance was evaluated with a joint Wald test that compared the full model to a nested model that did not include a bivariate interaction term.

Finally, to further understand scale-dependent cognitive effects within areas exhibiting EF-by-scale interactions, we compared network-level cognitive effects across scales for networks that fall at opposite ends of the functional hierarchy. To model the effect of scale, we fit a penalized spline to the relationship between scale and observed cognition effects for the lowest (Somatomotor-A) and highest (Default mode-B) order networks.

### 4.13 Multivariate EF predictions

As a final step, we sought to assess the degree to which multivariate patterns of functional edge coupling across scales jointly explain individual differences in executive function. To do this, we used ridge regression[135]. We iteratively fit a regression model to two-thirds of our sample (462 participants) and predicted executive function scores from functional coupling data in the left-out testing third of participants (231 participants). In each iteration, we used nested parameter optimization. Specifically, coefficients for each edge were fit with the 1st third of the sample, and then the L2 penalty term was selected based on predictions in the 2nd third of the sample. Finally, the degree to which functional coupling explains EF was calculated using the unseen 3rd third of the sample. In that left-out data that was not used in model training, we calculated the correlation between actual and predicted EF, as well as the mean squared error (MSE). We repeated this process 100 times to ensure that specific sample splits were not driving results, and averaged predictions across iterations. To evaluate the statistical significance of these predictions, we used permutation testing. Specifically, we repeated this process 1000 times, and compared our outcome measure (correlation of predicted vs. actual EF) versus the distribution of models where EF scores had been permuted across participants.

### 4.14 Reporting summary

Further information on research design is available in the Nature Research Reporting Summary linked to this article.

4.15 Data availability

The Source data generated in this study have been deposited in the Zenodo database under accession https://doi.org/10.5281/zenodo.6288879. The raw neuroimaging data are protected and are not available due to data privacy laws.

4.16 Code availability

The PNC data are publicly available in the Database of Genotypes and Phenotypes: accession number: phs00607.v3.p2; https://www.ncbi.nlm.nih.gov/projects/gap/cgi-bin/study.cgi?study_id=phs000607.v3.p2. All analysis code is available here https://github.com/PennLINC/multiscale, with detailed explanation provided at https://pennlinc.github.io/multiscale/.

5. Bibliography


1. Siegle, J. H., Jia, X., Durand, S., Gale, S., Bennett, C., Graddis, N., Heller, G., Ramirez, T. K., Choi, H., Luviano, J. A., Groblewski, P. A., Ahmed, R., Arkhipov, A., Bernard, A., Billeh, Y. N., Brown, D., Buice, M. A., Cain, N., Caldejon, S., … Koch, C. (2021). Survey of spiking in the mouse visual system reveals functional hierarchy. *Nature*, *592*(7852), 86–92. https://doi.org/10.1038/s41586-020-03171-x
2. Felleman, D. J., & Van Essen, D. C. (1991). Distributed hierarchical processing in the primate cerebral cortex. *Cerebral Cortex (New York, N.Y.: 1991)*, *1*(1), 1–47. https://doi.org/10.1093/cercor/1.1.1
3. Harris, J. A., Mihalas, S., Hirokawa, K. E., Whitesell, J. D., Choi, H., Bernard, A., Bohn, P., Caldejon, S., Casal, L., Cho, A., Feiner, A., Feng, D., Gaudreault, N., Gerfen, C. R., Graddis, N., Groblewski, P. A., Henry, A. M., Ho, A., Howard, R., … Zeng, H. (2019). Hierarchical organization of cortical and thalamic connectivity. *Nature*, *575*(7781), 195–202. https://doi.org/10.1038/s41586-019-1716-z
4. Burt, J. B., Demirtaş, M., Eckner, W. J., Navejar, N. M., Ji, J. L., Martin, W. J., Bernacchia, A., Anticevic, A., & Murray, J. D. (2018). Hierarchy of transcriptomic specialization across human cortex captured by structural neuroimaging topography. *Nature Neuroscience*. https://doi.org/10.1038/s41593-018-0195-0
5. Buckner, R. L., & Krienen, F. M. (2013). The evolution of distributed association networks in the human brain. *Trends in Cognitive Sciences*, *17*(12), 648–665. https://doi.org/10.1016/j.tics.2013.09.017
6. Mesulam, M. M. (1998). From sensation to cognition. *Brain: A Journal of Neurology*, *121 ( Pt 6)*, 1013–1052. https://doi.org/10.1093/brain/121.6.1013
7. Sydnor, V. J., Larsen, B., Bassett, D. S., Alexander-Bloch, A., Fair, D. A., Liston, C., Mackey, A. P., Milham, M. P., Pines, A., Roalf, D. R., Seidlitz, J., Xu, T., Raznahan, A., & Satterthwaite, T. D. (2021) Neurodevelopment of the association cortices: Patterns, mechanisms, and implications for psychopathology. *Neuron*, *109*. https://doi.org/10.1016/j.neuron.2021.06.016

8. Larivière, S., Vos de Wael, R., Hong, S.-J., Paquola, C., Tavakol, S., Lowe, A. J., Schrader, D. V., & Bernhardt, B. C. (2020). Multiscale Structure–Function Gradients in the Neonatal Connectome. *Cerebral Cortex*, *30*(1), 47–58. https://doi.org/10.1093/cercor/bhz069
9. Dong, H.-M., Margulies, D. S., Zuo, X.-N., & Holmes, A. J. (2021). Shifting gradients of macroscale cortical organization mark the transition from childhood to adolescence. *Proceedings of the National Academy of Sciences*, *118*(28) e2024448188. https://doi.org/10.1073/pnas.2024448118
10. Nenning, K.-H., Xu, T., Schwartz, E., Arroyo, J., Woehrer, A., Franco, A. R., Vogelstein, J. T., Margulies, D. S., Liu, H., Smallwood, J., Milham, M. P., & Langs, G. (2020). Joint embedding: A scalable alignment to compare individuals in a connectivity space. *NeuroImage*, *222*, 117232. https://doi.org/10.1016/j.neuroimage.2020.117232
11. Arffa, S. (2007). The relationship of intelligence to executive function and non-executive function measures in a sample of average, above average, and gifted youth. *Archives of Clinical Neuropsychology: The Official Journal of the National Academy of Neuropsychologists*, *22*(8), 969–978. https://doi.org/10.1016/j.acn.2007.08.001
12. Best, J. R., Miller, P. H., & Naglieri, J. A. (2011). Relations between Executive Function and Academic Achievement from Ages 5 to 17 in a Large, Representative National Sample. *Learning and Individual Differences*, *21*(4), 327–336. https://doi.org/10.1016/j.lindif.2011.01.007
13. Casey, B. J., Jones, R. M., & Hare, T. A. (2008). The Adolescent Brain. *Annals of the New York Academy of Sciences*, *1124*, 111–126. https://doi.org/10.1196/annals.1440.010
14. Snyder, H. R., Friedman, N. P., & Hankin, B. L. (2019). Transdiagnostic Mechanisms of Psychopathology in Youth: Executive Functions, Dependent Stress, and Rumination. *Cognitive Therapy and Research*, *43*(5), 834–851. https://doi.org/10.1007/s10608-019-10016-z
15. Shanmugan, S., Wolf, D. H., Calkins, M. E., Moore, T. M., Ruparel, K., Hopson, R. D., Vandekar, S. N., Roalf, D. R., Elliott, M. A., Jackson, C., Gennatas, E. D., Leibenluft, E., Pine, D. S., Shinohara, R. T., Hakonarson, H., Gur, R. C., Gur, R. E., & Satterthwaite, T. D. (2016). Common and Dissociable Mechanisms of Executive System Dysfunction Across Psychiatric Disorders in Youth. *The American Journal of Psychiatry*, *173*(5), 517–526. https://doi.org/10.1176/appi.ajp.2015.15060725
16. Millan, M. J., Agid, Y., Brüne, M., Bullmore, E. T., Carter, C. S., Clayton, N. S., Connor, R., Davis, S., Deakin, B., DeRubeis, R. J., Dubois, B., Geyer, M. A., Goodwin, G. M., Gorwood, P., Jay, T. M., Joëls, M., Mansuy, I. M., Meyer-Lindenberg, A., Murphy, D., Rolls, E., Saletu, B., Spedding, M., Sweeney, J., Whittington, M., & Young, L. J. (2012). Cognitive dysfunction in psychiatric disorders: Characteristics, causes and the quest for improved therapy. *Nature Reviews. Drug Discovery*, *11*(2), 141–168. https://doi.org/10.1038/nrd3628
17. Margulies, D. S., Ghosh, S. S., Goulas, A., Falkiewicz, M., Huntenburg, J. M., Langs, G., Bezgin, G., Eickhoff, S. B., Castellanos, F. X., Petrides, M., Jefferies, E., & Smallwood, J. (2016). Situating the default-mode network along a principal gradient of macroscale cortical organization. *Proceedings of the National Academy of Sciences*, *113*(44), 12574–12579. https://doi.org/10.1073/pnas.1608282113
18. Barber, A. D., Caffo, B. S., Pekar, J. J., & Mostofsky, S. H. (2013). Developmental Changes In Within- and Between-Network Connectivity Between Late Childhood and Adulthood. *Neuropsychologia*, *51*(1), 156–167. https://doi.org/10.1016/j.neuropsychologia.2012.11.011
19. Sherman, L. E., Rudie, J. D., Pfeifer, J. H., Masten, C. L., McNealy, K., & Dapretto, M. (2014). Development of the Default Mode and Central Executive Networks across early adolescence: A longitudinal study. *Developmental Cognitive Neuroscience*, *10*, 148–159. https://doi.org/10.1016/j.dcn.2014.08.002
20. Owens, M. M., Yuan, D., Hahn, S., Albaugh, M., Allgaier, N., Chaarani, B., Potter, A., & Garavan, H. (2020). Investigation of Psychiatric and Neuropsychological Correlates of Default Mode Network and Dorsal Attention Network Anticorrelation in Children. *Cerebral Cortex*, *30*(12), 6083–6096. https://doi.org/10.1093/cercor/bhaa143

21. Zhong, J., Rifkin-Graboi, A., Ta, A. T., Yap, K. L., Chuang, K.-H., Meaney, M. J., & Qiu, A. (2014). Functional Networks in Parallel with Cortical Development Associate with Executive Functions in Children. *Cerebral Cortex*, *24*(7), 1937–1947. https://doi.org/10.1093/cercor/bht051
22. Marek, S., Hwang, K., Foran, W., Hallquist, M. N., & Luna, B. (2015). The Contribution of Network Organization and Integration to the Development of Cognitive Control. *PLoS Biology*, *13*(12), e1002328. https://doi.org/10.1371/journal.pbio.1002328
23. Reineberg, A. E., Andrews-Hanna, J. R., Depue, B. E., Friedman, N. P., & Banich, M. T. (2015). Resting-state networks predict individual differences in common and specific aspects of executive function. *NeuroImage*, *104*, 69–78. https://doi.org/10.1016/j.neuroimage.2014.09.045
24. Dwyer, D. B., Harrison, B. J., Yücel, M., Whittle, S., Zalesky, A., Pantelis, C., Allen, N. B., & Fornito, A. (2014). Large-Scale Brain Network Dynamics Supporting Adolescent Cognitive Control. *Journal of Neuroscience*, *34*(42), 14096–14107. https://doi.org/10.1523/JNEUROSCI.1634-14.2014
25. Engel, T. A., & Steinmetz, N. A. (2019). New perspectives on dimensionality and variability from large-scale cortical dynamics. *Current Opinion in Neurobiology*, *58*, 181–190. https://doi.org/10.1016/j.conb.2019.09.003
26. Betzel, R. F., & Bassett, D. S. (2017). Multi-scale brain networks. *NeuroImage*, *160*, 73–83. https://doi.org/10.1016/j.neuroimage.2016.11.006
27. Eickhoff, S. B., Yeo, B. T. T., & Genon, S. (2018). Imaging-based parcellations of the human brain. *Nature Reviews Neuroscience*, *19*(11), 672–686. https://doi.org/10.1038/s41583-018-0071-7
28. Breakspear, M., & Stam, C. J. (2005). Dynamics of a neural system with a multiscale architecture. *Philosophical Transactions of the Royal Society B: Biological Sciences*, *360*(1457), 1051–1074. https://doi.org/10.1098/rstb.2005.1643
29. Yeo, B. T. T., Krienen, F. M., Chee, M. W. L., & Buckner, R. L. (2014). Estimates of segregation and overlap of functional connectivity networks in the human cerebral cortex. *NeuroImage*, *88*, 212–227. https://doi.org/10.1016/j.neuroimage.2013.10.046
30. Faskowitz, J., Esfahlani, F. Z., Jo, Y., Sporns, O., & Betzel, R. F. (2020). Edge-centric functional network representations of human cerebral cortex reveal overlapping system-level architecture. *Nature Neuroscience*, *23*(12), 1644–1654. https://doi.org/10.1038/s41593-020-00719-y
31. LaBar, K. S., Gitelman, D. R., Parrish, T. B., & Mesulam, M. (1999). Neuroanatomic overlap of working memory and spatial attention networks: A functional MRI comparison within subjects. *NeuroImage*, *10*(6), 695–704. https://doi.org/10.1006/nimg.1999.0503
32. Betzel, R. F., Bertolero, M. A., Gordon, E. M., Gratton, C., Dosenbach, N. U. F., & Bassett, D. S. (2019). The community structure of functional brain networks exhibits scale-specific patterns of inter- and intra-subject variability. *NeuroImage*, *202*, 115990. https://doi.org/10.1016/j.neuroimage.2019.07.003
33. de Reus, M. A., & van den Heuvel, M. P. (2013). The parcellation-based connectome: Limitations and extensions. *NeuroImage*, *80*, 397–404. https://doi.org/10.1016/j.neuroimage.2013.03.053
34. Arslan, S., Ktena, S. I., Makropoulos, A., Robinson, E. C., Rueckert, D., & Parisot, S. (2018). Human brain mapping: A systematic comparison of parcellation methods for the human cerebral cortex. *NeuroImage*, *170*, 5–30. https://doi.org/10.1016/j.neuroimage.2017.04.014
35. Bijsterbosch, J. D., Woolrich, M. W., Glasser, M. F., Robinson, E. C., Beckmann, C. F., Van Essen, D. C., Harrison, S. J., & Smith, S. M. (2018). The relationship between spatial configuration and functional connectivity of brain regions. *ELife*, *7*. https://doi.org/10.7554/eLife.32992
36. Kong, R., Li, J., Orban, C., Sabuncu, M. R., Liu, H., Schaefer, A., Sun, N., Zuo, X.-N., Holmes, A. J., Eickhoff, S. B., & Yeo, B. T. T. (2018). Spatial Topography of Individual-Specific Cortical Networks Predicts Human Cognition, Personality, and Emotion. *Cerebral Cortex (New York, N.Y.: 1991)*. https://doi.org/10.1093/cercor/bhy123

37. Li, M., Wang, D., Ren, J., Langs, G., Stoecklein, S., Brennan, B. P., Lu, J., Chen, H., & Liu, H. (2019). Performing group-level functional image analyses based on homologous functional regions mapped in individuals. *PLOS Biology*, *17*(3), e2007032. https://doi.org/10.1371/journal.pbio.2007032
38. Xu, T., Opitz, A., Craddock, R. C., Wright, M. J., Zuo, X.-N., & Milham, M. P. (2016). Assessing Variations in Areal Organization for the Intrinsic Brain: From Fingerprints to Reliability. *Cerebral Cortex (New York, NY)*, *26*(11), 4192–4211. https://doi.org/10.1093/cercor/bhw241
39. Gordon, E. M., Laumann, T. O., Adeyemo, B., & Petersen, S. E. (2017). Individual Variability of the System-Level Organization of the Human Brain. *Cerebral Cortex*, *27*(1), 386–399. https://doi.org/10.1093/cercor/bhv239
40. Cui, Z., Li, H., Xia, C. H., Larsen, B., Adebimpe, A., Baum, G. L., Cieslak, M., Gur, R. E., Gur, R. C., Moore, T. M., Oathes, D. J., Alexander-Bloch, A. F., Raznahan, A., Roalf, D. R., Shinohara, R. T., Wolf, D. H., Davatzikos, C., Bassett, D. S., Fair, D. A., Fan, Y., & Satterthwaite, T. D. (2020). Individual Variation in Functional Topography of Association Networks in Youth. *Neuron*, *106*(2), 340-353.e8. https://doi.org/10.1016/j.neuron.2020.01.029
41. Burger, B., Nenning, K.-H., Schwartz, E., Margulies, D. S., Goulas, A., Liu, H., Neubauer, S., Dauwels, J., Prayer, D., & Langs, G. (2021). Disentangling cortical functional connectivity strength and topography reveals divergent roles of genes and environment. *Neuroimage*, *247*, https://doi.org/10.1016/j.neuroimage.2021.118770
42. Benkarim, O., Paquola, C., Park, B., Hong, S.-J., Royer, J., Vos de Wael, R., Lariviere, S., Valk, S., Bzdok, D., Mottron, L., & C. Bernhardt, B. (2021). Connectivity alterations in autism reflect functional idiosyncrasy. *Communications Biology*, *4*(1), 1–15. https://doi.org/10.1038/s42003-021-02572-6
43. Bijsterbosch, J., Harrison, S. J., Jbabdi, S., Woolrich, M., Beckmann, C., Smith, S., & Duff, E. P. (2020). Challenges and future directions for representations of functional brain organization. *Nature Neuroscience*, *23*(12), 1484–1495. https://doi.org/10.1038/s41593-020-00726-z
44. Braga, R. M., & Buckner, R. L. (2017). Parallel Interdigitated Distributed Networks within the Individual Estimated by Intrinsic Functional Connectivity. *Neuron*, *95*(2), 457-471.e5. https://doi.org/10.1016/j.neuron.2017.06.038
45. Satterthwaite, T. D., Elliott, M. A., Ruparel, K., Loughead, J., Prabhakaran, K., Calkins, M. E., Hopson, R., Jackson, C., Keefe, J., Riley, M., Mentch, F. D., Sleiman, P., Verma, R., Davatzikos, C., Hakonarson, H., Gur, R. C., & Gur, R. E. (2014). Neuroimaging of the Philadelphia neurodevelopmental cohort. *NeuroImage*, *86*, 544–553. https://doi.org/10.1016/j.neuroimage.2013.07.064
46. Lee, D. D., & Seung, H. S. (1999). Learning the parts of objects by non-negative matrix factorization. *Nature*, *401*(6755), 788. https://doi.org/10.1038/44565
47. Li, H., Satterthwaite, T., & Fan, Y. (2017). Large-scale sparse functional networks from resting state fMRI. *NeuroImage*, *156*, 1–13. https://doi.org/10.1016/j.neuroimage.2017.05.004
48. Yeo, B. T. T., Krienen, F. M., Sepulcre, J., Sabuncu, M. R., Lashkari, D., Hollinshead, M., Roffman, J. L., Smoller, J. W., Zöllei, L., Polimeni, J. R., Fischl, B., Liu, H., & Buckner, R. L. (2011). The organization of the human cerebral cortex estimated by intrinsic functional connectivity. *Journal of Neurophysiology*, *106*(3), 1125–1165. https://doi.org/10.1152/jn.00338.2011
49. Alexander-Bloch, A. F., Shou, H., Liu, S., Satterthwaite, T. D., Glahn, D. C., Shinohara, R. T., Vandekar, S. N., & Raznahan, A. (2018). On testing for spatial correspondence between maps of human brain structure and function. *NeuroImage*, *178*, 540–551. https://doi.org/10.1016/j.neuroimage.2018.05.070
50. Fair, D. A., Dosenbach, N. U. F., Church, J. A., Cohen, A. L., Brahmbhatt, S., Miezin, F. M., Barch, D. M., Raichle, M. E., Petersen, S. E., & Schlaggar, B. L. (2007a). Development of distinct control networks through segregation and integration. *Proceedings of the National Academy of Sciences*, *104*(33), 13507–13512. https://doi.org/10.1073/pnas.0705843104

51. Power, J. D., Fair, D. A., Schlaggar, B. L., & Petersen, S. E. (2010). The Development of Human Functional Brain Networks. *Neuron*, *67*(5), 735–748. https://doi.org/10.1016/j.neuron.2010.08.017
52. Ma, Z., Tu, W., & Zhang, N. (2021). Increased wiring cost during development is driven by long-range cortical, but not subcortical connections. *NeuroImage*, *225*, 117463. https://doi.org/10.1016/j.neuroimage.2020.117463
53. Oligschläger, S., Huntenburg, J. M., Golchert, J., Lauckner, M. E., Bonnen, T., & Margulies, D. S. (2017). Gradients of connectivity distance are anchored in primary cortex. *Brain Structure & Function*, *222*(5), 2173–2182. https://doi.org/10.1007/s00429-016-1333-7
54. Huntenburg, J. M., Bazin, P.-L., & Margulies, D. S. (2018). Large-Scale Gradients in Human Cortical Organization. *Trends in Cognitive Sciences*, *22*(1), 21–31. https://doi.org/10.1016/j.tics.2017.11.002
55. Vainik, U., Paquola, C., Wang, X., Zheng, Y., Bernhardt, B., Misic, B., & Dagher, A. (2020). Heritability of cortical morphology reflects a sensory-fugal plasticity gradient. *BioRxiv*, 2020.11.03.366419. https://doi.org/10.1101/2020.11.03.366419
56. Paquola, C., Bethlehem, R. A., Seidlitz, J., Wagstyl, K., Romero-Garcia, R., Whitaker, K. J., Vos de Wael, R., Williams, G. B., NSPN Consortium, Vértes, P. E., Margulies, D. S., Bernhardt, B., & Bullmore, E. T. (2019). Shifts in myeloarchitecture characterise adolescent development of cortical gradients. *ELife*, *8*, e50482. https://doi.org/10.7554/eLife.50482
57. Park, B., Bethlehem, R. A., Paquola, C., Larivière, S., Rodríguez-Cruces, R., Vos de Wael, R., Neuroscience in Psychiatry Network (NSPN) Consortium, Bullmore, E. T., & Bernhardt, B. C. (2021). An expanding manifold in transmodal regions characterizes adolescent reconfiguration of structural connectome organization. *ELife*, *10*, e64694. https://doi.org/10.7554/eLife.64694
58. Mitra, A., & Raichle, M. E. (2016). How networks communicate: Propagation patterns in spontaneous brain activity. *Philosophical Transactions of the Royal Society B: Biological Sciences*, *371*(1705), 20150546. https://doi.org/10.1098/rstb.2015.0546
59. Matsui, T., Murakami, T., & Ohki, K. (2016). Transient neuronal coactivations embedded in globally propagating waves underlie resting-state functional connectivity. *Proceedings of the National Academy of Sciences*, *113*(23), 6556–6561. https://doi.org/10.1073/pnas.1521299113
60. Gu, Y., Sainburg, L. E., Kuang, S., Han, F., Williams, J. W., Liu, Y., Zhang, N., Zhang, X., Leopold, D. A., & Liu, X. (2021). Brain Activity Fluctuations Propagate as Waves Traversing the Cortical Hierarchy. *Cerebral Cortex (New York, N.Y.: 1991)*. https://doi.org/10.1093/cercor/bhab064
61. Satterthwaite, T. D., Wolf, D. H., Erus, G., Ruparel, K., Elliott, M. A., Gennatas, E. D., Hopson, R., Jackson, C., Prabhakaran, K., Bilker, W. B., Calkins, M. E., Loughead, J., Smith, A., Roalf, D. R., Hakonarson, H., Verma, R., Davatzikos, C., Gur, R. C., & Gur, R. E. (2013a). Functional Maturation of the Executive System during Adolescence. *Journal of Neuroscience*, *33*(41), 16249–16261. https://doi.org/10.1523/JNEUROSCI.2345-13.2013
62. Tan, Z., Robinson, H. L., Yin, D.-M., Liu, Y., Liu, F., Wang, H., Lin, T. W., Xing, G., Gan, L., Xiong, W.-C., & Mei, L. (2018). Dynamic ErbB4 Activity in Hippocampal-Prefrontal Synchrony and Top-Down Attention in Rodents. *Neuron*, *98*(2), 380-393.e4. https://doi.org/10.1016/j.neuron.2018.03.018
63. Murphy, A. C., Bertolero, M. A., Papadopoulos, L., Lydon-Staley, D. M., & Bassett, D. S. (2020). Multimodal network dynamics underpinning working memory. *Nature Communications*, *11*(1), 3035. https://doi.org/10.1038/s41467-020-15541-0
64. Baum, G. L., Ciric, R., Roalf, D. R., Betzel, R. F., Moore, T. M., Shinohara, R. T., Kahn, A. E., Vandekar, S. N., Rupert, P. E., Quarmley, M., Cook, P. A., Elliott, M. A., Ruparel, K., Gur, R. E., Gur, R. C., Bassett, D. S., & Satterthwaite, T. D. (2017). Modular Segregation of Structural Brain Networks Supports the Development of Executive Function in Youth. *Current Biology: CB*, *27*(11), 1561-1572.e8. https://doi.org/10.1016/j.cub.2017.04.051

65. Grayson, D. S., & Fair, D. A. (2017). Development of large-scale functional networks from birth to adulthood: A guide to the neuroimaging literature. *NeuroImage*, *160*, 15–31. https://doi.org/10.1016/j.neuroimage.2017.01.079
66. He, W., Sowman, P. F., Brock, J., Etchell, A. C., Stam, C. J., & Hillebrand, A. (2019). Increased segregation of functional networks in developing brains. *NeuroImage*, *200*, 607–620. https://doi.org/10.1016/j.neuroimage.2019.06.055
67. Murphy, C., Wang, H.-T., Konu, D., Lowndes, R., Margulies, D. S., Jefferies, E., & Smallwood, J. (2019). Modes of operation: A topographic neural gradient supporting stimulus dependent and independent cognition. *NeuroImage*, *186*, 487–496. https://doi.org/10.1016/j.neuroimage.2018.11.009
68. Murphy, C., Jefferies, E., Rueschemeyer, S.-A., Sormaz, M., Wang, H., Margulies, D. S., & Smallwood, J. (2018). Distant from input: Evidence of regions within the default mode network supporting perceptually-decoupled and conceptually-guided cognition. *NeuroImage*, *171*, 393–401. https://doi.org/10.1016/j.neuroimage.2018.01.017
69. Niendam, T. A., Laird, A. R., Ray, K. L., Dean, Y. M., Glahn, D. C., & Carter, C. S. (2012). Meta-analytic evidence for a superordinate cognitive control network subserving diverse executive functions. *Cognitive, Affective, & Behavioral Neuroscience*, *12*(2), 241–268. https://doi.org/10.3758/s13415-011-0083-5
70. Cole, M. W., Reynolds, J. R., Power, J. D., Repovs, G., Anticevic, A., & Braver, T. S. (2013). Multi-task connectivity reveals flexible hubs for adaptive task control. *Nature Neuroscience*, *16*(9), 1348–1355. https://doi.org/10.1038/nn.3470
71. Marek, S., & Dosenbach, N. U. F. (2018). The frontoparietal network: Function, electrophysiology, and importance of individual precision mapping. *Dialogues in Clinical Neuroscience*, *20*(2), 133–140.
72. Sonuga-Barke, E. J. S., & Castellanos, F. X. (2007). Spontaneous attentional fluctuations in impaired states and pathological conditions: A neurobiological hypothesis. *Neuroscience & Biobehavioral Reviews*, *31*(7), 977–986. https://doi.org/10.1016/j.neubiorev.2007.02.005
73. Bomyea, J., Taylor, C. T., Spadoni, A. D., & Simmons, A. N. (2018). Neural mechanisms of interference control in working memory capacity. *Human Brain Mapping*, *39*(2), 772–782. https://doi.org/10.1002/hbm.23881
74. Betzel, R. F., Byrge, L., He, Y., Goñi, J., Zuo, X.-N., & Sporns, O. (2014). Changes in structural and functional connectivity among resting-state networks across the human lifespan. *NeuroImage*, *102*, 345–357. https://doi.org/10.1016/j.neuroimage.2014.07.067
75. Chan, M. Y., Park, D. C., Savalia, N. K., Petersen, S. E., & Wig, G. S. (2014). Decreased segregation of brain systems across the healthy adult lifespan. *Proceedings of the National Academy of Sciences*, *111*(46), E4997–E5006. https://doi.org/10.1073/pnas.1415122111
76. Park, D. C., Polk, T. A., Park, R., Minear, M., Savage, A., & Smith, M. R. (2004). Aging reduces neural specialization in ventral visual cortex. *Proceedings of the National Academy of Sciences*, *101*(35), 13091–13095. https://doi.org/10.1073/pnas.0405148101
77. Goh, J. O. S. (2011). Functional Dedifferentiation and Altered Connectivity in Older Adults: Neural Accounts of Cognitive Aging. *Aging and Disease*, *2*(1), 30–48.
78. Chan, M. Y., Han, L., Carreno, C. A., Zhang, Z., Rodriguez, R. M., LaRose, M., Hassenstab, J., & Wig, G. S. (2021). Long-term prognosis and educational determinants of brain network decline in older adult individuals. *Nature Aging*, *1*(11), 1053–1067. https://doi.org/10.1038/s43587-021-00125-4
79. Geerligs, L., Maurits, N. M., Renken, R. J., & Lorist, M. M. (2014). Reduced specificity of functional connectivity in the aging brain during task performance. *Human Brain Mapping*, *35*(1), 319–330. https://doi.org/10.1002/hbm.22175
80. Cassady, K. E., Adams, J. N., Chen, X., Maass, A., Harrison, T. M., Landau, S., Baker, S., & Jagust, W. (2021). Alzheimer's Pathology Is Associated with Dedifferentiation of Intrinsic Functional Memory Networks in Aging. *Cerebral Cortex*, *bhab122*. https://doi.org/10.1093/cercor/bhab122
81. Doucet, G., Naveau, M., Petit, L., Delcroix, N., Zago, L., Crivello, F., Jobard, G., Tzourio-Mazoyer, N., Mazoyer, B., Mellet, E., & Joliot, M. (2011). Brain activity at rest: A multiscale

hierarchical functional organization. *Journal of Neurophysiology*, *105*(6), 2753–2763. https://doi.org/10.1152/jn.00895.2010
82. Shokri-Kojori, E., Tomasi, D., Alipanahi, B., Wiers, C. E., Wang, G.-J., & Volkow, N. D. (2019). Correspondence between cerebral glucose metabolism and BOLD reveals relative power and cost in human brain. *Nature Communications*, *10*(1), 690. https://doi.org/10.1038/s41467-019-08546-x
83. Seeley, W. W., Crawford, R. K., Zhou, J., Miller, B. L., & Greicius, M. D. (2009). Neurodegenerative diseases target large-scale human brain networks. *Neuron*, *62*(1), 42–52. https://doi.org/10.1016/j.neuron.2009.03.024
84. Uddin, L. Q., Yeo, B. T. T., & Spreng, R. N. (2019). Towards a Universal Taxonomy of Macro-scale Functional Human Brain Networks. *Brain Topography*, *32*(6), 926–942. https://doi.org/10.1007/s10548-019-00744-6
85. Power, J. D., Fair, D. A., Schlaggar, B. L., & Petersen, S. E. (2010). The Development of Human Functional Brain Networks. *Neuron*, *67*(5), 735–748. https://doi.org/10.1016/j.neuron.2010.08.017
86. Bazinet, V., Vos de Wael, R., Hagmann, P., Bernhardt, B. C., & Misic, B. (2021). Multiscale communication in cortico-cortical networks. *NeuroImage*, *243*, 118546. https://doi.org/10.1016/j.neuroimage.2021.118546
87. Esfahlani, F. Z., Bertolero, M. A., Bassett, D. S., & Betzel, R. F. (2020). Space-independent community and hub structure of functional brain networks. *NeuroImage*, *211*, 116612. https://doi.org/10.1016/j.neuroimage.2020.116612
88. Power, J. D., Cohen, A. L., Nelson, S. M., Wig, G. S., Barnes, K. A., Church, J. A., Vogel, A. C., Laumann, T. O., Miezin, F. M., Schlaggar, B. L., & Petersen, S. E. (2011). Functional network organization of the human brain. *Neuron*, *72*(4), 665–678. https://doi.org/10.1016/j.neuron.2011.09.006
89. Yeo, B. T. T., Krienen, F. M., Eickhoff, S. B., Yaakub, S. N., Fox, P. T., Buckner, R. L., Asplund, C. L., & Chee, M. W. L. (2015). Functional Specialization and Flexibility in Human Association Cortex. *Cerebral Cortex (New York, NY)*, *25*(10), 3654–3672. https://doi.org/10.1093/cercor/bhu217
90. Tooley, U. A., Bassett, D. S., & Mackey, A. P. (2021). Environmental influences on the pace of brain development. *Nature Reviews Neuroscience*, 1–13. https://doi.org/10.1038/s41583-021-00457-5
91. Di Martino, A., Fair, D. A., Kelly, C., Satterthwaite, T. D., Castellanos, F. X., Thomason, M. E., Craddock, R. C., Luna, B., Leventhal, B. L., Zuo, X.-N., & Milham, M. P. (2014). Unraveling the Miswired Connectome: A Developmental Perspective. *Neuron*, *83*(6), 1335–1353. https://doi.org/10.1016/j.neuron.2014.08.050
92. Satterthwaite, T. D., Wolf, D. H., Ruparel, K., Erus, G., Elliott, M. A., Eickhoff, S. B., Gennatas, E. D., Jackson, C., Prabhakaran, K., Smith, A., Hakonarson, H., Verma, R., Davatzikos, C., Gur, R. E., & Gur, R. C. (2013b). Heterogeneous impact of motion on fundamental patterns of developmental changes in functional connectivity during youth. *NeuroImage*, *83*, 45–57. https://doi.org/10.1016/j.neuroimage.2013.06.045
93. Ciric, R., Wolf, D. H., Power, J. D., Roalf, D. R., Baum, G. L., Ruparel, K., Shinohara, R. T., Elliott, M. A., Eickhoff, S. B., Davatzikos, C., Gur, R. C., Gur, R. E., Bassett, D. S., & Satterthwaite, T. D. (2017). Benchmarking of participant-level confound regression strategies for the control of motion artifact in studies of functional connectivity. *NeuroImage*, *154*, 174–187. https://doi.org/10.1016/j.neuroimage.2017.03.020
94. Fair, D. A., Schlaggar, B. L., Cohen, A. L., Miezin, F. M., Dosenbach, N. U. F., Wenger, K. K., Fox, M. D., Snyder, A. Z., Raichle, M. E., & Petersen, S. E. (2007b). A method for using blocked and event-related fMRI data to study “resting state” functional connectivity. *NeuroImage*, *35*(1), 396–405. https://doi.org/10.1016/j.neuroimage.2006.11.051
95. Gratton, C., Laumann, T. O., Nielsen, A. N., Greene, D. J., Gordon, E. M., Gilmore, A. W., Nelson, S. M., Coalson, R. S., Snyder, A. Z., Schlaggar, B. L., Dosenbach, N. U. F., & Petersen, S. E. (2018). Functional Brain Networks Are Dominated by Stable Group and

Individual Factors, Not Cognitive or Daily Variation. *Neuron*, *98*(2), 439-452.e5. https://doi.org/10.1016/j.neuron.2018.03.035
96. Laumann, T. O., Gordon, E. M., Adeyemo, B., Snyder, A. Z., Joo, S. J., Chen, M.-Y., Gilmore, A. W., McDermott, K. B., Nelson, S. M., Dosenbach, N. U. F., Schlaggar, B. L., Mumford, J. A., Poldrack, R. A., & Petersen, S. E. (2015). Functional System and Areal Organization of a Highly Sampled Individual Human Brain. *Neuron*, *87*(3), 657–670. https://doi.org/10.1016/j.neuron.2015.06.037
97. Palva, S., & Palva, J. M. (2018). Roles of Brain Criticality and Multiscale Oscillations in Temporal Predictions for Sensorimotor Processing. *Trends in Neurosciences*, *41*(10), 729–743. https://doi.org/10.1016/j.tins.2018.08.008
98. Buzsáki, G., & Draguhn, A. (2004). Neuronal oscillations in cortical networks. *Science (New York, N.Y.)*, *304*(5679), 1926–1929. https://doi.org/10.1126/science.1099745
99. Smith, S. M., Miller, K. L., Moeller, S., Xu, J., Auerbach, E. J., Woolrich, M. W., Beckmann, C. F., Jenkinson, M., Andersson, J., Glasser, M. F., Essen, D. C. V., Feinberg, D. A., Yacoub, E. S., & Ugurbil, K. (2012). Temporally-independent functional modes of spontaneous brain activity. *Proceedings of the National Academy of Sciences*, *109*(8), 3131–3136. https://doi.org/10.1073/pnas.1121329109
100. Vidaurre, D., Smith, S. M., & Woolrich, M. W. (2017). Brain network dynamics are hierarchically organized in time. *Proceedings of the National Academy of Sciences*, *114*(48), 12827–12832. https://doi.org/10.1073/pnas.1705120114
101. Mills, K. L., Goddings, A.-L., Clasen, L. S., Giedd, J. N., & Blakemore, S.-J. (2014). The Developmental Mismatch in Structural Brain Maturation during Adolescence. *Developmental Neuroscience*, *36*(3–4), 147–160. https://doi.org/10.1159/000362328
102. Raznahan, A., Shaw, P. W., Lerch, J. P., Clasen, L. S., Greenstein, D., Berman, R., Pipitone, J., Chakravarty, M. M., & Giedd, J. N. (2014). Longitudinal four-dimensional mapping of subcortical anatomy in human development. *Proceedings of the National Academy of Sciences*, *111*(4), 1592–1597. https://doi.org/10.1073/pnas.1316911111
103. Greene, D. J., Marek, S., Gordon, E. M., Siegel, J. S., Gratton, C., Laumann, T. O., Gilmore, A. W., Berg, J. J., Nguyen, A. L., Dierker, D., Van, A. N., Ortega, M., Newbold, D. J., Hampton, J. M., Nielsen, A. N., McDermott, K. B., Roland, J. L., Norris, S. A., Nelson, S. M., … Dosenbach, N. U. F. (2020). Integrative and Network-Specific Connectivity of the Basal Ganglia and Thalamus Defined in Individuals. *Neuron*, *105*(4), 742-758.e6. https://doi.org/10.1016/j.neuron.2019.11.012
104. Sylvester, C. M., Yu, Q., Srivastava, A. B., Marek, S., Zheng, A., Alexopoulos, D., Smyser, C. D., Shimony, J. S., Ortega, M., Dierker, D. L., Patel, G. H., Nelson, S. M., Gilmore, A. W., McDermott, K. B., Berg, J. J., Drysdale, A. T., Perino, M. T., Snyder, A. Z., Raut, R. V., … Dosenbach, N. U. F. (2020). Individual-specific functional connectivity of the amygdala: A substrate for precision psychiatry. *Proceedings of the National Academy of Sciences*, *117*(7), 3808–3818.
105. Tian, Y., Margulies, D. S., Breakspear, M., & Zalesky, A. (2020). Topographic organization of the human subcortex unveiled with functional connectivity gradients. *Nature Neuroscience*, *23*(11), 1421–1432. https://doi.org/10.1038/s41593-020-00711-6
106. Raut, R. V., Snyder, A. Z., & Raichle, M. E. (2020). Hierarchical dynamics as a macroscopic organizing principle of the human brain. *Proceedings of the National Academy of Sciences*, *117*(34), 20890–20897. https://doi.org/10.1073/pnas.2003383117
107. Romer, A. L., Elliott, M. L., Knodt, A. R., Sison, M. L., Ireland, D., Houts, R., Ramrakha, S., Poulton, R., Keenan, R., Melzer, T. R., Moffitt, T. E., Caspi, A., & Hariri, A. R. (2020). Pervasively Thinner Neocortex as a Transdiagnostic Feature of General Psychopathology. *American Journal of Psychiatry*, *178*(2), 174–182. https://doi.org/10.1176/appi.ajp.2020.19090934
108. Parkes, L., Moore, T. M., Calkins, M. E., Cieslak, M., Roalf, D. R., Wolf, D. H., Gur, R. C., Gur, R. E., Satterthwaite, T. D., & Bassett, D. S. (2021). Network Controllability in Transmodal Cortex Predicts Psychosis Spectrum Symptoms. Biological Psychiatry, 89(9), S370–S371. https://doi.org/10.1016/j.biopsych.2021.02.922

109. Xia, C. H., Ma, Z., Ciric, R., Gu, S., Betzel, R. F., Kaczkurkin, A. N., Calkins, M. E., Cook, P. A., Garza, A. G. de la, Vandekar, S. N., Cui, Z., Moore, T. M., Roalf, D. R., Ruparel, K., Wolf, D. H., Davatzikos, C., Gur, R. C., Gur, R. E., Shinohara, R. T., Bassett, D. S., & Satterthwaite, T. D. (2018). Linked dimensions of psychopathology and connectivity in functional brain networks. *Nature Communications*, *9*(1), 3003.
110. Wolf, D. H., Satterthwaite, T. D., Calkins, M. E., Ruparel, K., Elliott, M. A., Hopson, R. D., Jackson, C. T., Prabhakaran, K., Bilker, W. B., Hakonarson, H., Gur, R. C., & Gur, R. E. (2015). Functional neuroimaging abnormalities in youth with psychosis spectrum symptoms. *JAMA Psychiatry*, *72*(5), 456–465.
111. Fischl, B. (2012). FreeSurfer. *NeuroImage*, *62*(2), 774–781.
112. Ciric, R., Rosen, A. F. G., Erus, G., Cieslak, M., Adebimpe, A., Cook, P. A., Bassett, D. S., Davatzikos, C., Wolf, D. H., & Satterthwaite, T. D. (2018). Mitigating head motion artifact in functional connectivity MRI. *Nature Protocols*, *13*(12), 2801. https://doi.org/10.1038/s41596-018-0065-y
113. Jenkinson, M., Beckmann, C. F., Behrens, T. E. J., Woolrich, M. W., & Smith, S. M. (2012). FSL. *NeuroImage*, *62*(2), 782–790. https://doi.org/10.1016/j.neuroimage.2011.09.015
114. Smith, S. M., Jenkinson, M., Woolrich, M. W., Beckmann, C. F., Behrens, T. E. J., Johansen-Berg, H., Bannister, P. R., De Luca, M., Drobnjak, I., Flitney, D. E., Niazy, R. K., Saunders, J., Vickers, J., Zhang, Y., De Stefano, N., Brady, J. M., & Matthews, P. M. (2004). Advances in functional and structural MR image analysis and implementation as FSL. *NeuroImage*, *23*, S208–S219. https://doi.org/10.1016/j.neuroimage.2004.07.051
115. Cox, R. W. (1996). AFNI: Software for Analysis and Visualization of Functional Magnetic Resonance Neuroimages. *Computers and Biomedical Research*, *29*(3), 162–173. https://doi.org/10.1006/cbmr.1996.0014
116. Greve, D. N., & Fischl, B. (2009). Accurate and robust brain image alignment using boundary-based registration. *NeuroImage*, *48*(1), 63–72. https://doi.org/10.1016/j.neuroimage.2009.06.060
117. Hallquist, M. N., Hwang, K., & Luna, B. (2013). The nuisance of nuisance regression: Spectral misspecification in a common approach to resting-state fMRI preprocessing reintroduces noise and obscures functional connectivity. *NeuroImage*, *82*, 208–225. https://doi.org/10.1016/j.neuroimage.2013.05.116
118. Gordon, E. M., Laumann, T. O., Adeyemo, B., Huckins, J. F., Kelley, W. M., & Petersen, S. E. (2016). Generation and Evaluation of a Cortical Area Parcellation from Resting-State Correlations. *Cerebral Cortex*, *26*(1), 288–303. https://doi.org/10.1093/cercor/bhu239
119. Ojemann, J. G., Akbudak, E., Snyder, A. Z., McKinstry, R. C., Raichle, M. E., & Conturo, T. E. (1997). Anatomic Localization and Quantitative Analysis of Gradient Refocused Echo-Planar fMRI Susceptibility Artifacts. *NeuroImage*, *6*(3)s, 156–167. https://doi.org/10.1006/nimg.1997.0289
120. Wig, G. S., Laumann, T. O., & Petersen, S. E. (2014). An approach for parcellating human cortical areas using resting-state correlations. *NeuroImage*, *93*, 276–291. https://doi.org/10.1016/j.neuroimage.2013.07.035
121. Sotiras, A., Toledo, J. B., Gur, R. E., Gur, R. C., Satterthwaite, T. D., & Davatzikos, C. (2017). Patterns of coordinated cortical remodeling during adolescence and their associations with functional specialization and evolutionary expansion. *Proceedings of the National Academy of Sciences*, *114*(13), 3527–3532. https://doi.org/10.1073/pnas.1620928114
122. Gordon, E. M., Laumann, T. O., Gilmore, A. W., Newbold, D. J., Greene, D. J., Berg, J. J., Ortega, M., Hoyt-Drazen, C., Gratton, C., Sun, H., Hampton, J. M., Coalson, R. S., Nguyen, A. L., McDermott, K. B., Shimony, J. S., Snyder, A. Z., Schlaggar, B. L., Petersen, S. E., Nelson, S. M., & Dosenbach, N. U. F. (2017b). Precision Functional Mapping of Individual Human Brains. *Neuron*, *95*(4), 791-807.e7. https://doi.org/10.1016/j.neuron.2017.07.011
123. Wang, D., Li, M., Wang, M., Schoeppe, F., Ren, J., Chen, H., Öngür, D., Brady, R. O., Baker, J. T., & Liu, H. (2020). Individual-specific functional connectivity markers track dimensional and categorical features of psychotic illness. *Molecular Psychiatry*, *25*(9), 2119–2129. https://doi.org/10.1038/s41380-018-0276-1

124. Cai, D., He, X., Han, J., & Huang, T. S. (2011). Graph Regularized Nonnegative Matrix Factorization for Data Representation. *IEEE Transactions on Pattern Analysis and Machine Intelligence*, *33*(8), 1548–1560. https://doi.org/10.1109/TPAMI.2010.231
125. Vandekar, S. N., Shinohara, R. T., Raznahan, A., Roalf, D. R., Ross, M., DeLeo, N., Ruparel, K., Verma, R., Wolf, D. H., Gur, R. C., Gur, R. E., & Satterthwaite, T. D. (2015). Topologically Dissociable Patterns of Development of the Human Cerebral Cortex. *The Journal of Neuroscience*, *35*(2), 599–609. https://doi.org/10.1523/JNEUROSCI.3628-14.2015
126. Wood, S. (2001). Mgcv: GAMs and generalized ridge regression for R. *R News*, *1*, 20-25.
127. Wood, S. (2004). Stable and Efficient Multiple Smoothing Parameter Estimation for Generalized Additive Models. *Journal of the American Statistical Association*, *99*(467), 673–686. https://doi.org/10.1198/016214504000000980
128. Wood, S. N. (2011). Fast stable restricted maximum likelihood and marginal likelihood estimation of semiparametric generalized linear models. *Journal of the Royal Statistical Society. Series B (Statistical Methodology)*, *73*(1), 3–36. JSTOR.
129. R Core Team (2013). R: A language and environment for statistical computing. R Foundation for statistical computing, Vienna, Austria. https://r-project.org
130. Larsen, B., Bourque, J., Moore, T. M., Adebimpe, A., Calkins, M. E., Elliott, M. A., Gur, R. C., Gur, R. E., Moberg, P. J., Roalf, D. R., Ruparel, K., Turetsky, B. I., Vandekar, S. N., Wolf, D. H., Shinohara, R. T., & Satterthwaite, T. D. (2020). Longitudinal Development of Brain Iron Is Linked to Cognition in Youth. *The Journal of Neuroscience: The Official Journal of the Society for Neuroscience*, *40*(9), 1810–1818. https://doi.org/10.1523/JNEUROSCI.2434-19.2020
131. Pines, A. R., Cieslak, M., Larsen, B., Baum, G. L., Cook, P. A., Adebimpe, A., Dávila, D. G., Elliott, M. A., Jirsaraie, R., Murtha, K., Oathes, D. J., Piiwaa, K., Rosen, A. F. G., Rush, S., Shinohara, R. T., Bassett, D. S., Roalf, D. R., & Satterthwaite, T. D. (2020). Leveraging multi-shell diffusion for studies of brain development in youth and young adulthood. *Developmental Cognitive Neuroscience*, *43*, 100788. https://doi.org/10.1016/j.dcn.2020.100788
132. Simpson, G. L. (2018). Modelling Palaeoecological Time Series Using Generalised Additive Models. *Frontiers in Ecology and Evolution*, *6*. https://doi.org/10.3389/fevo.2018.00149
133. Wood, S. N. (2006). Low-rank scale-invariant tensor product smooths for generalized additive mixed models. *Biometrics*, *62*(4), 1025–1036. https://doi.org/10.1111/j.1541-0420.2006.00574.x
134. Gur, R. C., Richard, J., Calkins, M. E., Chiavacci, R., Hansen, J. A., Bilker, W. B., Loughead, J., Connolly, J. J., Qiu, H., Mentch, F. D., Abou-Sleiman, P. M., Hakonarson, H., & Gur, R. E. (2012). Age group and sex differences in performance on a computerized neurocognitive battery in children age 8–21. *Neuropsychology*, *26*(2), 251–265. https://doi.org/10.1037/a0026712
135. Moore, T. M., Reise, S. P., Gur, R. E., Hakonarson, H., & Gur, R. C. (2015). Psychometric properties of the Penn Computerized Neurocognitive Battery. *Neuropsychology*, *29*(2), 235–246. https://doi.org/10.1037/neu0000093
136. Pedregosa, F., Varoquaux, G., Gramfort, A., Michel, V., Thirion, B., Grisel, O., Blondel, M., Prettenhofer, P., Weiss, R., Dubourg, V., Vanderplas, J., Passos, A., Cournapeau, D., Brucher, M., Perrot, M., & Duchesnay, É. (2011). Scikit-learn: Machine Learning in Python. *The Journal of Machine Learning Research*, *12*, 2825–2830.

## 1. Premise

Here, we overcome limitations by capitalizing upon a widely-used method in computer vision – optical flow – to quantify activity propagations across the cortex. Optical flow enabled us to derive *directional* information regarding propagations directly from changes in local BOLD signal (**methods**). In neuroscience, optical flow has been primarily implemented either on group-level patterns[13], or on small 2-D sections of cortex[15]. Recently, the optical flow algorithm was adapted to efficiently estimate biological motion on 3-dimesional spheres[16]. We leveraged this advance to quantify the movement of BOLD signal directly on each participant's cortex following spherical registration. We hypothesized that this approach would reveal bottom-up and top-down propagations across the cortex. Furthermore, we predicted that top-down propagations would be associated with task-demands and become more prominent with age in youth. To test these hypotheses, we leveraged a large developmental dataset with both high-quality resting-state and task fMRI data[15] ($n$ = 388 after QC, mean age = 15.6, $SD$ = 3.7 years).

## 2. Main text

Optical flow yielded vector fields describing the direction of signal propagation between fMRI volumes mapped to the cortical surface via spherical registration (**Figure 4.1a**). To evaluate the presence of hierarchical propagations, we extracted the gradient vector field (∇) of an established map that defines the principal gradient (PG) of the cortical hierarchy (∇PG, **Figure 4.1b**). Because gradient vector fields describe the direction of image intensity increases, ∇PG describes the direction of hierarchical ascent at each point on the cortex. Local ∇PG directions were subsequently utilized as reference directions for optical flow vectors for each participant (**Figure 4.1c**). After removing volumes corrupted by head motion, we recorded the difference in the angle (in degrees) of the direction of activity estimated by the optical flow vectors with respect to the direction of hierarchical ascent defined by the ∇PG **(Figure 4.1d)**. In this framework,

alignment with the angle of hierarchical ascent (0° from ∇PG) indicates a bottom-up propagation, whereas flow in the opposite direction (180° from ∇PG) indicates a top-down propagation (**Figure 4.1e**).

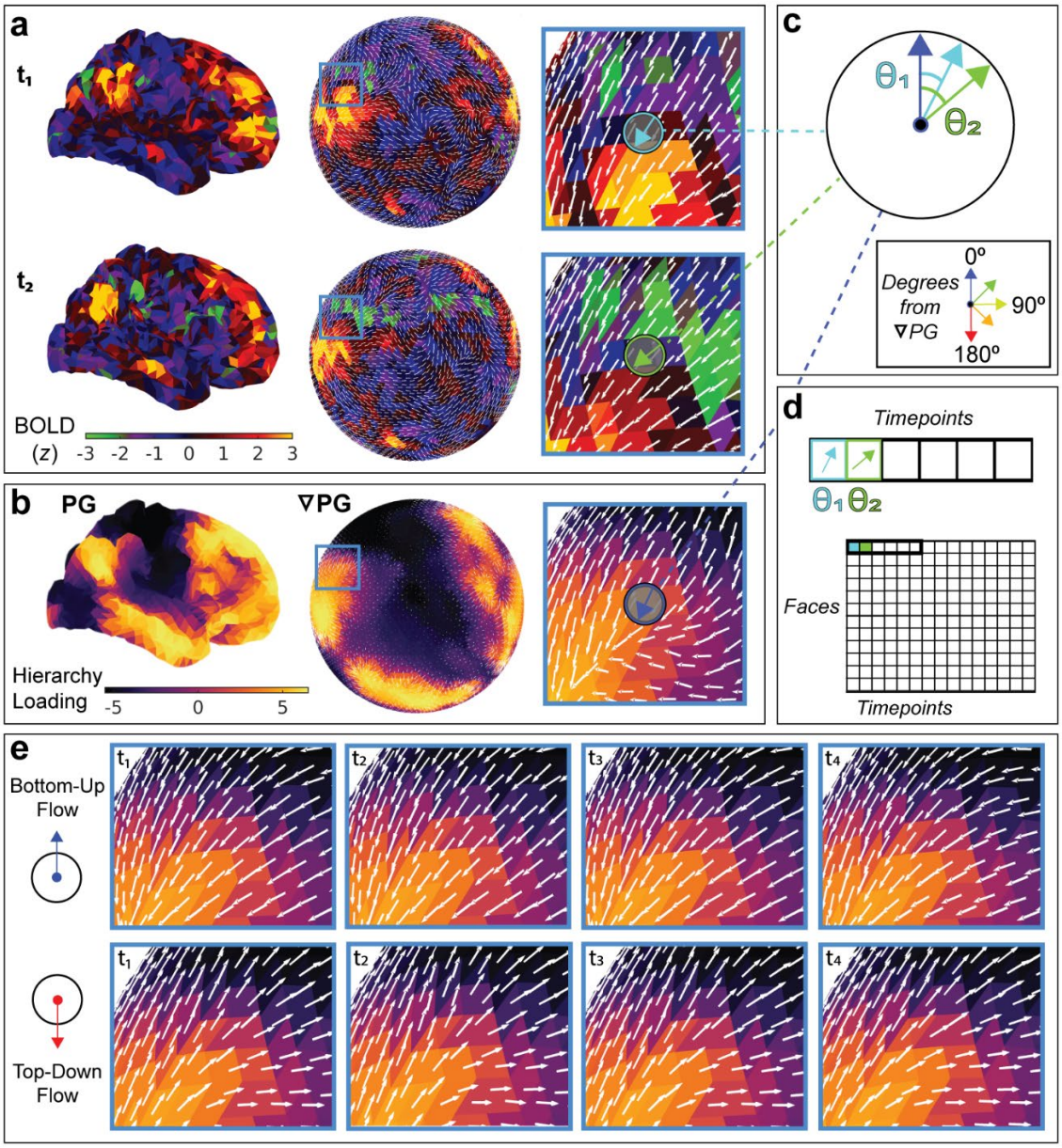


**Figure 4.1. Schematic for spherical optical flow and assessment of hierarchical propagations. a**) To estimate the spatial directionality of activity across the cortex, all fMR images are projected to the *fsaverage4* spherical surface. Specifically, for each pair of sequential images, we used optical flow to estimate the directions of signal propagations at each face on the cortical mesh. **b)** To estimate the direction of hierarchical ascent, the gradient vector field of a validated map of cortical hierarchy[10] was extracted along the cortical surface (∇PG). This

procedure yields vectors across the entire cortex, with each vector describing the most direct direction of hierarchical ascent for any given face on the mesh. **c)** To quantify directional distributions, each optical flow direction is assessed relative to the direction of hierarchical ascent face over all sequential image pairs. **d)** This procedure is repeated for each on the cortical mesh to yield a matrix of BOLD directions relative to ∇PG over time for each participant. **e)** Example bottom-up and top-down propagations: vectors were extracted from a pair of sequential BOLD images and overlaid onto the group-level PG.

We observed a predominance of both bottom-up and top-down propagations along the PG, which formed a bimodal distribution. Bimodal directional distributions were evident at the group (**Figure 4.2a**) and participant-level (**Figure 4.2b**). To rigorously test whether propagations were enriched for bottom-up and top-down directionality, we used a conservative spin-based permutation method that perseveres the spatial covariance structure of the data **(Figure 4.2c)**. This procedure revealed that the angular distributions of propagations were specifically aligned with ∇PG for every participant in the sample, far beyond what could be expected by chance. To further confirm that directions reflected true propagations rather than discrete, alternating activation of lower and higher-order cortices, we shuffled the fMRI volume ordering of each participant iteratively **(Figure 4.2d)**. These temporal permutation tests confirmed that optical flow captured specific sequences of activity that were not present in shuffled data.

Having demonstrated the presence of hierarchical propagations in all participants, we next sought to define the spatial distribution of bottom-up and top-down propagations. For each location on the cortex, we quantified the percentage of propagations that could be characterized as bottom-up or top-down (**methods**). While all regions exhibited a mix of both bottom-up and top-down propagations at different points in time, bottom-up propagations were most common in regions including the medial prefrontal cortex, while top-down propagations were most common in regions such as the dorsolateral prefrontal and anterior cingulate cortex (**Figure 4.2e**). At the participant-level, the percentage of top-down optical flow vectors was highly correlated with our statistical summary measure of non-unimodality (i.e., dip statistic, $r = .70$, $p < 0.01 \times 10^{-14}$). This measure allowed us to directly test whether top-down propagations became more common under task demands and with development in youth.

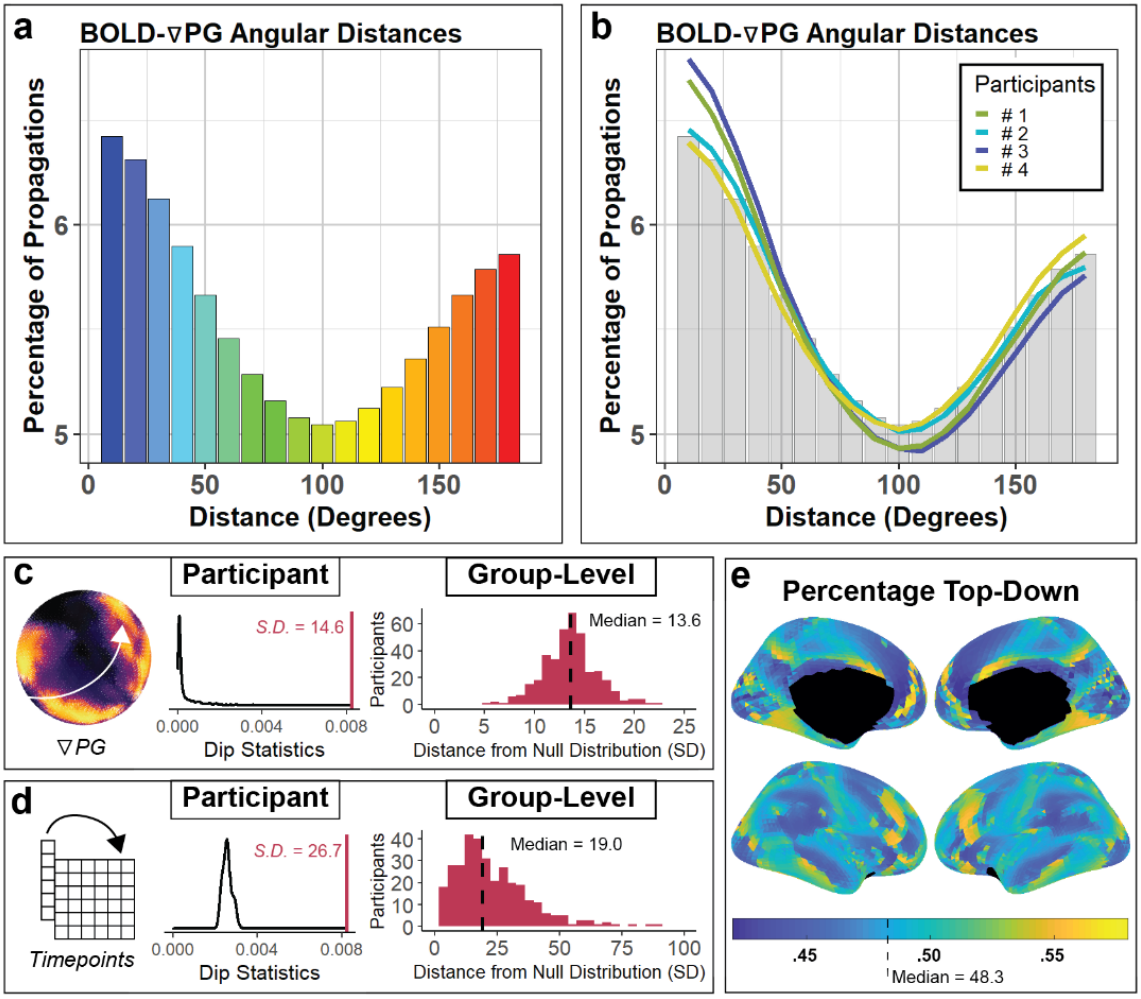
a
BOLD-∇PG Angular Distances
Percentage of Propagations
6
5
0
50
100
150
Distance (Degrees)
b
BOLD-∇PG Angular Distances
Participants
# 1
# 2
# 3
# 4
Percentage of Propagations
6
5
0
50
100
150
Distance (Degrees)
c
Participant
Group-Level
S.D. = 14.6
Median = 13.6
Participants
60
40
20
0
0.000
0.004
0.008
Dip Statistics
0
5
10
15
20
25
Distance from Null Distribution (SD)
∇PG
d
Participant
Group-Level
S.D. = 26.7
Median = 19.0
Participants
40
30
20
10
0
0.000
0.004
0.008
Dip Statistics
0
25
50
75
100
Distance from Null Distribution (SD)
Timepoints
e
Percentage Top-Down
.45
.50
.55
Median = 48.3

**Figure 4.2 . Cortical activity propagates up and down a normative hierarchy. a)** Group-level directional distributions revealed a bimodal distribution of angular distances between ∇PG and flow vectors ($n$ = 4.4 billion optical flow directions). **b)** Directional distributions are bimodal for hierarchical ascent (0°) and descent (180°) within individual participants. **c)** Spatial null models permuted the reference directions (∇PG) continuously in space, preserving the spatial covariance structure of the original map (left). Spatial null models are computed within participants (middle; participant #1 from **b**) by comparing the dip statistic obtained from permuted reference directions (black distribution) and the true dip statistic (red line). Whereas 1.96 standard deviations from the mean is the most common statistical threshold for significance, we found that true dip statistics tended to be roughly 13.6 standard deviations from the mean across participants (right). **d)** Temporal null models permuted the order of retained fMRI volumes in time, preserving complex spatial patterns found within individual images (left). Temporal null models were computed within participants (middle; participant #1 from **b**) by comparing the dip statistic obtained from permuted fMR ordering (black distribution) and the true dip statistic (red line). True dip statistics tended to be roughly 20.2 standard deviations from the mean across participants (right). **e)** All faces exhibited bottom-up (<90°) and top-down (>90°) propagations, but regions such as medial prefrontal cortex were enriched for bottom-up propagations. In contrast, regions including the dorsolateral prefrontal cortex and anterior cingulate cortex were enriched for top-down propagations.

Specifically, we sought to evaluate whether the prevalence of top-down propagations was modulated by cognitive tasks that require top-down cognitive control. We compared propagations during a modified Go/NoGo task, where top-down control is intermittently required to suppress reflexive button-pressing (Sommerville), to propagations observed during rest. Mass univariate analyses revealed more top-down propagations during task than rest ($t$ = 2.37-13.97, $p_{fdr}$ <0.05; **Figure 4.3a**). While these effects were distributed across the cortex, increases in top-down propagations were particularly prominent in regions within the dorsal and ventral attention networks.

Next, we evaluated whether the prevalence of top-down propagations was associated with age in youth. Mass univariate analyses revealed widespread increases in the proportion of top-down propagations observed with age across the cortex (Δ Adjusted $R^2$ = 0.01 - 0.19, $p_{fdr}$ <0.05**, Figure 4.3b**). These effects were particularly prominent in the dorsal and ventral streams, as well the premotor pathway. Surprisingly, age effects extended continuously beyond the canonical premotor pathway all the way into inferio-medial prefrontal cortex. These results suggest that maturation of internally-oriented default-mode regions may be directly linked to maturation of the internally-driven medial premotor pathway[16]. Although these regions exhibited

prominent age effects, we also found that the proportion of top-down propagations exhibited across the entire cortex increases with age (Δ Adjusted $R^2$ = 0.14, $p$ = 1.7x$10^{-14}$**, Figure 4.3c**).

Next, we sought to determine how development alters the full distribution of propagations directions rather than simply evaluating the change in proportion of top-down or bottom-up flow. To do so, we calculated the difference in the average angular distribution of propagations for the youngest ($n$ = 127, mean age = 11.49, $SD$ = 1.70 years) and oldest tertile ($n$ = 132, mean age = 19.76, $SD$ = 1.39 years) of the data (**Figure 4.3d**). We then evaluated the significance of this difference of distributions by comparing the true difference versus a null distribution created from random tertile splits (**Figure 4.3d,** gray band). We found that the angular distributions shift monotonically towards top-down propagations with age: maximally top-down propagations increased with age the most, whereas maximally bottom-up propagations showed the biggest declines with age.

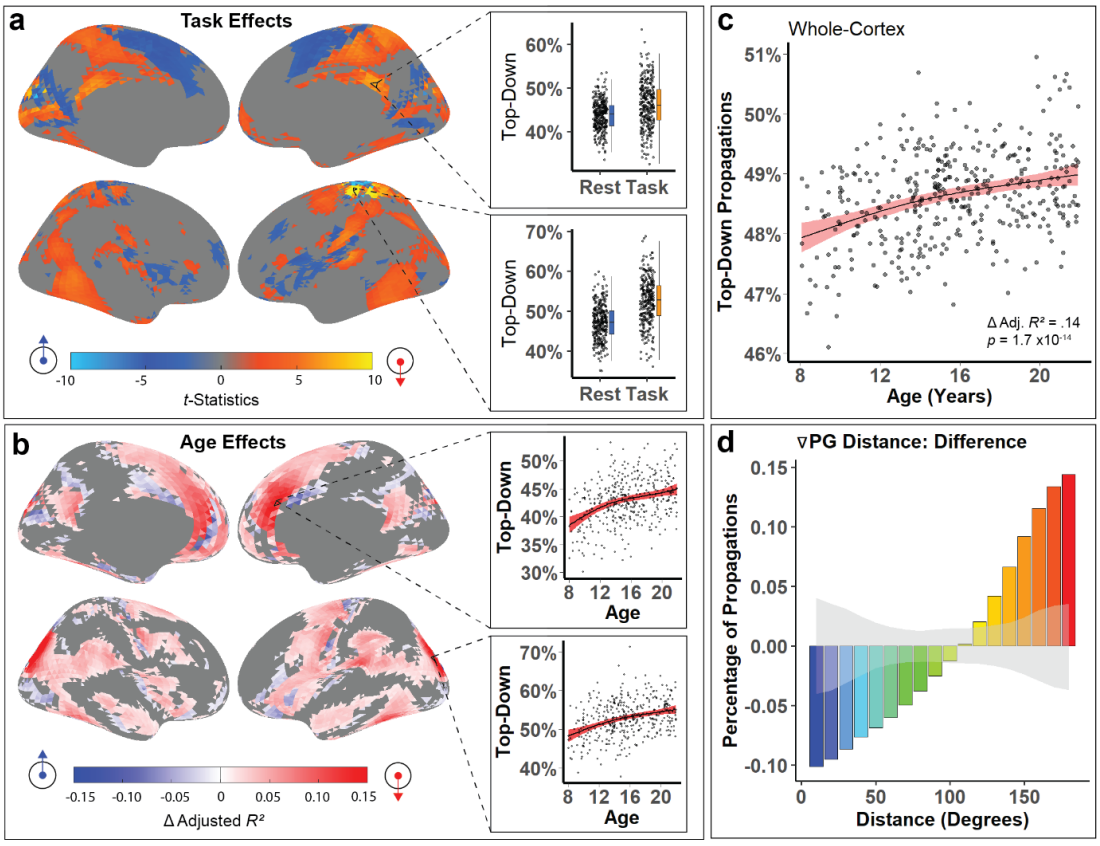

**Figure 4.3. The prevalence of top-down propagations are impacted by task-demands and develop with age. a)** Compared to rest, the demands of a cognitive control task elicit a shift in the proportion of propagations that are top-down ($Q_{FDR} < 0.05$, more top-down under task demands in orange). **b)** Adults exhibit more top-down propagations than children and adolescents across the brain, particularly in attention networks ($Q_{FDR} < 0.05$, more top-down with age in red). **c)** Whole-cortex-averaged top-down propagations increase with age. **d)** Whole-cortex directional distributions mature such that after adolescence, a greater percentage of propagations are top-down. This difference extends above and beyond distribution differences observed in 1,000 equally sized, randomly selected subgroups of participants (gray band = 95% confidence interval on bootstrap resamples).

Finally, we conducted sensitivity and specificity analyses to confirm our findings. Notably, the spatial distribution of the principal gradient is colinear with the distribution of functional networks[10], and the age effects we report occur over the same age range as developmental functional network segregation[6]. To ensure that our developmental results were not attributable to previously-reported functional network segregation, we quantified network segregation in all participants. While controlling for network segregation, increases in top-down propagations over development remained prominent ($\Delta$ Adjusted $R^2 = 0.14$, $p = 1.2 \times 10^{-14}$) and exhibited a stronger age-effect size than network segregation itself ($\Delta$ Adjusted $R^2 = 0.04$, $p = 3.1 \times 10^{-5}$). Finally, to verify that age effects were not attributable to scanning-site differences, we performed ComBat harmonization and repeated the above analyses. Developmental effects remained prominent when accounting for site differences ($\Delta$ Adjusted $R^2 = 0.12$, $p = 2.0 \times 10^{-12}$). Together, these sensitivity and specificity analyses confirmed that our findings were not attributable to previously documented properties of functional neurodevelopment or scanner differences.

## 3. Discussion

Several limitations should be noted. First, the cost function of optical flow is agnostic to the positivity of propagating signal: propagating *decreases* in BOLD signal are also captured by the resulting vector fields. Because propagating infraslow activations and deactivations can either facilitate or suppress gamma oscillations[12,13], explicitly disentangling activations from deactivations is an important step for future work. Second, motion-related signal artifact is likely to have a substantial impact on functional propagations. Consequently, we erred on the side of

being extremely stringent in quality assurance – using only low motion data and statistically controlling for residual motion artifact in all analyses.

These limitations notwithstanding, we developed an approach to quantify hierarchical how propagations align with the cortical hierarchy. This approach revealed that activity preferentially flows up and down the hierarchy. Given increases in top-down propagations in response to top-down task-demands, our work further suggests that such propagations are to some degree state-dependent. This observation coheres with initial evidence from Gu[12] and Munn[14], and further suggests that top-down processing may rely upon hierarchical cortical propagations. Finally, we found that top-down propagations become more prominent with age in youth. Our findings suggest that the *directionality* of propagating cortical activity may be broadly relevant for studies of hierarchical cortical organization and neurodevelopment, with potentially important applications for understanding psychopathology and neuromodulatory interventions.

## 4. Bibliography


1. Harris, J. A. *et al.* Hierarchical organization of cortical and thalamic connectivity. *Nature* **575**, 195–202 (2019).
2. Siegle, J. H. *et al.* Survey of spiking in the mouse visual system reveals functional hierarchy. *Nature* **592**, 86–92 (2021).
3. Felleman, D. J. & Van Essen, D. C. Distributed hierarchical processing in the primate cerebral cortex. *Cereb Cortex* **1**, 1–47 (1991).
4. Nenning, K.-H. *et al.* Joint embedding: A scalable alignment to compare individuals in a connectivity space. *NeuroImage* **222**, 117232 (2020).
5. Dong, H.-M., Margulies, D. S., Zuo, X.-N. & Holmes, A. J. Shifting gradients of macroscale cortical organization mark the transition from childhood to adolescence. *PNAS* **118**, (2021).
6. Pines, A. R. *et al.* Dissociable multi-scale patterns of development in personalized brain networks. *Nat Commun* **13**, 2647 (2022).
7. Shanmugan, S. *et al.* Common and Dissociable Mechanisms of Executive System Dysfunction Across Psychiatric Disorders in Youth. *AJP* **173**, 517–526 (2016).
8. Klassen, A. F., Miller, A. & Fine, S. Health-related quality of life in children and adolescents who have a diagnosis of attention-deficit/hyperactivity disorder. *Pediatrics* **114**, e541-547 (2004).
9. Casey, B. J., Jones, R. M. & Hare, T. A. The Adolescent Brain. *Ann N Y Acad Sci* **1124**, 111–126 (2008).

10. Margulies, D. S. *et al.* Situating the default-mode network along a principal gradient of macroscale cortical organization. *PNAS* **113**, 12574–12579 (2016).
11. Yousefi, B. & Keilholz, S. Propagating patterns of intrinsic activity along macroscale gradients coordinate functional connections across the whole brain. *NeuroImage* **231**, 117827 (2021).
12. Gu, Y. *et al.* Brain Activity Fluctuations Propagate as Waves Traversing the Cortical Hierarchy. *Cereb Cortex* (2021).
13. Raut, R. V. *et al.* Global waves synchronize the brain's functional systems with fluctuating arousal. *Sci Adv* **7**, eabf2709 (2021).
14. Munn, B. R., Müller, E. J., Wainstein, G. & Shine, J. M. The ascending arousal system shapes neural dynamics to mediate awareness of cognitive states. *Nat Commun* **12**, 6016 (2021).
15. Townsend, R. G. & Gong, P. Detection and analysis of spatiotemporal patterns in brain activity. *PLoS Comput Biol* **14**, e1006643 (2018).
16. Kirisits, C., Lang, L. F. & Scherzer, O. Decomposition of optical flow on the sphere. *Int J Geomath* **5**, 117–141 (2014).
17. Somerville, L. H. *et al.* The Lifespan Human Connectome Project in Development: A large-scale study of brain connectivity development in 5–21 year olds. *NeuroImage* **183**, 456–468 (2018).
18. Frey, S. H. *et al.* Neurological Principles and Rehabilitation of Action Disorders: Computation, Anatomy, and Physiology (CAP) Model. *Neurorehabil Neural Repair* **25**, 6S-20S (2011).

## 5. Methods

### *Sample*

To evaluate the maturation of cortical propagations, we used high-quality resting-state and task-fMRI data from the Human Connectome Project-Development 2.0 Release (HCP-D, $n$ = 652, mean age = 14.4, $SD$ = 4.1 years). Participants were scanned at four sites on 3 Tesla Siemens Prisma platforms. Structural scans consisted of high-resolution MPRAGE T1w images (0.8 $mm^3$, TR/TI=2,500,1000 ms, TE = 1.8/3.6/5.4/7.2 ms, flip angle = 8°) and a variable-flip-angle turbo-spin-echo T2w sequence (0.8 $mm^3$, TR/TI=3,200,564 ms, turbo factor = 314). Additionally, each subject underwent 26 minutes of resting-state scans across 4 runs, and 8 minutes of task-fMRI across 2 runs for our task of interest[17]. Multiband acceleration factors afforded sub-second temporal resolution for all functional images (2.0 $mm^3$, TR/TE = 800/37 ms, flip angle = 52°).

### *Image processing*

All images were processed with an updated version of the Human Connectome Project MRI pipeline[19,20.] Specifically, all structural images underwent gradient distortion correction, bias field correction, boundary-based registration, and normalization. Functional images underwent gradient distortion correction, re-alignment, EPI image distortion correction, boundary-based registration, and normalization prior to being projected to the cortical surface and smoothed with a 2mm FWHM gaussian kernel. Next, functional images were demeaned and de-trended using nuisance regressors. Finally, functional images were band-pass filtered between 0.008 and 0.09 Hz with a 2$^{nd}$ order Butterworth filter. Framewise displacement was calculated after accounting for the influence of respiratory signal on framewise image realignment. Noteworthy changes from the HCP pipeline included usage of Advanced Normalization Tools (ANTs) for denoising, bias field correction, and diffeomorphic symmetric image normalization, which was selected due to consistently higher registration performance over previous methods[21]. Finally, all images were downsampled to *fsaverage4* with connectome workbench for computational feasibility.

*Quality assurance*

In order to be included in analyses, participants needed to have at least 600 TRs surviving three quality-control thresholds. First frames were excluded if head motion exceeded 0.2 mm framewise displacement for that frame. Second, frames were excluded if they were contained DVARS values that were > 3 standard deviations above the mean. Third, because we were interested in propagations across TRs rather than patterns within single, low-motion TRs, we excluded otherwise low-motion segments that were interrupted by moderate to high-motion frames. Specifically, if sequential TRs did not meet the first two criteria for at least 10 consecutive TRs, the entire sequence was discarded. 388 participants (mean age = 15.7, *SD* = 3.4 years) met the > 600 TR requirement after the aforementioned quality assurance procedures.

*Cognitive control task*

For task-fMRI, we selected the Carit task *a priori* because it requires top-down cognitive control. The Carit task is a modified Go/No-Go task, where participants are instructed to make repeated button-presses in response to rapid, consistent stimuli, which are periodically interrupted. At the time of this interruption, the participant is to withhold a button press, probing their ability to suppress their button-pressing response. Because fewer scans were allocated to this task within HCP-D, we relaxed the minimum TR requirement to 300 TRs for task analyses only. As we compared propagations between task and resting conditions on a within-subject basis, only participants who passed both resting-state quality control (600 remaining TRs) and task QC (300 TRs) were included for these analyses.

*Optical flow*

Optical flow is a computer vision technique used to estimate the motion of signal intensity between successive images[22]. Like image registration, this procedure optimizes the deformation field that best explains the spatial discrepancy of signal intensity between two images. However, optical flow has been primarily implemented either at the group-level[13], or on small 2-D sections of cortex[15]. Recently, the optical flow algorithm was adapted to efficiently estimate biological motion on 3-dimesional spheres[16]. We leveraged this advance to quantify the movement of BOLD signal directly on each participant's cortex following spherical registration. As 2-dimensional "patch" projections of the cortex incur large discontinuities between spatially adjacent cortices, use of the spherical implementation of optical flow allowed us to efficiently analyze propagations across the cortex.

*∇PG*

In order to estimate directions of hierarchical ascent and descent, we extracted the gradient vector field (∇) of an established map that defines the principal gradient (PG) of the cortical hierarchy (∇PG). This approach is analogous to that taken in Tian et al. (2021)[23], but extracted across the cortical mantle rather than in subcortical volumetric space.

*Quantification of angular distances*

Our primary metric of interest was the angle (in degrees) between hierarchical vectors and optical flow vectors. To derive these, the 3-dimensional cartesian (x,y,z) vectors describing both vector fields were converted to a spherical coordinate system (azimuth, elevation, rho) via *cart2sphvec* in Matlab. Because signal travels across the sphere rather than into or away from it, this conversion obviates the third coordinate (rho). Consequently, we retained azimuth and elevation only for each hierarchical and optical flow vector, which describe directionality on a 2-D tangent-plane at each cortical face **(Figure 4.1c)**. From this point, angular distance was computed as the difference in directional orientation in degrees between ∇PG and optical flow, with 0 degrees indicating perfect alignment and 180 degrees indicating the maximum possible difference.

*Assessment of alignment between ∇PG and null models*

In order to test whether hierarchical ascent and descent were both directional modes in the distribution of optical flow vectors, we employed Hartigan's dip test. Specifically, we used the dip statistic to quantify the deviance of angular distributions from a unimodal distribution: a higher dip stat indicates that a distribution is more likely bimodal. Subsequently, we compared this measure to dip statistics derived from spatial and temporal null models.

For spatial null models, optical flow angular distances were calculated relative to a spatially permuted ∇PG. By "spinning" the entire ∇PG continuously in space, local spatial properties of the original map are conserved. Consequently, this procedure yields a more realistic and conservative spatial null model than random permutations where the spatial covariance structure is lost. We performed 1,000 permutations, and 1,000 corresponding null dip statistics were obtained for each participant. Finally, to extract a metric comparable across participants, we recorded the number of standard deviations between the true observed dip statistic and the mean of the 1,000 permutations.

For temporal null models, optical flow itself was re-calculated on temporally permuted data. Specifically, the temporal sequence of fMRI volumes surviving QC was shuffled iteratively for each participant. Because fitting optical flow to a pair of frames is computationally intensive (equivalent to a co-registration), we were limited to 100 temporal permutations per subject (613,000-1,883,000 optical flow decompositions per subject). This process yielded 100 sets of optical flow vectors for shuffled data, which were then subjected to the same angular distance calculation (relative to ∇PG), and 100 null dip statistics were subsequently obtained from these distributions. As for the spatial permutation tests, we compared true vs. permuted dip statistics as a single participant-level standard deviation.

*Analysis of the impact of task demands*

To test our hypotheses regarding shifts in top-down propagation prominence with task, we quantified the proportion of propagations that descended the cortical hierarchy. To do so, we calculated the proportion of optical flow vectors that indicated descent in any capacity (i.e., greater than 90 degrees from ∇PG) versus optical flow vectors that indicated hierarchical ascent (i.e., less than 90 degrees from ∇PG). This provided a measure of the prevalence of top-down propagations at each cortical face for each participant.

We compared the proportion of top-down propagations during rest and under the cognitive control demands of the Carit Task. Specifically, we conducted a paired t-test on the proportion of top-down propagations at each cortical face. This provided a t-statistic quantifying the degree to which faces exhibited more top-down propagations with task relative to rest. Multiple comparisons were controlled for with the false-discovery-rate (FDR: $q < 0.05$); only statistics that remained significant after correction for multiple comparisons were retained and reported.

*Analysis of developmental effects*

Developmental effects were estimated using generalized additive models[24] (GAMs) with penalized splines in R (Version 3.6.3) using the *mgcv* package. To avoid over-fitting, nonlinearity

was penalized using restricted maximum likelihood (REML)[25]. Participant sex, in-scanner head motion, and the number of frames passing quality assurance were included as covariates within each GAM. To quantify the effect sizes of each age spline, we calculated the change in adjusted $R^2$ ($\Delta R^2_{adj.}$) between the full model and a nested model that did not include an effect of age. Statistical significance was assessed using analysis of variance (ANOVA) to compare the full and nested models. As above, multiple comparisons were controlled for with the false-discovery-rate ($q < 0.05$). Finally, because $\Delta R^2_{adj.}$ describes effect size but not direction (i.e., increasing or decreasing top-down propagations with age), as in prior work[6], we extracted and applied the sign of the age coefficient from an equivalent linear model.

To quantify developmental differences in the full distributions of angular distances from ∇PG, we compared the oldest and youngest tertiles of all participants. Specifically, we reduced each participants angular distribution to 18 bins, with each bin comprising a 10-degree span from 0-180 degrees from ∇PG. Because each bin represents the percentage of total propagations that fall within their respective degree spans, the average of these values across participants represents the average percentage of total propagations each bin encompasses for each age tertile. Next, we subtracted the resultant value of each bin in the younger tertile from the resultant values in the older tertile. This provided a description of the difference in angular distributions between older and younger participants. However, that difference measure does not provide a statistical test of whether the difference is significant. To demonstrate statistically significant age effects, we performed a bootstrap procedure, where tertile splits were determined randomly. We repeated the difference-of-distributions procedure described above for 1,000 random tertile splits, producing 1,000 random differences of distributions. Finally, we extracted the 95% confidence interval from these 1,000 distribution differences to obtain an estimate of distribution differences that could be expected by chance alone. Observed differences exceeding this confidence interval were interpreted as true group differences, exceeding those expected by selecting two groups of the same size when the age distribution was random.

*Sensitivity Analyses*

We used sensitivity analyses to confirm that our results were not due to confounding factors. First, to ensure that hierarchical development of cortical propagations is not explained by hierarchical development of cortico-functional networks, we repeated our analyses while controlling for developmental network segregation. To do so, we constructed group-consensus atlas for the participants in our study with spatially regularized non-negative matrix factorization. Next, based on our prior work, we identified which of the delineated networks are those most likely to exhibit developmental segregation. Previously, we have detailed that the functional networks undergoing the most dramatic developmental segregation are those lying at the top of the cortical hierarchy[6], and other publications have similarly suggested that default-mode networks undergo developmental segregation[26,27]. Accordingly, we evaluated each network for its hierarchical position and overlap with canonical functional networks, and selected the single network fulfilling both *a priori* criteria (high in hierarchy and overlapping with canonical default mode). Next, we calculated a commonly-used measure of network segregation versus integration: the mean between-network coupling of this default-mode network with all other networks. We included this value as a model covariate in sensitivity analyses.

Finally, to ensure that the association between top-down propagations and age were not attributable to site effects, we harmonized top-down propagations across sites with ComBat[28,29]. This provided a site-harmonized measure of the proportion of top-down propagations exhibited by each participant, which we then tested in the same GAM framework.

**Bibliography**

1. Harris, J. A. *et al.* Hierarchical organization of cortical and thalamic connectivity. *Nature* **575**, 195–202 (2019).
2. Siegle, J. H. *et al.* Survey of spiking in the mouse visual system reveals functional hierarchy. *Nature* **592**, 86–92 (2021).
3. Felleman, D. J. & Van Essen, D. C. Distributed hierarchical processing in the primate cerebral cortex. *Cereb Cortex* **1**, 1–47 (1991).
4. Nenning, K.-H. *et al.* Joint embedding: A scalable alignment to compare individuals in a connectivity space. *NeuroImage* **222**, 117232 (2020).

5. Dong, H.-M., Margulies, D. S., Zuo, X.-N. & Holmes, A. J. Shifting gradients of macroscale cortical organization mark the transition from childhood to adolescence. *PNAS* **118**, (2021).
6. Pines, A. R. *et al.* Dissociable multi-scale patterns of development in personalized brain networks. *Nat Commun* **13**, 2647 (2022).
7. Shanmugan, S. *et al.* Common and Dissociable Mechanisms of Executive System Dysfunction Across Psychiatric Disorders in Youth. *AJP* **173**, 517–526 (2016).
8. Klassen, A. F., Miller, A. & Fine, S. Health-related quality of life in children and adolescents who have a diagnosis of attention-deficit/hyperactivity disorder. *Pediatrics* **114**, e541-547 (2004).
9. Casey, B. J., Jones, R. M. & Hare, T. A. The Adolescent Brain. *Ann N Y Acad Sci* **1124**, 111–126 (2008).
10. Margulies, D. S. *et al.* Situating the default-mode network along a principal gradient of macroscale cortical organization. *PNAS* **113**, 12574–12579 (2016).
11. Yousefi, B. & Keilholz, S. Propagating patterns of intrinsic activity along macroscale gradients coordinate functional connections across the whole brain. *NeuroImage* **231**, 117827 (2021).
12. Gu, Y. *et al.* Brain Activity Fluctuations Propagate as Waves Traversing the Cortical Hierarchy. *Cereb Cortex* (2021).
13. Raut, R. V. *et al.* Global waves synchronize the brain's functional systems with fluctuating arousal. *Sci Adv* **7**, eabf2709 (2021).
14. Munn, B. R., Müller, E. J., Wainstein, G. & Shine, J. M. The ascending arousal system shapes neural dynamics to mediate awareness of cognitive states. *Nat Commun* **12**, 6016 (2021).
15. Townsend, R. G. & Gong, P. Detection and analysis of spatiotemporal patterns in brain activity. *PLoS Comput Biol* **14**, e1006643 (2018).
16. Kirisits, C., Lang, L. F. & Scherzer, O. Decomposition of optical flow on the sphere. *Int J Geomath* **5**, 117–141 (2014).
17. Somerville, L. H. *et al.* The Lifespan Human Connectome Project in Development: A large-scale study of brain connectivity development in 5–21 year olds. *NeuroImage* **183**, 456–468 (2018).
18. Frey, S. H. *et al.* Neurological Principles and Rehabilitation of Action Disorders: Computation, Anatomy, and Physiology (CAP) Model. *Neurorehabil Neural Repair* **25**, 6S-20S (2011).
19. Glasser, M. F. *et al.* The minimal preprocessing pipelines for the Human Connectome Project. *Neuroimage* **80**, 105–124 (2013).
20. Earl, E., Perrone, A., Feczko, E., and Fair, D. (2020a). ABCD-BIDS pipeline (OSF).
21. Ou, Y., Akbari, H., Bilello, M., Da, X. & Davatzikos, C. Comparative Evaluation of Registration Algorithms in Different Brain Databases With Varying Difficulty: Results and Insights. *IEEE Transactions on Medical Imaging* **33**, 2039–2065 (2014).
22. Horn, B. K. P. & Schunck, B. G. Determining optical flow. *Artificial Intelligence* **17**, 185–203 (1981).
23. Tian, Y., Margulies, D. S., Breakspear, M. & Zalesky, A. Topographic organization of the human subcortex unveiled with functional connectivity gradients. *Nat Neurosci* **23**, 1421–1432 (2020).
24. Wood, S. N. Stable and Efficient Multiple Smoothing Parameter Estimation for Generalized Additive Models. *Journal of the American Statistical Association* **99**, 673–686 (2004).
25. Wood, S. N. Fast stable restricted maximum likelihood and marginal likelihood estimation of semiparametric generalized linear models. *Journal of the Royal Statistical Society. Series B (Statistical Methodology)* **73**, 3–36 (2011).
26. Jones, J. S., Team, T. C. & Astle, D. E. Segregation and integration of the functional connectome in neurodevelopmentally 'at risk' children. *Developmental Science* **25**, e13209 (2022).
27. Grayson, D. S. & Fair, D. A. Development of large-scale functional networks from birth to adulthood: A guide to the neuroimaging literature. *NeuroImage* **160**, 15–31 (2017).
28. Johnson, W. E., Li, C. & Rabinovic, A. Adjusting batch effects in microarray expression data using empirical Bayes methods. *Biostatistics* **8**, 118–127 (2007).
29. Fortin, J.-P. *et al.* Harmonization of cortical thickness measurements across scanners and sites. *NeuroImage* **167**, 104–120 (2018).

# CHAPTER 5: FUTURE DIRECTIONS

We've observed overlapping layers of neurodevelopment across magnetic resonance radiofrequency weightings, across spatial scales of cortico-functional networks, and across movements of activity unbounded by spatial discretization. Immediate future directions for multi-shell diffusion to study neurodevelopment might be as simple as including a greater diversity of neuroimaging data into models of microstructure. Just as we found that assaying across diffusion weightings yielded a richer characterization of microstructural maturation, it follows that incorporating greater *b*-values (i.e., *b*=3-6,000) and other structural signals (i.e., T2*, diffusion weighted spectroscopy) would yield an even richer characterization of neurodevelopment (De Marco et al., 2022; Fick et al., 2016). Similarly, immediate future directions for multi-scale functional network development might be as simple as expanding the range of spatial scales studied. High resolution 7-Tesla imaging might provide an avenue to delineate finer-grained functional covariance, and even to discern layers of functional organization across layers of cortex (Yang et al., 2021). The development of top-down propagations invokes the most future directions. Only the most basic within-individual variability has been assessed here (task-dependencies), only the most MRI-salient between-individual differences have been assessed (age), and only the most intuitive aspects of hierarchical directionality have been quantified (>90 degrees from bottom-up vs. < 90 degrees). Undoubtedly more nuanced task-assessment will provide greater insight into the role of propagations in cortical processes, analyses of health and disease-states will provide greater insight into how the cortex matches the mentation of the individual, and delineating the structures of cortical propagations will provide greater insight into the composition of the sea of cortical waves.

In turn, we might expect that greater nuance of microstructural, network, and propagation organization over development might yield a sharpened picture of normative neurodevelopment, or even inform normative brain organization. One advantage of this gained clarity is that with a

sharper image of normativity might come diagnostics of deviance. Advancements in individualized treatments do suggest increasing public health utility in increasingly specific clinical characterizations and interventions (Cole et al., 2020; Drysdale et al., 2017; Goldstein-Piekarski et al., 2016).

In contrast, tailoring neurodevelopment for utilitarian good might not require such precision. Broadly applicable tenants of healthy neurodevelopment are amenable to broad strokes of intervention. Dissimilar children are still likely to all benefit from increased support and resilience (Brody et al., 2017; Callaghan & Tottenham, 2016; Tooley et al., 2021).

Promisingly, universal tenants of normative development are being increasingly established. Height goes up with age for almost everyone. Weight goes up with age for almost everyone. Cortical volume and surface area goes up with age, as does the differentiation between gray and white matter (Bethlehem et al., 2022). As for cortical function, alignment with a normative hierarchy increases with age, (Nenning et al., 2020; Pines et al., 2022a), as does the propensity for local field potentials to traverse from the top of this hierarchy downwards (Pines et al., 2022b). If we are seeking to integrate these functional patterns, we might cling to this normative hierarchy as a foundation floating in an otherwise dark ocean. But summarizing is just half of understanding, digging deeper reveals higher dimensional multi-causality just beneath the surface. Delegating roles of causal creator and caused creation to hierarchy and brain function is difficult. Perhaps functional neurodevelopment hails from structural neurodevelopment (Pines et al., 2020), or both cause each other. Perhaps neurodevelopmental network reorganization proceeds coarsely before proceeding granularly (Busch et al., 2022), or perhaps multiple scales of network organization proceed in their neurodevelopmental adaptation contemporaneously (Pines et al., 2022a). Brain organization potentially being both emergent from and governing of neurodevelopment runs counter but not orthogonal to causality as a semantic framework. At the very least, the multicausality of neurodevelopment highlights that the transitive-property-causal framework that has worked so well for math and physics encounters substantial limitations understanding multiplex multicausal socio-biological systems.

Consideration of the environment in which brains maturate further complicates our attempts to reduce neurodevelopment to normativity. Disruptions to normative development can occur both within and across generations (Subica & Link, 2022), the brain and the environment are both causal agents upon each other (Cuvier, 1817; Lamarck, 1802), and brain-environment interactions are highly complex multivariate patterns (Murtha et al., 2021). Ironically, given that the extreme protraction of human development appears to underlie our highest-order cognition (Giedd & Rapoport, 2010), we might need further protraction of our neurodevelopment to fully understand it.

Delineating the complexities of neurodevelopment will likely necessitate novel approaches, if for no other reason than the complex interplay between the brain and environment. Whereas classical causality might be adequate for progressing chemistry or even neurology, the chances of delineating every causal agent in the development of the brain and environment is functionally zero. Further, causal chains presumes that each "agent" is truly a discrete construct, which does not hold water for excitatory tone, oxidative stress, metabolic efficiency, functional and structural connections in the brain, nor security, socioeconomic status, and environmental enrichment in the environment. Two alternative approaches, perhaps not themselves fully distinct from each other, might lend themselves to illuminating the water peripheral to our foundations.

First, the native language of the brain and behavior increasingly appears to be multivariate. The neuroscientific questions that are answered by one "neurotransmitter deficit", one region, or one circuit, are limited, particularly among observations noted only at one scale and/or one point in time. Minute facial movements in simple mammals invoke specific responses from at least thousands of neurons (Stringer et al., 2019), individual differences in psychopathology are captured by multidimensional brain-wide spatial patterns of functional covariance (Cui et al., 2022), and spatial variance in sets of genes might serve to differentiate subcortical territories rather than just individual genes (Vogel et al., 2020). Accounting for these relations with explicitly multivariate approaches might be one modest step towards pushing the bounds of our conception of neurodevelopment and the development of individual differences.

Second, considering the direction of an individual might bring us closer to characterizing them than considering their cross-sectional location. Just as measuring individual differences in the distance of a long jump might be rendered useless if individuals had different staring points from which to leap, we might expect that the dramatic variability in the origins of lives might confuse our evaluations of higher-order properties of the individual. We might find that analyzing the *directional profile* of an individual would better serve as a common foundation than the concept of development. Where are they, given their starting point? Although countless generations of brain and environmental differences accrue to yield the starting point for any organism, the movement of the organism from that point is more ascribable to a unitary being. Undoubtedly the individual has more autonomy over their relative distance covered rather than absolute, suggesting that the latter would be more informative to the nature of the individual. Concretely, such quantifications of individual movements might emerge from longitudinal data, in the form of change between timepoints, or participant-specific random effect slopes. In combination with the first proposed method of advancing our conceptions of neurodevelopment, multivariate profiles of change between timepoints might serve as key (if complex) indices of the individual. Either in tandem with multivariatism or on its own, considering the change of the individual might provide another modest increase in our conceptualization of neurodevelopment, and the development of individual differences.

To zoom out, If we return to our analogy of the biomedical sciences approximating a campaign of combating complexity, we appreciate what role such quantifications might play. If we permit ourselves a multi-scale view, we discover that just as cortical propagations are not bound to discrete regions, our efforts as scientists are not circumscribed within the domain of science:

> *"[Philosophy] is the front trench in the siege of truth. Science is the captured territory, and behind it are those secure regions in which knowledge and art build our imperfect and marvelous world."* (Durant, 1926).

We find this progression in truths regarding the relationship between the organism and environment, a relationship first put to the microscope by philosopher Herbert Spencer in the 19th century (among English-speakers, Pearce, 2010; Taylan, 2022). After the front trench was able to

conceptualize this relationship, we've been able to secure prospective truths within its territory (Callaghan & Tottenham, 2016; Murtha et al., 2021; Tooley et al., 2021), and in turn hope this knowledge might be appropriately reflected in our world (Brody et al., 2017). It follows that to consider the future directions of our science, those beyond our next paper or grant, we might consider the territories of conception thinkers of the recent past have annexed. Temporally equidistant between the writer of this dissertation and Laplace, Alfred Adler also postulated the organization of individual mentation exhibited its form *across* time, namely in its movement over time:

> *"We attribute a soul only to moving, living organisms. The soul stands in innate relationship to free motion…There is a strict corollary between movement and psychic life"* (Adler, 1927).

Adler might find modern support for his postulation of organization *over* time being critical to the individual (Betzel & Bassett, 2017; Buzsáki & Draguhn, 2004). Further, the process by which Adler described that we might make sense of the individual, to record "many movements of an individual" as points over time, and to search for expression of their psychic life specifically in the connections between these points, is now considered the gold standard for understanding development (Adler, 1927; Casey et al., 2018). Indeed, to dissect the system for investigation, we must make our cut somewhere. Let us make our cross-section in time, so that we might consider and control for temporal location from which the participant travels, and delineate the direction in which they move. Although this approach incurs assumptions of its own (i.e., non-relativity of time between measurements between individuals), we might at the very least further our characterization of the form of individual differences, and the development of these individual differences.

Undoubtedly multiple layers of lifespan development intersect with directions of the self: a mid-life parent will not hesitate to sacrifice themselves for an early-life child. If we can adequately ascribe variability-by-age and variability-by-individual, perhaps we might identify directionality as a key individual difference to bridge the foundations of development and the individual (Pines et al., 2022b).

References

Adler, A. (1927). *Understanding human nature* (pp. xiii, 286). Greenberg.

Antón-Bolaños, N., Sempere-Ferràndez, A., Guillamón-Vivancos, T., Martini, F. J., Pérez-Saiz, L., Gezelius, H., Filipchuk, A., Valdeolmillos, M., & López-Bendito, G. (2019). Prenatal activity from thalamic neurons governs the emergence of functional cortical maps in mice. *Science*, *364*(6444), 987–990. https://doi.org/10.1126/science.aav7617

Bath, K. G., Manzano-Nieves, G., & Goodwill, H. (2016). Early life stress accelerates behavioral and neural maturation of the hippocampus in male mice. *Hormones and Behavior*, *82*, 64–71. https://doi.org/10.1016/j.yhbeh.2016.04.010

Bavelier, D., Levi, D. M., Li, R. W., Dan, Y., & Hensch, T. K. (2010). Removing brakes on adult brain plasticity: From molecular to behavioral interventions. *The Journal of Neuroscience: The Official Journal of the Society for Neuroscience*, *30*(45), 14964–14971. https://doi.org/10.1523/JNEUROSCI.4812-10.2010

Berwick, R. C., & Chomsky, N. (2016). *Why Only Us: Language and Evolution*. MIT Press.

Bethlehem, R. a. I., Seidlitz, J., White, S. R., Vogel, J. W., Anderson, K. M., Adamson, C., Adler, S., Alexopoulos, G. S., Anagnostou, E., Areces-Gonzalez, A., Astle, D. E., Auyeung, B., Ayub, M., Bae, J., Ball, G., Baron-Cohen, S., Beare, R., Bedford, S. A., Benegal, V., … Alexander-Bloch, A. F. (2022). Brain charts for the human lifespan. *Nature*, *604*(7906), 525–533. https://doi.org/10.1038/s41586-022-04554-y

Betzel, R. F., & Bassett, D. S. (2017). Multi-scale brain networks. *NeuroImage*, *160*, 73–83. https://doi.org/10.1016/j.neuroimage.2016.11.006

Bihan, D. L. (2007). The `wet mind': Water and functional neuroimaging. *Physics in Medicine and Biology*, *52*(7), R57–R90. https://doi.org/10.1088/0031-9155/52/7/R02

Blinder, P., Tsai, P. S., Kaufhold, J. P., Knutsen, P. M., Suhl, H., & Kleinfeld, D. (2013). The cortical angiome: An interconnected vascular network with noncolumnar patterns of blood flow. *Nature Neuroscience*, *16*(7), 889–897. https://doi.org/10.1038/nn.3426

Braun, U., Schaefer, A., Betzel, R. F., Tost, H., Meyer-Lindenberg, A., & Bassett, D. S. (2018). From Maps to Multi-dimensional Network Mechanisms of Mental Disorders. *Neuron*, *97*(1), 14–31. https://doi.org/10.1016/j.neuron.2017.11.007

Breakspear, M., & Stam, C. J. (2005). Dynamics of a neural system with a multiscale architecture. *Philosophical Transactions of the Royal Society B: Biological Sciences*, *360*(1457), 1051–1074. https://doi.org/10.1098/rstb.2005.1643

Brinkmann, L., Gezerli, D., Kleist, K. V., Müller, T. F., Rahwan, I., & Pescetelli, N. (2022). Hybrid social learning in human-algorithm cultural transmission. *Philosophical Transactions. Series A, Mathematical, Physical, and Engineering Sciences*, *380*(2227), 20200426. https://doi.org/10.1098/rsta.2020.0426

Brody, G. H., Gray, J. C., Yu, T., Barton, A. W., Beach, S. R. H., Galván, A., MacKillop, J., Windle, M., Chen, E., Miller, G. E., & Sweet, L. H. (2017). Protective Prevention Effects on the Association of Poverty With Brain Development. *JAMA Pediatrics*, *171*(1), 46–52. https://doi.org/10.1001/jamapediatrics.2016.2988

Buckner, R. L., & Krienen, F. M. (2013). The evolution of distributed association networks in the human brain. *Trends in Cognitive Sciences*, *17*(12), 648–665. https://doi.org/10.1016/j.tics.2013.09.017

Budget of NASA. (2022). In *Wikipedia*. https://en.wikipedia.org/w/index.php?title=Budget_of_NASA&oldid=1079068475

Busch, E. L., Rapuano, K. M., Anderson, K., Rosenberg, M. D., Watts, R., Casey, B., Haxby, J., & Feilong, M. (2022). *The LEGO theory of the developing functional connectome* [Preprint]. Neuroscience. https://doi.org/10.1101/2022.05.24.493295

Buzsáki, G., & Draguhn, A. (2004). Neuronal oscillations in cortical networks. *Science (New York, N.Y.)*, *304*(5679), 1926–1929. https://doi.org/10.1126/science.1099745

Cadwell, C. R., Bhaduri, A., Mostajo-Radji, M. A., Keefe, M. G., & Nowakowski, T. J. (2019). Development and Arealization of the Cerebral Cortex. *Neuron*, *103*(6), 980–1004. https://doi.org/10.1016/j.neuron.2019.07.009

Callaghan, B. L., & Tottenham, N. (2016). The Stress Acceleration Hypothesis: Effects of early-life adversity on emotion circuits and behavior. *Current Opinion in Behavioral Sciences*, *7*, 76–81. https://doi.org/10.1016/j.cobeha.2015.11.018

Casey, B. J., Cannonier, T., Conley, M. I., Cohen, A. O., Barch, D. M., Heitzeg, M. M., Soules, M. E., Teslovich, T., Dellarco, D. V., Garavan, H., Orr, C. A., Wager, T. D., Banich, M. T., Speer, N. K., Sutherland, M. T., Riedel, M. C., Dick, A. S., Bjork, J. M., Thomas, K. M., … Dale, A. M. (2018). The Adolescent Brain Cognitive Development (ABCD) study: Imaging acquisition across 21 sites. *Developmental Cognitive Neuroscience*, *32*, 43–54. https://doi.org/10.1016/j.dcn.2018.03.001

Casey, B., Jones, R. M., & Somerville, L. H. (2011). Braking and Accelerating of the Adolescent Brain. *Journal of Research on Adolescence : The Official Journal of the Society for Research on Adolescence*, *21*(1), 21–33. https://doi.org/10.1111/j.1532-7795.2010.00712.x

Casselman, B. (2007). *All for Nought*. American Mathematical Society. https://www.ams.org/publicoutreach/feature-column/fcarc-india-zero

Chang, Y. S., Owen, J. P., Pojman, N. J., Thieu, T., Bukshpun, P., Wakahiro, M. L. J., Berman, J. I., Roberts, T. P. L., Nagarajan, S. S., Sherr, E. H., & Mukherjee, P. (2015). White Matter Changes of Neurite Density and Fiber Orientation Dispersion during Human Brain Maturation. *PLOS ONE*, *10*(6), e0123656. https://doi.org/10.1371/journal.pone.0123656

Cole, E. J., Stimpson, K. H., Bentzley, B. S., Gulser, M., Cherian, K., Tischler, C., Nejad, R., Pankow, H., Choi, E., Aaron, H., Espil, F. M., Pannu, J., Xiao, X., Duvio, D., Solvason, H. B., Hawkins, J., Guerra, A., Jo, B., Raj, K. S., … Williams, N. R. (2020). Stanford Accelerated Intelligent Neuromodulation Therapy for Treatment-Resistant Depression. *American Journal of Psychiatry*, *177*(8), 716–726. https://doi.org/10.1176/appi.ajp.2019.19070720

Cui, Z., Pines, A. R., Larsen, B., Sydnor, V. J., Li, H., Adebimpe, A., Alexander-Bloch, A. F., Bassett, D. S., Bertolero, M., Calkins, M. E., Davatzikos, C., Fair, D. A., Gur, R. C., Gur, R. E., Moore, T. M., Shanmugan, S., Shinohara, R. T., Vogel, J. W., Xia, C. H., … Satterthwaite, T. D. (2021). *Linking Individual Differences in Personalized Functional Network Topography to Psychopathology in Youth* (p. 2021.08.02.454763). https://doi.org/10.1101/2021.08.02.454763

Cui, Z., Pines, A. R., Larsen, B., Sydnor, V. J., Li, H., Adebimpe, A., Alexander-Bloch, A. F., Bassett, D. S., Bertolero, M., Calkins, M. E., Davatzikos, C., Fair, D. A., Gur, R. C., Gur, R. E., Moore, T. M., Shanmugan, S., Shinohara, R. T., Vogel, J. W., Xia, C. H., … Satterthwaite, T. D. (2022). Linking Individual Differences in Personalized Functional Network Topography to Psychopathology in Youth. *Biological Psychiatry*. https://doi.org/10.1016/j.biopsych.2022.05.014

De Marco, R., Ronen, I., Branzoli, F., Amato, M. L., Asllani, I., Colasanti, A., Harrison, N. A., & Cercignani, M. (2022). Diffusion-weighted MR spectroscopy (DW-MRS) is sensitive to LPS-induced changes in human glial morphometry: A preliminary study. *Brain, Behavior, and Immunity*, *99*, 256–265. https://doi.org/10.1016/j.bbi.2021.10.005

Dietze, G. (2011). Units of measurement past, present and future. International system of units. *Radiation Protection Dosimetry*, *145*(4), 426–427. https://doi.org/10.1093/rpd/ncr215

Dong, H.-M., Margulies, D. S., Zuo, X.-N., & Holmes, A. J. (2021). Shifting gradients of macroscale cortical organization mark the transition from childhood to adolescence. *Proceedings of the National Academy of Sciences*, *118*(28). https://doi.org/10.1073/pnas.2024448118

Drews, R. (1993). *The End of the Bronze Age: Changes in Warfare and the Catastrophe ca. 1200 B.C. - Third Edition* (3rd ed.). Princeton University Press. https://doi.org/10.2307/j.ctvx5wbmc

Drysdale, A. T., Grosenick, L., Downar, J., Dunlop, K., Mansouri, F., Meng, Y., Fetcho, R. N., Zebley, B., Oathes, D. J., Etkin, A., Schatzberg, A. F., Sudheimer, K., Keller, J.,

Mayberg, H. S., Gunning, F. M., Alexopoulos, G. S., Fox, M. D., Pascual-Leone, A., Voss, H. U., … Liston, C. (2017). Resting-state connectivity biomarkers define neurophysiological subtypes of depression. *Nature Medicine*, *23*(1), 28–38. https://doi.org/10.1038/nm.4246

Fick, R. H. J., Wassermann, D., Caruyer, E., & Deriche, R. (2016). MAPL: Tissue microstructure estimation using Laplacian-regularized MAP-MRI and its application to HCP data. *NeuroImage*, *134*, 365–385. https://doi.org/10.1016/j.neuroimage.2016.03.046

Giedd, J. N., & Rapoport, J. L. (2010). Structural MRI of Pediatric Brain Development: What Have We Learned and Where Are We Going? *Neuron*, *67*(5), 728–734. https://doi.org/10.1016/j.neuron.2010.08.040

Gogtay, N., Giedd, J. N., Lusk, L., Hayashi, K. M., Greenstein, D., Vaituzis, A. C., Nugent, T. F., Herman, D. H., Clasen, L. S., Toga, A. W., Rapoport, J. L., & Thompson, P. M. (2004). Dynamic mapping of human cortical development during childhood through early adulthood. *Proceedings of the National Academy of Sciences*, *101*(21), 8174–8179. https://doi.org/10.1073/pnas.0402680101

Goldstein-Piekarski, A. N., Korgaonkar, M. S., Green, E., Suppes, T., Schatzberg, A. F., Hastie, T., Nemeroff, C. B., & Williams, L. M. (2016). Human amygdala engagement moderated by early life stress exposure is a biobehavioral target for predicting recovery on antidepressants. *Proceedings of the National Academy of Sciences of the United States of America*, *113*(42), 11955–11960. https://doi.org/10.1073/pnas.1606671113

Heath, T. L. (1921). *A history of Greek mathematics*. Oxford, The Clarendon press. http://archive.org/details/cu31924008704219

Heidecker, T., Wareheim, E., & Reilly, J. C. (2010). *Check It Out! With Dr. Steve Brule*.

Hill, J., Inder, T., Neil, J., Dierker, D., Harwell, J., & Essen, D. V. (2010). Similar patterns of cortical expansion during human development and evolution. *Proceedings of the National Academy of Sciences*, *107*(29), 13135–13140. https://doi.org/10.1073/pnas.1001229107

Kleitman, N., & Engelmann, T. G. (1953). Sleep Characteristics of Infants. *Journal of Applied Physiology*, *6*(5), 269–282. https://doi.org/10.1152/jappl.1953.6.5.269

Laplace, P. S. (1902). *A philosophical essay on probabilities*. New York : J. Wiley ; London : Chapman & Hall. http://archive.org/details/philosophicaless00lapliala

Larsen, B., & Luna, B. (2018). Adolescence as a neurobiological critical period for the development of higher-order cognition. *Neuroscience & Biobehavioral Reviews*, *94*, 179–195. https://doi.org/10.1016/j.neubiorev.2018.09.005

Larson, G. J., & Bhattacharya, R. S. (2016). *The Encyclopedia of Indian Philosophies, Volume 4*. https://press.princeton.edu/books/hardcover/9780691633541/the-encyclopedia-of-indian-philosophies-volume-4

Leinekugel, X., Khazipov, R., Cannon, R., Hirase, H., Ben-Ari, Y., & Buzsáki, G. (2002). Correlated Bursts of Activity in the Neonatal Hippocampus in Vivo. *Science*, *296*(5575), 2049–2052. https://doi.org/10.1126/science.1071111

Leskovec, J., Backstrom, L., & Kleinberg, J. (2009). Meme-tracking and the dynamics of the news cycle. *Proceedings of the 15th ACM SIGKDD International Conference on Knowledge Discovery and Data Mining*, 497–506. https://doi.org/10.1145/1557019.1557077

Li, M., Santpere, G., Kawasawa, Y. I., Evgrafov, O. V., Gulden, F. O., Pochareddy, S., Sunkin, S. M., Li, Z., Shin, Y., Zhu, Y., Sousa, A. M. M., Werling, D. M., Kitchen, R. R., Kang, H. J., Pletikos, M., Choi, J., Muchnik, S., Xu, X., Wang, D., … Sestan, N. (2018). Integrative functional genomic analysis of human brain development and neuropsychiatric risks. *Science*, *362*(6420), eaat7615. https://doi.org/10.1126/science.aat7615

Macleod, N., Rawson, P. F., Forey, P. L., Banner, F. T., Boudagher-Fadel, M. K., Bown, P. R., Burnett, J. A., Chambers, P., Culver, S., Evans, S. E., Jeffery, C., Kaminski, M. A., Lord, A. R., Milner, A. C., Milner, A. R., Morris, N., Owen, E., Rosen, B. R., Smith, A. B., … Young, J. R. (1997). The Cretaceous-Tertiary biotic transition. *Journal of the Geological Society*, *154*(2), 265–292. https://doi.org/10.1144/gsjgs.154.2.0265

Marek, S., Tervo-Clemmens, B., Calabro, F. J., Montez, D. F., Kay, B. P., Hatoum, A. S., Donohue, M. R., Foran, W., Miller, R. L., Hendrickson, T. J., Malone, S. M., Kandala, S., Feczko, E., Miranda-Dominguez, O., Graham, A. M., Earl, E. A., Perrone, A. J., Cordova, M., Doyle, O., … Dosenbach, N. U. F. (2022). Reproducible brain-wide association studies require thousands of individuals. *Nature*, *603*(7902), 654–660. https://doi.org/10.1038/s41586-022-04492-9

Mazziotta, J. C., Woods, R., Iacoboni, M., Sicotte, N., Yaden, K., Tran, M., Bean, C., Kaplan, J., Toga, A. W., & Members of the International Consortium for Brain Mapping (ICBM). (2009). The myth of the normal, average human brain--the ICBM experience: (1) subject screening and eligibility. *NeuroImage*, *44*(3), 914–922. https://doi.org/10.1016/j.neuroimage.2008.07.062

Melamed, D., Nov, Y., Malik, A., Yakass, M. B., Bolotin, E., Shemer, R., Hiadzi, E. K., Skorecki, K. L., & Livnat, A. (2022). De novo mutation rates at the single-mutation resolution in a human HBB gene-region associated with adaptation and genetic disease. *Genome Research*, gr.276103.121. https://doi.org/10.1101/gr.276103.121

Melrose, S. (2015). Seasonal Affective Disorder: An Overview of Assessment and Treatment Approaches. *Depression Research and Treatment*, *2015*, 178564. https://doi.org/10.1155/2015/178564

Mitra, A., Kraft, A., Wright, P., Acland, B., Snyder, A. Z., Rosenthal, Z., Czerniewski, L., Bauer, A., Snyder, L., Culver, J., Lee, J.-M., & Raichle, M. E. (2018). Spontaneous

Infra-slow Brain Activity Has Unique Spatiotemporal Dynamics and Laminar Structure. *Neuron*, *98*(2), 297-305.e6. https://doi.org/10.1016/j.neuron.2018.03.015

Murtha, K., Larsen, B., Pines, A., Parkes, L., Moore, T. M., Adebimpe, A., Alexander-Bloch, A., Calkins, M. E., Davila, D. G., Lindquist, M. A., Mackey, A. P., Roalf, D. R., Scott, J. C., Wolf, D. H., Gur, R. C., Gur, R. E., Barzilay, R., & Satterthwaite, T. D. (2021). *Association between Neighborhood Socioeconomic Status and Executive System Activation in Youth* (p. 2021.08.12.454903). https://doi.org/10.1101/2021.08.12.454903

Nenning, K.-H., Xu, T., Schwartz, E., Arroyo, J., Woehrer, A., Franco, A. R., Vogelstein, J. T., Margulies, D. S., Liu, H., Smallwood, J., Milham, M. P., & Langs, G. (2020). Joint embedding: A scalable alignment to compare individuals in a connectivity space. *NeuroImage*, *222*, 117232. https://doi.org/10.1016/j.neuroimage.2020.117232

Palva, S., & Palva, J. M. (2018). Roles of Brain Criticality and Multiscale Oscillations in Temporal Predictions for Sensorimotor Processing. *Trends in Neurosciences*, *41*(10), 729–743. https://doi.org/10.1016/j.tins.2018.08.008

Pearce, T. (2010). From "circumstances" to "environment": Herbert Spencer and the origins of the idea of organism-environment interaction. *Studies in History and Philosophy of Biological and Biomedical Sciences*, *41*(3), 241–252. https://doi.org/10.1016/j.shpsc.2010.07.003

Pines, A., Keller, A. S., Larsen, B., Bertolero, M., Ashourvan, A., Bassett, D. S., Cieslak, M., Covitz, S., Fan, Y., Feczko, E., Houghton, A., Rueter, A. R., Tapera, T., Vogel, J., Weinstein, S. M., Shinohara, R. T., Fair, D., & Satterthwaite, T. (2022). Development of Top-Down Cortical Propagations in Youth. *BioRxiv*, 2022.06.14.496175. https://doi.org/10.1101/2022.06.14.496175

Pines, A. R., Cieslak, M., Larsen, B., Baum, G. L., Cook, P. A., Adebimpe, A., Dávila, D. G., Elliott, M. A., Jirsaraie, R., Murtha, K., Oathes, D. J., Piiwaa, K., Rosen, A. F. G., Rush, S., Shinohara, R. T., Bassett, D. S., Roalf, D. R., & Satterthwaite, T. D. (2020). Leveraging multi-shell diffusion for studies of brain development in youth and young adulthood. *Developmental Cognitive Neuroscience*, *43*, 100788. https://doi.org/10.1016/j.dcn.2020.100788

Pines, A. R., Larsen, B., Cui, Z., Sydnor, V. J., Bertolero, M. A., Adebimpe, A., Alexander-Bloch, A. F., Davatzikos, C., Fair, D. A., Gur, R. C., Gur, R. E., Li, H., Milham, M. P., Moore, T. M., Murtha, K., Parkes, L., Thompson-Schill, S. L., Shanmugan, S., Shinohara, R. T., … Satterthwaite, T. D. (2022). Dissociable multi-scale patterns of development in personalized brain networks. *Nature Communications*, *13*(1), 2647. https://doi.org/10.1038/s41467-022-30244-4

Rousseau, J.-J. (1762, October 29). *Du contrat social ou Principes du droit politique*. https://www.worldcat.org/title/du-contrat-social-ou-principes-du-droit-politique/oclc/85101219?page=citation

Rudolph, M. D., Graham, A. M., Feczko, E., Miranda-Dominguez, O., Rasmussen, J. M., Nardos, R., Entringer, S., Wadhwa, P. D., Buss, C., & Fair, D. A. (2018). Maternal IL-6 during pregnancy can be estimated from newborn brain connectivity and predicts future working memory in offspring. *Nature Neuroscience*, *21*(5), 765–772. https://doi.org/10.1038/s41593-018-0128-y

*SOAS: Standard Babylonian Epic of Gilgamesh*. (n.d.). Retrieved May 24, 2022, from https://www.soas.ac.uk/gilgamesh/standard/

Sotiras, A., Toledo, J. B., Gur, R. E., Gur, R. C., Satterthwaite, T. D., & Davatzikos, C. (2017). Patterns of coordinated cortical remodeling during adolescence and their associations with functional specialization and evolutionary expansion. *Proceedings of the National Academy of Sciences*, *114*(13), 3527–3532. https://doi.org/10.1073/pnas.1620928114

Sowell, E. R., Thompson, P. M., Holmes, C. J., Jernigan, T. L., & Toga, A. W. (1999). In vivo evidence for post-adolescent brain maturation in frontal and striatal regions. *Nature Neuroscience*, *2*(10), 859–861. https://doi.org/10.1038/13154

Stringer, C., Pachitariu, M., Steinmetz, N., Reddy, C. B., Carandini, M., & Harris, K. D. (2019). Spontaneous behaviors drive multidimensional, brainwide activity. *Science*, *364*(6437). https://doi.org/10.1126/science.aav7893

Subica, A. M., & Link, B. G. (2022). Cultural trauma as a fundamental cause of health disparities. *Social Science & Medicine*, *292*, 114574. https://doi.org/10.1016/j.socscimed.2021.114574

Taylan, F. (2022). The Rise of the "Environment": Lamarckian Environmentalism Between Life Sciences and Social Philosophy. *Biological Theory*, *17*(1), 4–19. https://doi.org/10.1007/s13752-020-00358-3

Tooley, U. A., Bassett, D. S., & Mackey, A. P. (2021). Environmental influences on the pace of brain development. *Nature Reviews Neuroscience*, 1–13. https://doi.org/10.1038/s41583-021-00457-5

Vainik, U., Paquola, C., Wang, X., Zheng, Y., Bernhardt, B., Misic, B., & Dagher, A. (2020). Heritability of cortical morphology reflects a sensory-fugal plasticity gradient. *BioRxiv*, 2020.11.03.366419. https://doi.org/10.1101/2020.11.03.366419

Vitaterna, M. H., Takahashi, J. S., & Turek, F. W. (2001). Overview of Circadian Rhythms. *Alcohol Research & Health*, *25*(2), 85–93.

Vogel, J. W., La Joie, R., Grothe, M. J., Diaz-Papkovich, A., Doyle, A., Vachon-Presseau, E., Lepage, C., Vos de Wael, R., Thomas, R. A., Iturria-Medina, Y., Bernhardt, B., Rabinovici, G. D., & Evans, A. C. (2020). A molecular gradient along the longitudinal axis of the human hippocampus informs large-scale behavioral systems. *Nature Communications*, *11*(1), 960. https://doi.org/10.1038/s41467-020-14518-3

Wegman, M. E. (2001). Infant Mortality in the 20th Century, Dramatic but Uneven Progress. *The Journal of Nutrition*, *131*(2), 401S-408S. https://doi.org/10.1093/jn/131.2.401S

Will Durant. (n.d.). *The Story Of Philosophy*. Retrieved June 26, 2022, from http://archive.org/details/in.ernet.dli.2015.264687

Yang, J., Huber, L., Yu, Y., & Bandettini, P. A. (2021). Linking cortical circuit models to human cognition with laminar fMRI. *Neuroscience & Biobehavioral Reviews*, *128*, 467–478. https://doi.org/10.1016/j.neubiorev.2021.07.005